

From surface properties towards a multiscale approach for modelling MgF₂ nanocrystals

INAUGURAL-DISSERTATION
TO OBTAIN THE ACADEMIC DEGREE
DOCTOR RERUM NATURALIUM (DR. RER. NAT.)
SUBMITTED TO THE DEPARTMENT OF
BIOLOGY, CHEMISTRY AND PHARMACY
OF FREIE UNIVERSITÄT BERLIN

by
Elisavet Kanaki
from Athens

2015

This work was prepared under supervision of
Prof. Dr. Beate Paulus (Freie Universität Berlin)
from October 2011 until November 2015

1. Gutachter: Prof. Dr. Beate Paulus
2. Gutachter: Prof. Dr. Erhard Kemnitz

Disputation am 18. Januar 2016

Summary

Nanostructured sol-gel synthesized magnesium fluoride exhibits catalytic activity significantly different than its conventional counterparts. It has been shown experimentally to act as a moderate Lewis acid due to coordinatively unsaturated cations on the surface. When partially hydroxylated, the material is shown to combine Brønsted- and Lewis-acidity. In this work, surfaces of magnesium fluoride are examined in a variety of pure and partially hydroxylated terminations in order to break down the catalytic activity of the material into individual interactions. In addition, the quantum chemical results are combined with surface thermodynamics for the prediction of the relative stability of terminations at finite conditions of temperature and pressure of hydrogen fluoride and water. The shape of magnesium fluoride crystals at these conditions is predicted using Wulff constructions. Adsorption of hydrogen fluoride and of water on the surfaces is modelled using density functional, perturbation, and Hartree-Fock theory for the periodic systems. The results show that the basicity and position of the fluorines on the surface are as important as the acidity of the cations. As a consequence, no direct connection was found between the number of missing coordination partners of cationic sites and the strength of adsorption. Instead the adsorption is governed by the synergetic effect of acid-base pairs. Theoretical results indicate that surface hydroxyls are in some occasions Brønsted-basic while in others they act as adsorption sites for water. From a methodological point of view, it was shown that complex adsorption situations cannot be described adequately by DFT. The presence of hydrogen fluoride and water, as well as temperature, have a significant effect on the relative stability of the different terminations. The agreement to perturbation theory showed that the description with DFT/B3LYP is satisfactory for the description of the crystal shapes. Unfortunately, the model can not be validated for the case of sol-gel synthesized material, due to the lack of suitable experimental data. A classical force field was parametrized based on the DFT description of magnesium fluoride. This will enable the mesoscale modelling of magnesium fluoride crystallites beyond the periodic model.

Zusammenfassung

Nanostrukturiertes, mittels Sol-Gel-Synthese hergestelltes Magnesiumfluorid weist katalytische Eigenschaften auf, die sich von denen des konventionell hergestellten Materials signifikant unterscheiden. Experimentell hat es sich aufgrund der koordinativ ungesättigten Kationen an seiner Oberfläche als moderate Lewis-Säure erwiesen. In seiner partiell hydroxylierten Form werden Brønsted- und Lewis-Säure kombiniert. In dieser Arbeit werden Magnesiumfluoridoberflächen in verschiedenen reinen und partiell hydroxylierten Terminierungen untersucht, um die katalytische Aktivität in die einzelnen Wechselwirkungen zu zerlegen. Zusätzlich werden die quantenchemischen Ergebnisse mit Oberflächenthermodynamik kombiniert, um die relative Stabilität der Terminierungen in Bedingungen endlicher Temperatur und endlichen Partialdrucks von Fluorwasserstoff und Wasser vorherzusagen. Die Form von Magnesiumfluoridkristallen unter diesen Bedingungen werden mittels Wulffkonstruktionen vorhergesagt. Die Adsorption von Fluorwasserstoff und Wasser wird mittels Dichtefunktional-, Störungs- und Hartree-Fock-Theorie in periodischen Systemen modelliert. Die Ergebnisse zeigen, dass dabei die Basizität und die Position der Fluoratome an der Oberfläche so wichtig wie die Säure der Kationen sind. Infolgedessen wurde kein direkter Zusammenhang zwischen der Anzahl fehlender Koordinationspartner der Kationen und der Stärke der Adsorption identifiziert. Stattdessen ist das Zusammenwirken der Säure-Base-Paare für die Adsorption maßgebend. Laut den theoretischen Ergebnissen sind die Hydroxyle an der Oberfläche in manchen Fällen Brønsted-basisch, während sie in anderen Fällen als Adsorptionszentren für Wasser dienen. Aus methodischer Sicht wurde gezeigt, dass komplizierte Adsorptionssituationen mit DFT nicht ausreichend beschrieben werden. Sowohl die Präsenz von Fluorwasserstoff und Wasser als auch die Temperatur haben einen signifikanten Effekt auf die relative Stabilität unterschiedlicher Terminierungen. Die Übereinstimmung zur Störungstheorie zeigt, dass DFT/B3LYP die Form der Kristalle befriedigend beschreibt. Leider kann das Modell für mittels Sol-Gel synthetisiertes Material mangels experimenteller Daten nicht validiert werden. In Anlehnung an die Beschreibung mittels DFT wurde ein klassisches Kraftfeld für Magnesiumfluorid parametrisiert. So wird eine mesoskalige Modellierung von Magnesiumfluoridkristallen jenseits des periodischen Modells ermöglicht.

Contents

List of figures	9
List of tables	11
List of abbreviations	13
1 Introduction	15
2 Theoretical background and methodology	23
2.1 Quantum chemical methods	23
2.1.1 Introduction	23
2.1.2 The Hartree-Fock approximation	24
2.1.3 Perturbation theory	26
2.1.4 Density functional theory	29
2.1.5 Electronic structure of solids	32
2.2 Long-range effects	34
2.2.1 Dipole-dipole interaction	34
2.2.2 Dispersion correction for DFT	35
2.2.3 Electrostatic contributions in periodic systems	37
2.3 Surface thermodynamics	38
3 Computational methods	43
3.1 General remarks	43
3.2 Model of the surfaces	43
3.3 Surface thermodynamics	44
3.3.1 Calculation of the chemical potential	44
3.4 Parametrization of classical force fields	45
4 Results	49
4.1 The contribution of electron correlation to the stability of low-index surfaces	50
4.2 Truncation and stability of vicinal surfaces	55
4.3 Surface (103)	58
4.3.1 Terminations and adsorption	58
4.3.2 Surface thermodynamics	61
4.4 Surface thermodynamics based on MP2 energies	62
4.4.1 Phase diagrams and crystal morphology	62

4.4.2	MP2 versus DFT for surface thermodynamics	67
4.5	A force field for MgF_2	67
4.5.1	Embedded clusters as a model for MgF_2 bulk	67
4.5.2	Fitted force fields	70
4.5.3	Validation of the force fields	73
5	Publications	77
5.1	Paper P1	79
5.2	Paper P2	89
6	Conclusions	103
	Bibliography	107
	Acknowledgement	115

List of figures

1.1	Possible products of the sol-gel synthesis for nanostructured MgF_2 . . .	16
1.2	Coordination in the magnesium fluoride bulk	18
2.1	Treatment of interfaces in thermodynamics.	40
2.2	The Wulff construction	42
3.1	Construction of the slab	44
3.2	The minimum image convention	46
3.3	Strategy for the parametrization of classical pair potentials	48
4.1	The effect of truncation on the surface energy of unrelaxed slabs	50
4.2	Relaxed surfaces of rutile MgF_2	52
4.3	HF on partially hydroxylated low-index surfaces	54
4.4	Periodicity and symmetry in vicinal slabs	56
4.5	Convergence of the surface energy for vicinal cuts	57
4.6	Relaxed structure of surface (103)	58
4.7	Adsorption structures of HF and H_2O on terminations of (103)	59
4.8	Phase diagrams for surface (103)	61
4.9	Phase diagrams at 300 K, based on MP2 energies	63
4.10	Phase diagrams at 450 K, based on MP2 energies	64
4.11	Phase diagrams at 600 K, based on MP2 energies	65
4.12	Exposed surfaces of MgF_2 crystals from MP2 calculations	66
4.13	Translational asymmetric unit of MgF_2	68
4.14	Bulk energy from embedding	69
4.15	EOS for MgF_2	71
4.16	Pair potentials for MgF_2	73
4.17	Clusters for validation of the force field	74
4.18	Total energy of the clusters from DFT and fitted force fields	75

List of tables

3.1	Shomate equation factors for H ₂ O and HF	45
4.1	Surface energy for low-index terminations	51
4.2	Energy of hydroxylation	53
4.3	Energy of vicinal surfaces	58
4.4	Energy of hydroxylation for surface (103)	58
4.5	Adsorption energies for H ₂ O and HF on (103)	60
4.6	Exposed surfaces of MgF ₂ crystals from MP2 calculations	66
4.7	Parameters of the pair potentials in Catti's force field	68
4.8	Parameters of selected fitted force fields	70
4.9	Fitted EOS	72
4.10	Energy of clusters obtained from DFT and MM calculations	74

List of abbreviations

B3LYP Becke, three-parameter, Lee-Yang-Parr (hybrid functional)

B3PW Becke, three-parameter, Perdew-Wang (hybrid functional)

BSSE Basis set superposition error

DFT Density functional theory

EOS Equation of states

GGA General gradient approximation

LCAO Linear combination of atomic orbitals

LDA Local density approximation

LMP2 Local MP2

MD Molecular dynamics

MM Molecular mechanics

MP2 second-order Møller-Plesset perturbation theory

PBE Perdew-Burke-Ernzerhof (GGA functional)

PW91 Perdew-Wang 91 (GGA functional)

SSE Sum of squared errors

1 Introduction

An increasing awareness concerning the environmental impact of human activity and industrialization has emerged in the past couple of decades [1]. This is reflected, for example, in the introduction of the term *green chemistry* in 1998 [2] and its wide use ever since. In twelve principles, the term comprises the aims to be pursued for a sustainable chemical industry; minimization of waste production and of the use of auxiliary substances, reduction of toxicity of reagents and products, preference for catalytic routes are only some of the aspects it addresses.

Catalysis is called “a foundational pillar of green chemistry” [3]. In particular high surface heterogeneous catalysts offer the advantage of relatively easy separation and re-use compared to the alternatives [4], which makes their use attractive. Nanoscopic structures offer, in addition to the advantage of high surface area – or partly as a consequence thereof, higher catalytic activities compared to the corresponding conventional material. An excellent example of such behaviour is MgF_2 . Until recently, it was regarded as rather unreactive, only suitable as catalytic support [5]. This changed with the development of the sol-gel synthetic route for metal fluorides in the early 2000s [6]. Originally used for the production of nanostructured AlF_3 , the sol-gel synthesis has evolved into a flexible process for the synthesis of a wide range of fluorides [7], including MgF_2 .

Synthesis and catalytic applications of nanostructured magnesium fluoride

The sol-gel synthesis offers a possibility to produce MgF_2 -based material with a variety of surface modifications (fig. 1.1). The procedure essentially consists of the formation of magnesium alkoxide from metallic magnesium and a solvent, and its consequent reaction with hydrogen fluoride to form a sol or gel. The end-product is obtained after a suitable thermal treatment with post-fluorination. Small variations of the synthetic process give rise to modifications of the nanomaterial's surface; reported functionalizations include for example the introduction of sulfonic [8], or oxide groups on the surface [9], doping with noble metals [10], coexistence of MgF_2 with other phases [11], and partial hydroxylation of the surface [12–14]. Although nanoscopic MgF_2 can be produced using a variety of methods, sol-gel synthesis is the only possibility, until now, for the production of partially hydroxylated material (see [15] and references therein). Hydroxylation is achieved by using aqueous HF, thus provoking a competition between fluorolysis and hydrolysis. Fluorolysis is significantly favoured against hydrolysis, so only a small amount of hydroxyls are introduced in the nanomaterial. Still, different concentrations of surface hydroxyls can be achieved by variation of the ratio of H_2O to HF [16]. The nanomaterial's surface

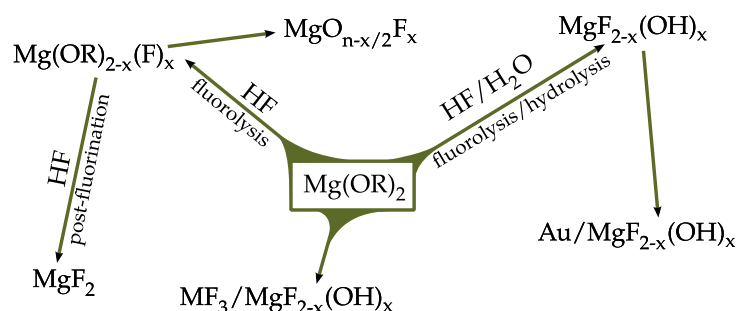


Figure 1.1: Some of the possible products of the sol-gel synthesis for nanostructured MgF_2 .

modifications determine its catalytic activity, making it useful in a variety of applications.

Compared to other metal fluorides, pure MgF_2 shows a weak to moderate Lewis-acidity, which is advantageous for certain applications. An example is the fluorination of 2-chloropyridine to 2-fluoropyridine, an intermediate in the production of pesticides and other biologically active compounds: According to the proposed mechanism, HF forms chains coordinated to surface fluorines. The free F-end of the chain attacks the 2-chloropyridine, which is adsorbed on a cationic site. It was shown that catalysts with stronger Lewis-acidity are not as efficient as MgF_2 [17]. In other cases, variation of the Lewis-acidity leads to manipulation of the outcome of a reaction, as in the case of dehydrohalogenation of haloalkanes. It was demonstrated in the example of 3-chloro-1,1,1,3-tetrafluorobutane that AlF_3 and MgF_2 selectively catalyse the elimination of HF, whereas the much weaker acid BaF_2 the elimination of HCl [18].

Partially hydroxylated MgF_2 combines Lewis- and Brønsted-acidic properties due to the cationic sites and acidic hydroxyls on the surface, respectively. It is a particularly suited catalyst for synthetic routes involving Friedel-Crafts reactions, yet its catalytic properties depend to a certain extent on the concentration of the hydroxyls. This is illustrated in the following examples: According to the proposed mechanism for the synthesis of (all-*rac*)- α -tocopherol of the vitamin E family, the first step takes place on the Brønsted-acidic hydroxyl, while the second step on the Lewis-acidic site, thus allowing a one-pot synthesis [12]. At a certain degree of hydroxylation, $\text{MgF}_{2-x}\text{OH}_x$ exhibits high degree of conversion and selectivity for this synthesis. At higher degrees of hydroxylation the conversion increases, but at the same time some of the selectivity is lost. By contrast in the synthesis of vitamin K, catalysts with a high density of Brønsted-acidic sites are more efficient [19]. Other reactions catalysed by partially hydroxylated high-surface magnesium fluoride include the dehydration of D-xylose to furfural [8], benzylation reactions [20] and the conversion of cellulose to glucose [19]. The observed acidic hydroxyls stand in contrast to those of conventional hydroxylated MgF_2 , which exhibit basic properties [21].

Other functionalities make the nanomaterial suitable for more applications: Nano-

material with oxide functionalities has been shown to perform well in the catalysis of Michael additions [9]. Nanostructured MgF_2 doped with noble metals is suitable for hydrogenation reactions. For example, gold-doped magnesium hydroxide fluoride was successfully employed for an one-pot synthesis of menthol [10]. The first step of the synthesis, the cyclization of citronellal to isopulegol is catalysed by the acidic sites, while the second step, the hydrogenation, occurs on the gold sites. Nanoscopic palladium-doped magnesium fluoride is active in the hydrogenation of styrene [7]. The outlined diversity in catalytic applications of nanoscopic MgF_2 was the inspiration for this work. The aim is to develop a predictive model for the sol-gel synthesis of MgF_2 and the properties of the synthesized material, with focus on partially hydroxylated modifications. In this context, two principle questions arise: Which properties of the surface are decisive for the catalytic activity and which synthetic conditions affect these properties.

From nanostructured MgF_2 to a quantum chemical model

The structural characteristics of sol-gel synthesized MgF_2 -based nanomaterial have been extensively investigated in a number of studies targeting both its bulk and its surface properties. Data from ^{19}F -NMR [22, 23], XRD [12] and TEM [24] show evidence of coexisting crystalline and amorphous phases in the nanomaterial's bulk. The crystalline phases have a size of 3–8 nm and space group (136), which is a rutile-type structure.

Space group (136) defines a tetragonal lattice with two MgF_2 formula units in the conventional unit cell (fig. 1.2(b)). The bulk consists of octahedra which share their edges and tips in an alternating arrangement, as shown in fig. 1.2(a). Magnesium cations and fluorine anions are arranged in the centre and corners of the octahedra respectively. So, each cation is surrounded by six anions in an octahedral coordination, while each anion is surrounded by three cations. According to results from X-ray powder diffraction, the lattice constants of rutile-type MgF_2 are $a = 4.625 \text{ \AA}$ and $c = 3.052 \text{ \AA}$, and $x(\text{F}) = 0.3024$ [25]. Periodic density functional theory with B3LYP [26, 27] shows a deviation of 3% in the volume of the unit cell, with $a = 4.667 \text{ \AA}$ and $c = 3.083 \text{ \AA}$ [28].

According to the above, a cubic MgF_2 crystal with edge of 5 nm consists of about 10^4 atoms. Based on a rough estimation, one facet of such a crystallite consists of approximately 100 unit cells or 350 atoms. So having a mean size of 5 nm, the crystalline phases in the nanomaterial are in the range of crystallites rather than clusters, and are better modelled as periodic systems.

Two possibilities for the quantum chemical description of solids are embedded cluster and periodic models. In the embedded clusters scheme, a small number of atoms around the site of interest is treated in a high level of theory. Around it, one or more hosting systems are set up, which represent the surrounding bulk and are treated in lower levels of theory. Downside of this treatment is the large amount of hand-work needed for the setup. On the other hand, the periodic treatment of solids, the principles of which are discussed in detail in the next chapter, has been largely au-

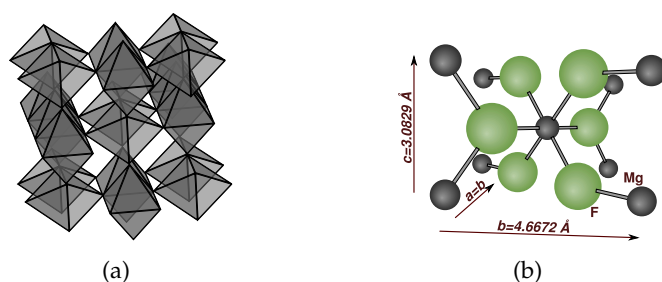


Figure 1.2: (a) Coordination in the magnesium fluoride bulk and (b) unit cell. Cations are arranged in the centre of the octahedra, anions on the edges. The unit cell includes two MgF_2 units.

tomatized in the last couple of decades, as a number of software for this purpose have been published. This constitutes an important advantage, as the present study requires the investigation of a large number of structures. Therefore, the periodic treatment was chosen for the quantum chemical modelling of the surfaces.

Adsorption as an indicator of catalytic properties

A simplified general model for heterogeneous catalysis is that of a three-step process. In the first step, one or more reactants are adsorbed on the catalyst's surface. In the second step, the reaction takes place on the surface of the catalyst, and in the third step, the product is desorbed. It is thus of importance for the catalytic activity, that the interaction between reactant and surface is adequate for the activation of the former, but at the same time not as strong as to prevent the desorption of the molecule in the third step (poisoning) [29].

Theoretical studies on heterogeneous catalysis usually focus on the snapshot between the first and second step of the process: the structure of adsorbed molecules on surfaces. The evaluation of the adsorption structure and energy can give valuable information about the type of activation that occurs, as well as the strength of the interaction between surface and molecule. However, catalytically relevant adsorption systems usually involve large molecules, for which a complex scheme of multiple interactions might compose the mechanism of activation. It is therefore helpful to study the adsorption of different small molecules on the surfaces of interest, in order to break down the complex schemes into individual interactions. This way, an insight in the mechanisms behind the catalytic activity of surfaces is gained.

The adsorption of suitable probe molecules is employed in experiment as well as in theory for the characterization of surface properties. A widely used method is the measurement of the vibrational frequency shift of probe molecules and of surface functionalities in adsorption systems compared to the free components. For example, Lewis-acidic sites are evaluated from the vibrational frequency shift of CO molecules when adsorbed on a surface [30]. For MgF_2 surfaces, it has been employed both in experimental [12] and theoretical [28] characterization of the cationic sur-

face sites revealing their Lewis-acidic character. It is however noteworthy that the calculated frequency shifts of CO do not confirm the assumption of direct analogy between Lewis-acidity and coordination number of the cations. In the presence of surface hydroxyls, CO has been employed for the experimental identification of their Brønsted-acidic properties [16]. The acid-base pairs on MgF_2 surfaces have been investigated via the vibrational frequency shifts of adsorbed CHCl_3 [31].

In this work, HF and H_2O have been chosen as probe molecules. Investigating their interaction with (partially hydroxylated) MgF_2 surfaces serves two purposes: First, they influence the formation of the nanomaterial, as both of them are reactants in the synthetic procedure. Secondly, they are involved in numerous reactions that could be catalysed by the nanomaterial, so modelling the adsorption can give an insight in the activation mechanisms occurring on MgF_2 surfaces.

Based on the strength of the interaction and its effect on the electronic structure of the adsorbates, adsorption is generally divided into chemisorption and physisorption. The former involves a change in the electronic structure of the molecule, charge-transfer and even dissociation or formation of new molecules; the latter includes correlated charge fluctuations like mutually induced dipole moments in surface and adsorbate [32]. However, the two are not distinct, but rather two limiting cases in a continuous spectrum of interaction strengths. Translated in adsorption energies, -0.5eV^1 per adsorbate is generally regarded as the limit between physisorption and chemisorption [33].

The theoretical investigation of weak interactions, as in the case of physisorption, requires consideration of electron correlation. Sophisticated wave function-based methods, e.g. configuration interaction or coupled cluster, are feasible for small systems, but their exponential scaling with the number of electrons is prohibitive for their application to large or periodic systems. A possibility to circumvent this problem is offered by approaches based on clusters, e.g. the method of increments [34–36] where the interactions are fragmented and expanded in series of different terms [37]. Unfortunately, these methods are time-consuming and require a great amount of handwork, so they cannot be used for production. The only automatized electron correlation method for periodic systems is second-order Møller-Plesset perturbation theory [38]. Based on the “local ansatz” it is implemented in the CRYSCOR package [39, 40], and a canonical implementation is available in VASP [41–44]. The MP2 description has long been regarded as sufficient for the treatment of adsorption [45]. This assumption was recently confirmed for MgF_2 [46].

Density functional theory is routinely employed for the calculation of large and extended systems. It partly accounts for electron correlation, but not always adequately. A number of correction schemes for DFT have been proposed to account for this insufficiency [47–54]. Among them, the dispersion correction schemes proposed by Grimme and coworkers [53, 54] are widely used and have been implemented in quantum chemical codes not only for molecules, but also for solids (D3 gradients are im-

¹Here and in the following, the negative sign in the adsorption energy indicates an attractive interaction.

plemented in VASP and D2 in CRYSTALOG [55, 56] and later). The Grimme corrections combine sophisticated calculations and models on one hand, and on the other hand a large number of approximations, which will be discussed in detail in the next chapter. As their description of systems involving solids and adsorption interactions has certain shortcomings, there have been efforts to improve the Grimme schemes: Civalleri *et al.* [57] have proposed a revision of the dispersion coefficients to reproduce calculations of cohesive energies and structures of molecular crystals. Ehrlich *et al.* [58] presented an adaptation of the Grimme scheme specifically concentrated on adsorption on ionic surfaces. The latter appears to perform better compared to the previous dispersion correction schemes, showing that there is the possibility to improve the performance of dispersion correction schemes.

Prediction of the morphology of the crystal surface

The advances in surface science and in heterogeneous catalysis in the mid-nineties lead to a revival in the interest for surface thermodynamics², although the scheme is based on principles of the nineteenth century physics. Initially, concepts of surface thermodynamics were employed to interpret and link experimental results from ultra-high vacuum to technically relevant conditions [59, 60]. Later, with the establishment of quantum chemical codes for periodic systems, surface thermodynamics were employed to link results from *ab initio* calculations to experimental conditions, predicting the stability of different surfaces with respect to ambient conditions. The scheme was developed and extensively tested on ruthenium/oxygen and ruthenium oxid/oxygen systems showing agreement to experimental data [61, 62]. Since then, *ab initio* surface thermodynamics have been employed to address a variety of questions concerning the stability and reactivity of surfaces (see for example references [63–70]).

The evidence of crystalline structures in nanostructured MgF_2 already in solution during formation of the sol or gel indicate that the nanostructured MgF_2 -based material could be regarded as an agglomeration of crystallites. Within this model, the surface and consequently the reactivity of the nanomaterial are largely determined by the exposed surfaces of the crystallites. Based on the fact that the sol-gel synthesis includes a thermal treatment as a last step of the process, it is sensible to assume that thermodynamics play an important role in the formation of the surfaces. On these grounds, surface thermodynamics are employed in the present work for modelling the effect of temperature and gas phase composition on the relative stability of terminations and adsorption structures, and how they consequently affect the morphology of MgF_2 crystals.

²Source: Citation reports of Web of Science™ of publications with keywords *heterogeneous catalysis* and *surface thermodynamics*.

Multiscale modelling

The combination of surface thermodynamics and periodic quantum chemical calculations offer an idealized view of the shape of the crystals. However, mesoscale effects that deviate from this view, as irregularities in the crystal shape, e.g. lattice distortion and defect formation, or agglomeration processes, are highly relevant for nanoscopic materials. In order to investigate such effects, at least partly abandoning the quantum chemical description is inevitable, due to its high computational cost: The hypothetical cubic crystal mentioned earlier consists of roughly 10^4 atoms; even after approximations, e.g. assuming perfectly symmetric crystallites with frozen core, some hundreds of atoms per crystallite need to be taken into account.

Classical force fields are routinely employed for the modelling of very large systems, with main focus on biomolecules. An enormous variety of force fields has been developed for such applications (see for example [71, 72]), spanning through a wide spectrum of functional forms, parametrized based on *ab initio* or experimental data. Recently there has been an increasing interest also for solid state modelling with classical force fields [73–77]. A classical force field for MgF_2 was published by Catti *et al.* [78] in the nineties, and was employed for simulations of MgF_2 clusters up to a size of some tenths of atoms [79, 80]. However, a study of MgF_2 in the mesoscale has not yet been done.

A challenging part of multiscale modelling is the achievement of a seamless transition between different scales. So in the last section of this work, the foundation for future investigation of nanostructured MgF_2 in the mesoscale is laid by parametrizing a force field based on the quantum chemical data.

2 Theoretical background and methodology

2.1 Quantum chemical methods

2.1.1 Introduction

Less than thirty years after the postulation of Planck’s constant [81], following a long journey of scientific – and indeed philosophical – exchange among the pioneers of the field, E. Schrödinger published a series of six papers titled “Quantisierung als Eigenwertproblem” [82], in which he postulated a wavefunction for the hydrogen atom and explored its range of applications. A few months earlier, in their famous “three-man-paper”, Born, Heisenberg, and Jordan [83] had presented an application of matrix mechanics on quantum physics. The evolution thereafter was rapid. “From about 1927 onwards, the quantum theory [...] was essentially complete” (Longair [84]). The Schrödinger equation is the core of every non-relativistic quantum chemical problem. In its general form, it is written as:

$$i \frac{\partial}{\partial t} \Psi(t, x) = \mathcal{H} \Psi(t, x). \quad (2.1)$$

The wavefunction $\Psi(t, x)$, in which t stands for time and x for all space coordinates of the quantum mechanical particles, contains all information about the system, and the Hamiltonian \mathcal{H} describes the evolution of the system and its energy states. Unfortunately, as the size of the system increases, Ψ becomes multi-dimensional and the Schrödinger equation becomes a highly complex problem, the solution of which is impossible without the introduction of approximations: First of all, quantum chemistry treats stationary states instead of following the time evolution of the system: The time dependence of the wavefunction is separated from the spatial part, and only the latter is treated. In addition, relativistic effects can be usually neglected (for light atoms). Under these two approximations, the *non-relativistic, time-independent* Hamiltonian for a system consisting of N electrons, and M nuclei of mass m and charge Z takes in atomic units the form:

$$\mathcal{H} = - \sum_{i=1}^N \frac{1}{2} \nabla_i^2 - \sum_{a=1}^M \frac{1}{2m_a} \nabla_a^2 - \sum_{i=1}^N \sum_{a=1}^M \frac{Z_a}{r_{ia}} + \sum_{i=1}^N \sum_{j>i}^N \frac{1}{r_{ij}} + \sum_{a=1}^M \sum_{b>a}^M \frac{Z_a Z_b}{r_{ab}}. \quad (2.2)$$

The first two terms describe the kinetic energy of electrons and of nuclei, followed by terms for the electrostatic interaction between nuclei and electrons (with r_{ia} the

distance between electron i and nucleus a) as well as among electrons, and among nuclei (with r_{ij} the distance between electrons i and j and r_{ab} between nuclei a and b).

The problem was further simplified by Born and Oppenheimer [85]. They suggested in 1927 that, because the nuclei's motion happens in a much slower time-scale than the motion of electrons, the latter can be regarded as moving in the field of static nuclei. As a result of the consequent separation of variables, the problem is reduced to solving the electronic Schrödinger equation:

$$\mathcal{H}^{\text{el}}|\Psi\rangle = \mathcal{E}^{\text{el}}|\Psi\rangle, \quad (2.3)$$

with \mathcal{H}^{el} the electronic Hamiltonian:

$$\mathcal{H}^{\text{el}} = -\sum_{i=1}^N \frac{1}{2} \nabla_i^2 - \sum_{i=1}^N \sum_{a=1}^M \frac{Z_a}{r_{ia}} + \sum_{i=1}^N \sum_{j>i}^N \frac{1}{r_{ij}}, \quad (2.4)$$

getting the electronic energy \mathcal{E}^{el} . Then, the potential energy of the system within the Born-Oppenheimer approximation can be readily calculated as:

$$\mathcal{E} = \mathcal{E}^{\text{el}} + \sum_{a=1}^M \sum_{b>a}^M \frac{Z_a Z_b}{r_{ab}}. \quad (2.5)$$

In the present work, systems are only treated within the Born-Oppenheimer approximation and focus is placed on methods for the calculation of the electronic energy. Thus for simplicity, \mathcal{H} and \mathcal{E} will be written in the following instead of \mathcal{H}^{el} and \mathcal{E}^{el} .

2.1.2 The Hartree-Fock approximation

In the Hartree approximation [86], the electronic wavefunction Ψ of an N -electron system is approximated by a set of N orthogonal spin orbitals χ :

$$\Psi(x_1, x_2, \dots, x_N) = \chi(x_1)\chi(x_2)\dots\chi(x_N). \quad (2.6)$$

Slater explicitly included the Pauli exclusion principle in the above formalism by writing Ψ as an antisymmetric wavefunction [87], the Slater determinant. For a system of N electrons in spin orbitals χ , the Slater determinant is written as:

$$\Psi(x_1, x_2, \dots, x_N) = \frac{1}{\sqrt{N!}} \begin{vmatrix} \chi_i(x_1) & \chi_j(x_1) & \cdots & \chi_k(x_1) \\ \chi_i(x_2) & \chi_j(x_2) & \cdots & \chi_k(x_2) \\ \vdots & \vdots & \ddots & \vdots \\ \chi_i(x_N) & \chi_j(x_N) & \cdots & \chi_k(x_N) \end{vmatrix}, \quad (2.7)$$

with normalization factor $\frac{1}{\sqrt{N!}}$. Hartree later included exchange in his theory reformulating it into the Hartree-Fock equations [88, 89]. The problem then consists in finding, following the variational principle, the set of χ_i which gives the lowest energy. This is the best approximation to the electronic energy \mathcal{E} , and the Slater determinant Ψ_0 that gives E_0 is the best approximation for the wavefunction:

$$E_0 = \langle \Psi_0 | \mathcal{H} | \Psi_0 \rangle. \quad (2.8)$$

Each electron is assumed to interact with an effective potential of all other electrons in the system (self-consistent field approximation) [90], so instead of solving the N -electron Schrödinger equation, one needs to solve N one-electron equations, the Hartree-Fock equations (eq. 2.9). The Fock operator f is an effective one-electron operator, which acts on the spin orbitals. So, the eigenvalue problem that needs to be solved is:

$$f|\chi_i\rangle = \varepsilon_i|\chi_i\rangle, \quad (2.9)$$

where the Fock operator takes the form:

$$f = h(1) + v^{\text{hf}}(1). \quad (2.10)$$

The $h(1)$ part of the one-electron Hamiltonian includes the kinetic energy of electron (1) and its interaction with the nuclei:

$$h(1) = -\frac{1}{2}\nabla^2 - \sum_a \frac{Z_a}{r_{1a}} \quad (2.11)$$

The interaction of electron (1) in spin orbital χ_i with the other electrons in the system is expressed by the effective Hartree-Fock potential $v^{\text{hf}}(1)$:

$$v^{\text{hf}}(1) = \sum_{j \neq i} (\mathcal{J}_j(1) - \mathcal{K}_j(1)). \quad (2.12)$$

It consists of the Coulomb operator $\mathcal{J}_j(1)$ which expresses the classical Coulomb interaction between two electrons (1) and (2) in orbitals i and j :

$$\mathcal{J}_j(1)\chi_i(1) = \left[\int d\mathbf{x}_2 \chi_j^*(2) \frac{1}{r_{12}} \chi_j(2) \right] \chi_i(1), \quad (2.13)$$

and the exchange operator $\mathcal{K}_j(1)$ – without classical equivalent:

$$\mathcal{K}_j(1)\chi_i(1) = \left[\int d\mathbf{x}_2 \chi_j^*(2) \frac{1}{r_{12}} \chi_i(2) \right] \chi_j(1). \quad (2.14)$$

The exchange integral vanishes when electrons (1) and (2) have antiparallel spin due to the orthogonality of spin orbitals. Self-interaction is intrinsically dealt with in Hartree-Fock theory, since exchange and Coulomb integrals cancel out when $\chi_i = \chi_j$. The orbital energy ε_i of eq. 2.9 is calculated as the sum of the integrals:

$$\varepsilon_i = \langle \chi_i | f | \chi_i \rangle = \langle \chi_i | h(i) | \chi_i \rangle + \sum_j \langle \chi_i | \mathcal{J}_j | \chi_i \rangle - \sum_j \langle \chi_i | \mathcal{K}_j | \chi_i \rangle, \quad (2.15)$$

and the total electronic energy E_0 is derived from the orbital energies according to:

$$E_0 = \sum_i \varepsilon_i - \frac{1}{2} \left(\sum_{ij} \langle \chi_i | \mathcal{J}_j | \chi_i \rangle - \sum_{ij} \langle \chi_i | \mathcal{K}_j | \chi_i \rangle \right). \quad (2.16)$$

In restricted Hartree-Fock, the set of spin orbitals consists of pairs with the same spatial part and antiparallel spin. As a consequence, the spin components can be

integrated out in closed-shell systems and the orbital energy only depends on the spatial component ψ .

Roothaan and Hall [91, 92] proposed to express the unknown molecular orbitals ψ_i as a linear combination of known basis functions ϕ_μ :

$$\psi_i = \sum_{\mu=1}^K C_{\mu i} \phi_\mu. \quad (2.17)$$

This way, the variational problem consists in finding the coefficients $C_{\mu i}$, for which the orbitals minimize the energy. The matrix representation of the Roothaan equations is:

$$\mathbf{FC} = \mathbf{SC}\boldsymbol{\varepsilon}. \quad (2.18)$$

The orbital energies ε_i are stored in the diagonal matrix $\boldsymbol{\varepsilon}$. The coefficients $C_{\mu i}$ of the linear expansion in eq. 2.17 are stored in the square matrix \mathbf{C} . As the basis functions ϕ are not necessarily orthogonal, a hermitian overlap matrix \mathbf{S} emerges. Its elements are defined as the overlap of the basis functions:

$$S_{\mu\nu} = \int \phi_\mu^*(1) \phi_\nu(1) d\mathbf{r}_1, \quad (2.19)$$

and take values between 0 and 1. \mathbf{F} is the Fock matrix, a hermitian matrix with elements:

$$F_{\mu\nu} = \int \phi_\mu^*(1) f \phi_\nu(1) d\mathbf{r}_1, \quad (2.20)$$

with f the Fock operator of eq. 2.10. Since the elements of the Fock matrix $F_{\mu\nu}$ depend on the coefficients $C_{\nu i}$, the Roothaan equations can only be solved iteratively.

2.1.3 Perturbation theory

Rayleigh-Schrödinger perturbation theory

One of the possibilities to improve the Hartree-Fock solution is perturbation theory. It presupposes that a problem, the exact solution of which is unknown, can be reduced to a simple part that can be solved exactly, and a *perturbation*. The contribution of the latter to the energy must be expected to be small compared to the unperturbed part. The time-independent perturbation theory is known as Rayleigh-Schrödinger perturbation theory [93]. The derivation presented in this section for the energy perturbation follows the notation by Szabo and Ostlund [94].

To solve the eigenvalue problem of eq. 2.3 using perturbation theory, the exact Hamiltonian \mathcal{H} is rewritten as a combination of the unperturbed Hamiltonian \mathcal{H}^0 and a perturbation \mathcal{H}' :

$$\mathcal{H}|\Phi_i\rangle = (\mathcal{H}^0 + \lambda\mathcal{H}')|\Phi_i\rangle = \mathcal{E}_i|\Phi_i\rangle. \quad (2.21)$$

The factor λ allows for a continuous transition from the perturbed to the unperturbed system taking values between one and zero. The eigenfunctions Φ_i and energies \mathcal{E}_i can be expanded in power series in λ :

$$\Phi_i = \Phi_i^{(0)} + \lambda\Phi_i^{(1)} + \lambda^2\Phi_i^{(2)} + \dots \quad (2.22)$$

$$\mathcal{E}_i = E_i^{(0)} + \lambda E_i^{(1)} + \lambda^2 E_i^{(2)} + \dots \quad (2.23)$$

$\Phi_i^{(0)}$ is required to be normalized, while the k -th order correction to the wavefunction $\Phi_i^{(k)}$ is required to fulfil the constrain of intermediate normalization:

$$\langle \Phi_i^{(0)} | \Phi_i \rangle. \quad (2.24)$$

Substitution of eq. 2.22 into 2.24, results in:

$$\langle \Phi_i^{(0)} | \Phi_i^{(0)} \rangle + \lambda \langle \Phi_i^{(0)} | \Phi_i^{(1)} \rangle + \lambda^2 \langle \Phi_i^{(0)} | \Phi_i^{(2)} \rangle + \dots = 1, \quad (2.25)$$

and as eq. 2.25 is required to hold for every λ between zero and one, it follows that:

$$\langle \Phi_i^{(0)} | \Phi_i^{(1)} \rangle = 0, \langle \Phi_i^{(0)} | \Phi_i^{(2)} \rangle = 0, \dots \quad (2.26)$$

Substituting equations 2.22 and 2.23 into 2.21 gives:

$$\begin{aligned} & (\mathcal{H}^0 + \lambda \mathcal{H}') \left(|\Phi_i^{(0)}\rangle + \lambda |\Phi_i^{(1)}\rangle + \lambda^2 |\Phi_i^{(2)}\rangle + \dots \right) = \\ & \left(E_i^{(0)} + \lambda E_i^{(1)} + \lambda^2 E_i^{(2)} + \dots \right) \left(|\Phi_i^{(0)}\rangle + \lambda |\Phi_i^{(1)}\rangle + \lambda^2 |\Phi_i^{(2)}\rangle + \dots \right). \end{aligned} \quad (2.27)$$

This holds for every λ , so eq. 2.27 can be split into equations according to the powers of λ . For instance, grouping the λ^1 -terms and multiplying by $\langle \Phi_n^{(0)} |$ results in:

$$\langle \Phi_n^{(0)} | \mathcal{H}^0 | \Phi_i^{(1)} \rangle - E_i^{(0)} \langle \Phi_n^{(0)} | \Phi_i^{(1)} \rangle = E_i^{(1)} \langle \Phi_n^{(0)} | \Phi_i^{(0)} \rangle - \langle \Phi_n^{(0)} | \mathcal{H}' | \Phi_i^{(0)} \rangle. \quad (2.28)$$

Taking into account the orthonormality of the unperturbed wavefunctions and the fact that \mathcal{H}^0 is hermitian, eq. 2.28 gives for $i = n$ following expressions for the first-order correction of the energy:

$$E_i^{(1)} = \langle \Phi_i^{(0)} | \mathcal{H}' | \Phi_i^{(0)} \rangle. \quad (2.29)$$

Following the same steps with the λ^2 -terms of eq. 2.27, the expression for the second-order correction is:

$$E_i^{(2)} = \langle \Phi_i^{(0)} | \mathcal{H}' | \Phi_i^{(1)} \rangle. \quad (2.30)$$

So for the calculation of $E_i^{(2)}$, the first-order corrected wavefunction $\Phi_i^{(1)}$ is required. $\Phi_i^{(1)}$ is expanded in the basis of eigenfunctions of \mathcal{H}^0 :

$$|\Phi_i^{(1)}\rangle = \sum_n c_n |\Phi_n^{(0)}\rangle \quad (2.31)$$

with coefficients $c_n = \langle \Phi_n^{(0)} | \Phi_i^{(1)} \rangle$ and $c_i = 0$ as a consequence of the intermediate normalization. As the unperturbed wavefunctions are mutually orthogonal, eq. 2.28 gives for $n \neq i$:

$$\langle \Phi_n^{(0)} | \mathcal{H}' | \Phi_i^{(0)} \rangle = \left(E_i^{(0)} - E_n^{(0)} \right) \langle \Phi_n^{(0)} | \Phi_i^{(1)} \rangle, \quad (2.32)$$

so the first-order corrected wavefunction is:

$$|\Phi_i^{(1)}\rangle = \sum_{n:n \neq i} \frac{\langle \Phi_n^{(0)} | \mathcal{H}' | \Phi_i^{(0)} \rangle}{E_i^{(0)} - E_n^{(0)}} |\Phi_n^{(0)}\rangle. \quad (2.33)$$

For the second-order correction of the energy, eq. 2.33 is substituted into 2.30:

$$E_i^{(2)} = \sum_{i \neq n} \frac{\left| \langle \Phi_n^{(0)} | \mathcal{H}' | \Phi_i^{(0)} \rangle \right|^2}{E_i^{(0)} - E_n^{(0)}}. \quad (2.34)$$

Corrections of higher order for the energy and wavefunction are obtained in an analogous manner.

Correlation energy

Correlated systems can be described by means of perturbation theory by setting \mathcal{H}^0 the Hartree-Fock Hamiltonian:

$$\mathcal{H}^0 = \sum_i f(i), \quad (2.35)$$

and the electron correlation as perturbation:

$$\mathcal{H}' = \sum_{ij} \frac{1}{r_{ij}} - \sum_i v^{\text{hf}}(i). \quad (2.36)$$

This treatment of electron correlation is called Møller-Plesset (MP) perturbation theory [38]. The unperturbed wavefunction $\Phi^{(0)}$ is the Hartree-Fock wavefunction, which is an eigenfunction of \mathcal{H}^0 with eigenvalue

$$E_0^{(0)} = \sum_a \varepsilon_a, \quad (2.37)$$

with ε_a the orbital energies. The first-order correction of the energy is according to eq. 2.29:

$$E_0^{(1)} = \langle \Phi^{(0)} | \sum_{i < j} \frac{1}{r_{ij}} | \Phi^{(0)} \rangle - \langle \Phi^{(0)} | \sum_i v^{\text{hf}}(i) | \Phi^{(0)} \rangle. \quad (2.38)$$

The sum of the two terms is the Hartree-Fock energy of 2.16. Consequently, the treatment of electron correlation starts with the second-order correction of the energy. According to Brillouin's theorem, singly excited determinants do not mix with the Hartree-Fock reference, so the singly excited terms vanish and $\Phi_i^{(0)}$ of eq. 2.34 are wavefunctions Φ_{ab}^{rs} , that represent double excitations from orbitals a, b to r, s , with eigenvalue:

$$\mathcal{H}^0 |\Phi_{ab}^{rs}\rangle = \left(E_0^{(0)} - (\varepsilon_a + \varepsilon_b - \varepsilon_r - \varepsilon_s) \right) |\Phi_{ab}^{rs}\rangle. \quad (2.39)$$

The general expression of eq. 2.34 becomes for MP:

$$E_i^{(2)} = \sum_{\substack{a < b \\ r < s}} \frac{\left| \langle \Phi_n^{(0)} | \sum_{i < j} \frac{1}{r_{ij}} | \Phi_{ab}^{rs} \rangle \right|^2}{\varepsilon_a + \varepsilon_b - \varepsilon_r - \varepsilon_s}. \quad (2.40)$$

2.1.4 Density functional theory

Hohenberg-Kohn theorems

The development of density functional theory (DFT) marked the breakthrough in the application of quantum chemical calculations to large systems. It has its roots in the work of Thomas and Fermi on the statistical treatment of electron density in the nineteen twenties [95, 96], but it was in the nineteen sixties that the Hohenberg-Kohn theorems [97] opened the way for its definition as a formally exact theory. [98]

In wavefunction-based methods, the electron density ρ in volume unit (r_1) is obtained by integrating the wavefunction:

$$\rho(r_1) = N \int \int \cdots \int |\Psi(x_1, x_2, \dots, x_N)|^2 ds_1 dx_2 dx_3 \dots dx_N. \quad (2.41)$$

Then, an integration of the electron density over the entire space gives the total number of electrons in the system:

$$N = \int \rho(r) dr. \quad (2.42)$$

The first Hohenberg-Kohn theorem states that the external potential of the system can be defined by the electron density. With the external potential and the number of electrons being known, the electronic Hamiltonian of eq. 2.4 can be reformulated so that its lowest eigenvalue, the ground-state electronic energy of the system, is expressed as a functional of its ground-state electron density:

$$E[\rho] = V_{\text{ne}}[\rho] + T[\rho] + V_{\text{ee}}[\rho]. \quad (2.43)$$

V_{ne} is the energy contribution due to the external potential from the nuclei, T the kinetic energy of the electrons and V_{ee} the electron-electron interaction. The second Hohenberg-Kohn theorem states that for any trial density that integrates to the correct number of electrons, the calculated energy is higher than the energy defined by the exact density. That means that the electron density can be treated variationally. The Hohenberg-Kohn theorems show that in principle it is possible to bypass finding the wavefunction for the description of a system.

Kohn-Sham equations

The introduction of orbitals in DFT by Kohn and Sham [99] was an essential step towards its future wide use: They assume a system of N non-interacting electrons and an external potential v_{eff} such that, when acting on the electrons, it gives rise to an electron density identical to the electron density of the interacting system. In the basis of the separation in a non-interacting and an interacting part, the energy of eq. 2.43 takes the form:

$$E[\rho] = \int v(r_1)\rho(r_1)dr + T_{\text{ni}}[\rho] - \Delta T[\rho] + \frac{1}{2} \iint \frac{\rho(r_1)\rho(r_2)}{r_{12}} dr_1 dr_2 + \Delta V_{\text{ee}}[\rho]. \quad (2.44)$$

The kinetic energy of the electrons is now separated into the kinetic energy in the non-interacting system T_{ni} and the kinetic correlation energy ΔT , which is the difference of the kinetic energy in the real and the non-interacting system. The term of the electron-electron interaction is split into an integral expressing the Coulomb repulsion between densities in two volumes r_1 and r_2 , and a term ΔV_{ee} . The latter comprises correlation and exchange effects, as well as a self-interaction correction for the Coulomb repulsion.

The exchange and correlation terms, ΔV_{ee} and ΔT , form the functional $E_{\text{xc}}[\rho]$, which is linked to an exchange-correlation potential $v_{\text{xc}}(r)$ via:

$$v_{\text{xc}}(r) = \frac{\delta E_{\text{xc}}[\rho(r)]}{\delta \rho(r)}. \quad (2.45)$$

This separation allows for the Hamiltonian to be written as a sum of one-electron Hamiltonians h_i^{KS} :

$$\mathcal{H}^{\text{KS}} = \sum_{i=1}^N h_i^{\text{KS}} = \sum_{i=1}^N \left(-\frac{1}{2} \nabla^2 + v_{\text{eff}}(r_i) \right). \quad (2.46)$$

Solution of the non-interacting system is – analogously to the Hartree-Fock method – a Slater determinant of the Kohn-Sham spin orbitals. The spatial part of the Kohn-Sham orbitals θ_i^{KS} is an eigenfunction of the one-electron operator h_i^{KS} with Kohn-Sham orbital energy $\varepsilon_i^{\text{KS}}$:

$$\left[-\frac{1}{2} \nabla_i^2 + v(r_1)\rho(r_1) + \int \frac{\rho(r_2)}{r_{12}} dr_1 + v_{\text{xc}} \right] \theta_i^{\text{KS}} = \varepsilon_i^{\text{KS}} \theta_i^{\text{KS}}. \quad (2.47)$$

In eq. 2.47, the contributions to the external potential v_{eff} have been separated into non-interacting and interacting. The former include the nuclei-electron interaction and the Coulomb repulsion among electrons; the interacting contributions are collected in the one-electron exchange-correlation potential v_{xc} .

The Kohn-Sham orbitals are determined by solving eq. 2.47 in an iterative procedure with objective the minimization of the electronic energy. It follows from equations 2.47 and 2.44 that the electronic energy is:

$$E[\rho] = - \sum_a z_a \int \frac{\rho(r_1)}{r_{1a}} dr_1 - \frac{1}{2} \sum_{i=1}^N \langle \theta_i^{\text{KS}}(1) | \nabla_1^2 | \theta_i^{\text{KS}}(1) \rangle + \frac{1}{2} \iint \frac{\rho(r_1)\rho(r_2)}{r_{12}} dr_1 dr_2 + E_{\text{xc}}[\rho], \quad (2.48)$$

where the Kohn-Sham orbitals are required to be normalized. Equation 2.48 is in principle exact. Unfortunately, the expression of the unknown exchange-correlation functional for the calculation of E_{xc} is not trivial.

Exchange-correlation functionals

The first approach to the exchange-correlation contribution was the local density approximation (LDA) [100–102]. It assumes a system consisting of a homogeneous electron gas and a uniform positive background that ensures the neutrality of the system.

The electron exchange contribution E_x in this case can be calculated analytically giving for the homogeneous electron gas the Slater (or Dirac) exchange energy:

$$E_x^{\text{Dirac}} = -\frac{3}{4} \left(\frac{3}{\pi} \right)^{1/3} \int \rho^{3/4}(r) dr. \quad (2.49)$$

The kinetic energy of the non-interacting system can also be determined analytically:

$$T_{\text{ni}} = -\frac{3}{10} (3\pi^2)^{2/3} \int \rho^{5/3}(r) dr. \quad (2.50)$$

The correlation energy for the homogeneous electron gas has been accurately calculated by Ceperley and Alder [103] by means of quantum Monte Carlo simulations. This, together with analytical data for the limiting cases of very high and very low density [98], was used in interpolations by Vosko, Wilk, and Nusair who formulated the exchange-correlation energy as a functional of the electron density [102]. The assumption of a constant local electron density as made in LDA is a rather rough approximation for molecules.

A more sophisticated description of the electron density is offered by the generalized gradient approximation (GGA). Here, E_{xc} is expressed as a function of both the density and the density gradient:

$$E_{xc}^{\text{GGA}}[\rho] = \int f(\rho, \nabla\rho) d^3r. \quad (2.51)$$

Some GGA functionals are derived from theoretical arguments only, while others are additionally based on semi-empirical parameters [98]. Perdew-Burke-Ernzerhof (PBE) [104] is an example of purely theoretical functional, in which f of eq. 2.51 is derived from the homogeneous electron gas model and fundamental constants.

Hybrid-functionals mix the exact Hartree-Fock exchange determined with the Kohn-Sham orbitals with exchange from LDA and GGA functionals; the correlation contribution is a combination of LDA and GGA correlation. A great variety of hybrid functionals exists, some of which are semi-empirical, while others purely theoretical. One of the most popular hybrid functionals is B3LYP [26, 27], in which the exchange-correlation energy is calculated according to:

$$E_{xc}^{\text{B3LYP}} = (1-a-b)E_x^{\text{Dirac}} + aE_x^0 + bE_x^{\text{B88}} + (1-c)E_c^{\text{VWN}} + cE_c^{\text{LYP}}. \quad (2.52)$$

B3LYP mixes a fraction of exact exchange E_x^0 with exchange from LDA and the gradient-corrected functional B88 [26]. The correlation is described with a fraction of the LDA parametrization by Vosko *et al.* (E_c^{VWN}) and the GGA functional by Lee *et al.* (E_c^{LYP}) [27]. B3LYP was introduced within the package Gaussian92/DFT [105]. It is a variation of the earlier B3PW, in which the exchange-correlation energy is:

$$E_{xc}^{\text{B3PW}} = (1-a-b)E_x^{\text{Dirac}} + aE_x^0 + bE_x^{\text{B88}} + E_c^{\text{VWN}} + cE_c^{\text{PW91}}. \quad (2.53)$$

The exchange is treated in both functionals alike, and the values for coefficients a , b , c are the same in equations 2.52 and 2.53. The two functionals differ in the treatment

of the correlation contribution: In B3PW, VWN correlation is mixed with the PW91 functional [106]. The parameters $a = 0.20$, $b = 0.72$ and $c = 0.81$ have been obtained from fitting of B3PW results to certain molecular atomization energies, ionization potentials and proton affinities in the G1 set [107], and are adopted in B3LYP.

2.1.5 Electronic structure of solids

The Schrödinger equation for periodic systems

Although finite defective crystals compose most solids in reality, the model used for their quantum chemical description is that of a perfect crystal. A perfect crystal [108] is an infinite periodic system of atoms arranged on a Bravais lattice with basis vectors $\mathbf{a}_1, \mathbf{a}_2, \mathbf{a}_3$, forming the direct lattice with lattice vectors \mathbf{g} :

$$\mathbf{g} = n_1 \mathbf{a}_1 + n_2 \mathbf{a}_2 + n_3 \mathbf{a}_3, \quad (2.54)$$

for which the corresponding reciprocal lattice \mathbf{K} is defined as:

$$\mathbf{K} = k_1 \mathbf{b}_1 + k_2 \mathbf{b}_2 + k_3 \mathbf{b}_3, \quad (2.55)$$

with n_i and k_i integers. The reciprocal lattice basis vectors \mathbf{b}_i are connected to the direct lattice basis vectors:

$$\mathbf{a}_i \mathbf{b}_j = 2\pi \delta_{ij}. \quad (2.56)$$

By definition, a crystal exhibits translational invariance with respect to the direct lattice vectors \mathbf{g} . As the potential energy of the crystal reflects the periodicity of its lattice, the Hamiltonian in the Schrödinger equation is required to exhibit the same periodicity:

$$\mathcal{H}(\mathbf{r})\Psi(\mathbf{r}) = \mathcal{E}\Psi(\mathbf{r}) \equiv \mathcal{H}(\mathbf{r} - \mathbf{g})\Psi(\mathbf{r} - \mathbf{g}) = \mathcal{E}\Psi(\mathbf{r} - \mathbf{g}), \quad (2.57)$$

with Ψ the many-particle wavefunction. Eigenfunctions of Hamiltonian in eq. 2.57 must obey the Bloch theorem [109], which states that:

$$\Phi(\mathbf{r} + \mathbf{g}, \mathbf{k}) = e^{i\mathbf{k} \cdot \mathbf{r}} \Phi(\mathbf{r}, \mathbf{k}), \quad (2.58)$$

and are thus called Bloch functions. Bloch functions that fulfil the periodic boundary conditions of eq. 2.57 are the product of a plane wave with vector \mathbf{k} and a function u which has the same periodicity as the direct lattice \mathbf{g} :

$$\Phi(\mathbf{r}, \mathbf{k}) = e^{i\mathbf{k} \cdot \mathbf{r}} u(\mathbf{r}, \mathbf{k}). \quad (2.59)$$

From the periodic boundary conditions and the Bloch theorem, it follows that the components of the wave vector \mathbf{k} in eq. 2.59 correspond to points of the reciprocal lattice:

$$\mathbf{k}_j = m \mathbf{b}_j, \quad (2.60)$$

with m an integer. The Bloch functions of eq. 2.59 have the same periodicity as the reciprocal lattice. As a result, the description of a crystalline system can be limited to

the first Brillouin zone [110].

The Schrödinger equation for solids is solved in the self-consistent field approximation, discussed in section 2.1.2. The eigenfunctions of the one-electron Hamiltonian of the periodic system, single-particle wavefunctions called crystalline orbitals, are linear combinations of Bloch functions with coefficients $C_{\mu n}$:

$$\Psi_n(\mathbf{r}, \mathbf{k}) = \sum_{\mu} C_{\mu n} \Phi(\mathbf{r}, \mathbf{k}). \quad (2.61)$$

Bloch functions can be constructed from plane waves or atomic orbitals, and both methods are employed in quantum chemical codes for solids. Latter is the case in the CRYSTAL09 software package [55, 56], which has been employed for the DFT and Hartree-Fock calculations throughout this work; for this reason, the discussion here is limited to LCAO-crystalline orbitals. For an atomic orbital $\phi(\mathbf{r}_n)$ centred in the atomic position \mathbf{r}_n of the 0-cell, and $\phi_n^{\mathbf{g}}(\mathbf{r})$ its equivalent atomic orbitals in cell \mathbf{g} , the Bloch function constructed from the linear combination of these orbitals is:

$$\Phi_n(\mathbf{r}, \mathbf{k}) = \frac{1}{\sqrt{N}} \sum_{\mathbf{g}} e^{i\mathbf{k} \cdot \mathbf{g}} \phi_n^{\mathbf{g}}(\mathbf{r}). \quad (2.62)$$

The Schrödinger equation is solved in an iterative procedure analogous to that for non-periodic systems. In matrix representation, eq. 2.57 takes the form:

$$\mathbf{F}(\mathbf{k})\mathbf{C}(\mathbf{k}) = \mathbf{S}(\mathbf{k})\mathbf{C}(\mathbf{k})\mathbf{E}(\mathbf{k}). \quad (2.63)$$

The coefficients of the linear combination 2.61 are stored in matrix \mathbf{C} , and the overlap of the basis functions in matrix \mathbf{S} . Bloch functions Φ_{μ} that correspond to different reciprocal lattice points \mathbf{k} are mutually orthogonal. As a consequence, the Schrödinger equation for a crystalline system can be solved for each \mathbf{k} -point separately.

Periodic local MP2

Among the possibilities to overcome the computational cost involved in wavefunction-based methods for electron correlation is the use of local, instead of canonical, orbitals as is done for example in local MP2 [111]. The computational cost of perturbation theory as formulated in section 2.1.3 follows a scaling of $\mathcal{O}(n^5)$ with the number of electrons n in a system, which is prohibitive for the calculation of large systems. However, for a given occupied orbital, only the virtual orbitals which have a significant overlap with it contribute to the correlation. This is exploited in the localized description: The virtual space is truncated into an excitation domain only involving virtual orbitals in the close proximity of the corresponding occupied one. Moreover, taking into account the short-ranged nature of electron correlation ($\propto r^{-6}$), pairs need to be taken into account only up to a certain distance. The local MP2 scheme, first proposed by Saebo and Pulay [112], combined with integral-direct techniques reduces the computational effort to a linear scaling [113], making its use feasible on large systems.

Local MP2 has been implemented for solids in the CRYSCOR package [39, 40]. The occupied space is described in CRYSCOR with a set of orthonormal Wannier functions [114], which are derived from the localization of the canonical Bloch functions provided by CRYSTAL [115, 116]. The virtual space is spanned with projected atomic orbitals, created by projecting the atomic orbitals of an excitation domain against the occupied subspace and each other [117]. The projected atomic orbitals form a non-orthogonal set, but are orthogonal to the Wannier functions and well-localized.

The correlation energy of a pair \mathbf{i}, \mathbf{j} is:

$$E_{ij}^{\text{LMP2}} = \sum_{\mathbf{a}, \mathbf{b} \text{ in } [\mathbf{i}, \mathbf{j}]} K_{\mathbf{ab}}^{\mathbf{ij}} (2T_{\mathbf{ab}}^{\mathbf{ij}} - T_{\mathbf{ba}}^{\mathbf{ij}}), \quad (2.64)$$

where the Wannier function \mathbf{i} is in the 0-cell and \mathbf{j} can be in principle anywhere in space. \mathbf{a} and \mathbf{b} are the projected atomic orbitals in the excitation domains for \mathbf{i} and \mathbf{j} . K are the electron repulsion integrals and T the corresponding LMP2 amplitudes. K and T decay with r^{-3} , leading to the energy decay of r^{-6} , that allows for a cutoff in the sum of eq. 2.64. Pairs are classified according to a distance criterion into strong, weak, and distant, and are treated at different levels [39]. A detailed derivation of the expression for the energy correction, as well as an extensive discussion on the implementation of LMP2 can be found in the Cryscor User's Manual [118].

2.2 Long-range effects

2.2.1 Dipole-dipole interaction

In addition to the interactions that arise from the overlap of wavefunctions, long-range effects are of significance in extended systems as well. These are electrostatic, dispersion, and induction interactions. While electrostatic forces are positive or negative depending on the sign of the charges, dispersive and induction forces are always attractive [119]. Induction is partly accounted for in Hartree-Fock, but dispersion interactions are a consequence of electron correlation, so they can be treated by means of perturbation theory.

In a system AB with unperturbed Hamiltonian $\mathcal{H}^0 = \mathcal{H}^A + \mathcal{H}^B$ which has the eigenvalue $E^A + E^B$, the electrostatic interaction is regarded as perturbation between the electron distributions:

$$\mathcal{H}' = \int \frac{\hat{\rho}^A(\mathbf{r})\hat{\rho}^B(\mathbf{r})}{|\mathbf{r} - \mathbf{r}'|} d^3\mathbf{r} d^3\mathbf{r}'. \quad (2.65)$$

For the description of the charge distributions, it is convenient to express them as a multipole expansion:

$$\mathcal{H}' = T q^A q^B + T_\alpha (q^A \hat{\mu}_\alpha^B - \hat{\mu}_\alpha^A q^B) + T_{\alpha\beta} \left(\frac{1}{3} q^A \hat{\Theta}_{\alpha\beta}^B - \hat{\mu}_\alpha^A \hat{\mu}_\beta^B + \frac{1}{3} \hat{\Theta}_{\alpha\beta}^A q^B \right) + \dots, \quad (2.66)$$

with $T_\nu = \nabla_\alpha \dots \nabla_\nu \frac{1}{r}$, q the total charge, μ the dipole moment and Θ the quadrupole moment [119].

The first-order correction of the energy, as defined in eq. 2.38, corresponds to the classical electrostatic interaction of the electron distributions:

$$E^{(1)} = \langle \Phi_A^0 \Phi_B^0 | \mathcal{H}' | \Phi_A^0 \Phi_B^0 \rangle = \int \frac{\rho^A(\mathbf{r})\rho^B(\mathbf{r}')}{|\mathbf{r} - \mathbf{r}'|} d^3\mathbf{r} d^3\mathbf{r}'. \quad (2.67)$$

The second-order correction of the ground-state energy is in accordance with eq. 2.34:

$$E_{00}^{(2)} = \sum_{\substack{mn \\ m \text{ or } n \neq 0}} \frac{|\langle 00 | \mathcal{H}' | mn \rangle|^2}{E_{00}^0 - E_{mn}^0}, \quad (2.68)$$

with m and n the excited states of subsystem A and B respectively. The terms of eq. 2.68 can be separated into induction (for $m = 0$ or $n = 0$) and dispersion (for $m, n \neq 0$) contributions.

If expression 2.66 is truncated after the dipole terms, the dispersion energy becomes proportional to r^{-6} , r being the distance between the fragments considered. The dispersion energy E_{disp} can be expressed as a function of ionization energies I_p and polarizabilities α of species A and B :

$$E_{\text{disp}}^{[6]} \approx -\frac{3I_p^A I_p^B}{2(I_p^A + I_p^B)} \frac{\alpha^A \alpha^B}{r^6}, \quad (2.69)$$

which is the London equation for the dispersion interaction [120].

An alternative approach gives an expression of the dispersion interaction in terms of polarizabilities at an imaginary frequency $i\omega$ [121]:

$$E_{\text{disp}}^{[6]} = -\frac{3}{\pi r^6} \int_0^\infty \alpha^A(i\omega) \alpha^B(i\omega) d\omega. \quad (2.70)$$

In equations 2.69 and 2.70, α refers to the average polarizabilities and the superscript in $E_{\text{disp}}^{[6]}$ indicates that only interactions up to dipole-dipole are taken into account.

2.2.2 Dispersion correction for DFT

Due to its low computational cost, DFT is the method of choice for the calculation of large and extended systems. It is thus a drawback, that it does not sufficiently account for dispersion effects. A long-range dispersion correction (D2) for different functionals was presented by Grimme and co-workers in 2006 [53]. It calculates a semi-empirical correction of the form:

$$E_{\text{disp}}^{\text{D2}} = -s_6 \sum_{i=1}^{n-1} \sum_{j=i+1}^n \frac{C_{ij}^{[6]}}{r_{ij}^6} f_{\text{dmp}}(r_{ij}^6). \quad (2.71)$$

The dispersion energy in D2 consists of a sum of pair interactions with r^{-6} dependence, a global factor s_6 that depends on the density functional used, and a damping function $f_{\text{dmp}}(r_{ij}^6)$ that prevents the correction from taking large negative values at short distances, which are already treated correctly by DFT.

Key to the success of the dispersion correction is the choice of $C_{ij}^{[6]}$ coefficients. At the same time, their global determination is problematic, as they strongly depend on the particular binding situation in every system. Following the London dispersion formula, the atomic coefficients are defined in D2 as:

$$C_i^{[6]} = 0.05NI_p^i\alpha^i. \quad (2.72)$$

The ionization potential I_p and polarizability α are calculated with DFT/PBE0. However, their product is then scaled by 0.05 and by a factor N that depends on the row of the atom in the periodic table. The atomic coefficients of eq. 2.72 are used to calculate the pair coefficients:

$$C_{ij}^{[6]} = \sqrt{C_i^{[6]}C_j^{[6]}}. \quad (2.73)$$

D3, a development of the dispersion correction for density functionals was presented by Grimme and co-workers in 2010 as a “more sophisticated and less empirical scheme” [54]. It includes higher multipole terms for the pair interactions ($C^{[8]}$ and $C^{[10]}$), as well as three-body terms. The coefficients are calculated based on the Casimir-Polder formula (2.70) by means of time-dependent DFT with a modified PBE0 functional. In particular, to achieve a consistent description of the atoms throughout the periodic table, the polarizabilities of hydrides of all elements are calculated and the coefficients are determined according to:

$$C_{AB}^{[6]} = -\frac{3}{\pi} \int_0^\infty \frac{1}{m} \left(\alpha^{A_m H_n}(i\omega) - \frac{n}{2} \alpha^{H_2}(i\omega) \right) \times \frac{1}{k} \left(\alpha^{B_k H_l}(i\omega) - \frac{l}{2} \alpha^{H_2}(i\omega) \right) d\omega. \quad (2.74)$$

An interpolation scheme is then used to define coordination-adopted dispersion coefficients. The coordination number of A and B in the hydrides of eq. 2.74 is determined based on the values for the covalent radii proposed by Pyykkö and Atsumi [122], but is then scaled by a factor of 4/3 for use in D3. The coefficients for higher-order terms are calculated according to recursive formulas based on multipole expansions for hydrogen and helium [123], which can be in principle extended to heavier atoms [124]. In the D3 scheme, these parameters are “[...] chosen for convenience such that reasonable $C_{AA}^{[8]}$ values for He, Ne and Ar are obtained” (Grimme *et al.* [54]). The three-body contribution in D3 is derived from third-order perturbation theory:

$$E_{ABC}^{D3} = \sum_{ABC} f_{\text{dmp},3}(\bar{r}_{ABC}) \frac{C_{ABC}^{[9]} (3 \cos \theta_a \cos \theta_b \cos \theta_c + 1)}{(r_{AB} r_{BC} r_{CA})^3}, \quad (2.75)$$

with θ and r the angles and edges of the triangle formed by atoms A , B and C . $f_{\text{dmp},3}(\bar{r}_{ABC})$ is a dumping function that depends on the geometrical average of r_{AB} , r_{BC} and r_{CA} . Instead of being calculated from the polarizabilities, the coefficient $C_{ABC}^{[9]}$ is approximated as the geometrical mean of the corresponding two-body coefficients:

$$C_{ABC}^{[9]} = -\sqrt{C_{AB}^{[6]}C_{BC}^{[6]}C_{AC}^{[6]}}. \quad (2.76)$$

2.2.3 Electrostatic contributions in periodic systems

In a periodic system of unit cell with volume $V = l^3$ and particles i, j , the electrostatic interaction E_{Coul} between particles in the \mathbf{n} -th periodic images of the system is given by:

$$E_{\text{Coul}} = \frac{1}{2} \sum_{\substack{i,j,\mathbf{n} \\ \mathbf{n}=0:i \neq j}} \frac{q_i q_j}{|\mathbf{r}_{ij} + \mathbf{n}l|}. \quad (2.77)$$

The indices i and j run over the particles in the zeroth cell. The vector $\mathbf{n}l$ expresses the translation to the neighbouring cells, thus including all pair interactions in the periodic system, while the condition $i \neq j$ for $\mathbf{n} = 0$ takes care of self-interaction. Due to the poor convergence of the sum in eq. 2.77, the electrostatic contribution cannot be calculated directly. A number of methods have been developed to address this problem, but probably the most widely used – at least for ionic solids – is also the predecessor of all others: the Ewald summation [125].

For every particle with charge q_i , a screening charge density is introduced with opposite sign. The screening charges can have any shape, but following the formulation by Frenkel and Smit [126], the densities are chosen to have the form of Gaussians with width $\sqrt{2/\alpha}$:

$$\rho(r) = -q_i \left(\frac{\alpha}{\pi} \right)^{3/2} \exp(-\alpha \mathbf{r}^2). \quad (2.78)$$

In contrast to the original sum, the electrostatic energy due to the screened charges converges rapidly, hence it can be calculated easily with direct-lattice summation:

$$E_{\text{scr}} = \frac{1}{2} \sum_{i \neq j}^N q_i q_j \frac{\text{erfc}(\sqrt{\alpha} r_{ij})}{r_{ij}}. \quad (2.79)$$

A compensating charge distribution is introduced to correct for the added screening charges. It consists of a sum of Gaussians:

$$\rho_1(r) = \sum_{j,\mathbf{n}} q_j \left(\frac{\alpha}{\pi} \right)^{3/2} \exp\left(-\alpha |\mathbf{r} - (\mathbf{r}_j + \mathbf{n}l)|^2\right). \quad (2.80)$$

Sum 2.80 is periodic and varies smoothly in space. The electrostatic energy due to the compensating charges E_{comp} is thus calculated in the reciprocal space as:

$$E_{\text{comp}} = \frac{1}{2V} \sum_{\mathbf{k} \neq 0} \frac{4\pi}{k^2} |\rho(\mathbf{k})|^2 \exp\left(\frac{-k^2}{4\alpha}\right). \quad (2.81)$$

E_{comp} as given in eq. 2.81 includes self-interaction between a Gaussian distribution with charge q_i and the point charge q_i in its center. The self-interaction has the value:

$$E_{\text{self}} = \sqrt{\frac{\alpha}{\pi}} \sum_i q_i^2. \quad (2.82)$$

Finally, from equations 2.79, 2.81 and 2.82, the Coulomb energy in a periodic system can be calculated as a combination of a direct- and a reciprocal-space sum:

$$\begin{aligned} E_{\text{Coul}} &= E_{\text{scr}} + E_{\text{comp}} - E_{\text{self}} \\ &= \frac{1}{2} \sum_{i \neq j}^N q_i q_j \frac{\text{erfc}(\sqrt{\alpha} r_{ij})}{r_{ij}} + \frac{1}{2V} \sum_{\mathbf{k} \neq 0} \frac{4\pi}{k^2} |\rho(\mathbf{k})|^2 \exp\left(\frac{-k^2}{4\alpha}\right) - \sqrt{\frac{\alpha}{\pi}} \sum_i q_i^2. \end{aligned} \quad (2.83)$$

The value of α controls the convergence of the sums in equations 2.79 and 2.81. When α is chosen large, the Gaussian charge distribution is narrow and the direct-space sum converges rapidly. On the other hand, the reciprocal-space sum converges rapidly for small values of α [127].

To this point, no approximations have been made. However, truncation of the series in the direct and reciprocal space are required for their calculation. The accuracy of the Ewald summation depends on the choice of direct- and reciprocal-space cutoff, r_{max} and k_{max} . The errors of the direct-space contribution δE_{real} and of the reciprocal-space contribution δE_{rec} are estimated as:

$$\delta E_{\text{real}} \propto \exp(\alpha^2 r_{\text{max}}^2), \quad \delta E_{\text{rec}} \propto \exp\left(-\frac{\pi^2 k_{\text{max}}^2}{\alpha^2 l^2}\right). \quad (2.84)$$

The two errors are kept in same order of magnitude [128] when the cutoff values r_{max} and k_{max} are chosen according to:

$$k_{\text{max}} = \frac{\alpha^2 r_{\text{max}} l}{\pi}. \quad (2.85)$$

2.3 Surface thermodynamics

The chemical potential

The thermodynamic quantity that describes the spontaneity of a process at conditions of constant temperature and pressure is the Gibbs energy G . For a closed monophasic system, it is linked to the inner energy U , entropy S , temperature T , pressure P , and volume V according to:

$$G = U - TS + PV. \quad (2.86)$$

Processes in a system occur spontaneously if they give rise to a decrease in the Gibbs energy [129]. In a multiphase system with phases j and components i , the change in the total Gibbs energy dG^{tot} is given by:

$$dG^{\text{tot}} = - \sum_j S^j dT + \sum_j V^j dP + \sum_j \sum_i \mu_i^j dn_i^j. \quad (2.87)$$

The term involving the chemical potential μ_i^j arises from the fact that the system described by eq. 2.87 does not consist of closed phases; an exchange of particles between

phases is allowed. If pressure and temperature are kept constant, eq. 2.87 reduces to:

$$(\mathrm{d}G^{\mathrm{tot}})_{T,P} = \sum_j \sum_i \mu_i^j \mathrm{d}n_i^j, \quad (2.88)$$

so the processes in the system are determined only by the chemical potential of the components in the different phases. The chemical potential is thus the intensive analogue to the Gibbs energy:

$$\mu = \left(\frac{\partial G}{\partial n} \right)_{T,P}, \quad (2.89)$$

therefore a function of temperature and pressure. For a system in equilibrium, it holds that $\mathrm{d}G^{\mathrm{tot}} = 0$. Considering a system with two phases a and b , this condition takes the form:

$$\sum_i \mu_i^a \mathrm{d}n_i^a + \sum_i \mu_i^b \mathrm{d}n_i^b = 0. \quad (2.90)$$

In equilibrium, the same number of particles of a species is transferred from a to b as from b to a : $\mathrm{d}n_i^a = -\mathrm{d}n_i^b$. Then, according to eq. 2.90, the chemical potential of a component i must be equal in both phases of the system:

$$\mu_i^a = \mu_i^b. \quad (2.91)$$

In statistical mechanics, the chemical potential of a system with N particles and volume V can be calculated from the total partition function Q via:

$$\mu = -RT \left(\frac{\partial \ln Q}{\partial N} \right)_{V,T}, \quad (2.92)$$

with R the universal gas constant. In a system of indistinguishable particles following Boltzmann statistics, e.g. the ideal gas, the total partition function is:

$$Q(N, T, V) = \frac{(q(V, T))^N}{N!}, \quad (2.93)$$

with q the one-particle partition function. According to Sterling's approximation [130], the logarithm of the total partition function can be written as:

$$\ln Q \approx N \ln q - N \ln N + N. \quad (2.94)$$

In the ideal gas limit, the one-particle partition function q is proportional to the volume and the quantity $q(V, T)/V$ depends only on temperature. Taking this into account and using $k_B T/P = V/N$, the chemical potential of the ideal gas is written as:

$$\mu_{\text{ideal gas}} = -RT \ln \left(\frac{q}{V} k_B T \right) + RT \ln P. \quad (2.95)$$

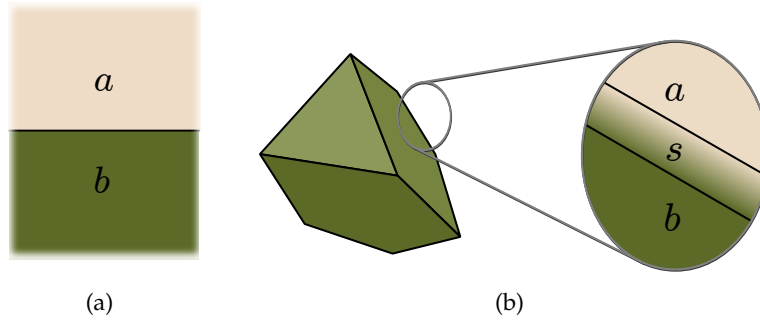


Figure 2.1: Treatment of interfaces in thermodynamics. (a) The interface as mathematical surface separating two homogeneous phases. (b) The interface as a non-homogeneous phase.

Surface energy

Until now, the system was discussed only with regard to the bulk phases; no information whatsoever was included about the interface between the phases. Two possibilities to treat an interface are illustrated in fig. 2.1. The first, shown in fig. 2.1(a), was originally proposed by J.W.Gibbs [131]. The interface is regarded as a strictly two-dimensional boundary separating two perfectly homogeneous bulk phases. An alternative approach, introduced by Guggenheim [132] based on previous work of van der Waals Jr. and Baker, is shown in fig. 2.1(b). Here, the interface is regarded as a distinct, non-homogeneous phase, each limit of which shares the properties of the neighbouring bulk phase so that the phase transitions are continuous. Both models can be employed to derive expressions for the thermodynamics of interfaces. In the Gibbs model, the interface is a mathematical construct, so its thermodynamic properties need to be defined explicitly. In the Guggenheim model, the properties of the interface are derived from standard thermodynamic considerations. It offers a more intuitive treatment, therefore it will be used in the following to derive an expression for the interface energy.

The total Gibbs energy of the system in fig. 2.1(b) is

$$G^{\text{tot}} = G^a + G^s + G^b, \quad (2.96)$$

or using the chemical potential

$$\sum_j \sum_i n_i^j \mu_i^j = \sum_i n_i^a \mu_i^a + \sum_i n_i^s \mu_i^s + \sum_i n_i^b \mu_i^b. \quad (2.97)$$

The Gibbs energy of the surface G^s in equations 2.96 depends on the area of the interface. Instead of normalizing it with respect to the number of particles, it is more sensible to define an area-specific surface energy γ . If γ is defined as the surface energy per area unit, and A the area of the interface, eq. 2.96 becomes:

$$\gamma = \frac{1}{A} (G^{\text{tot}} - G^a - G^b). \quad (2.98)$$

In quantum chemical modelling, the calculation of surface energy is based on eq. 2.98. However, instead of calculating a Gibbs surface energy γ , pure electronic energy values are usually used for the calculation, although corrections for vibrational energy can be in principle included from first principles. If the system consists only of a solid phase in vacuum, the electronic surface energy is calculated as:

$$E^s = \frac{1}{2A} (E^{\text{slab}} - nE^{\text{bulk}}). \quad (2.99)$$

E^{slab} is the energy of a slab consisting of n formula units and E^{bulk} the energy per formula unit in bulk. The factor $1/2$ in eq. 2.99 emerges as a consequence of the modelling of the solid as a symmetric slab. The intensive bulk energy E^{bulk} is multiplied by the number of “molecules” n in the slab (see section 3.2 for details on the slab model).

Unfortunately, as soon as adsorbates are introduced on the surface, eq. 2.99 ceases to be valid, due to the inhomogeneity of the treated solid phase: Having modified the surface of the slab by adding adsorbates, it is not possible to define an infinite bulk corresponding to the slab. From a thermodynamic point of view, the presence of adsorbates on the surface implies – instead of vacuum as modelled by first principles – the existence of a second phase. Expressing the Gibbs energy of the adsorbates as $G^{\text{ads}} = \sum_i \mu_i^{\text{ads}} n_i^{\text{ads}}$, one uses the chemical potential to attribute a temperature and a pressure to the implied gas phase; the temperature and pressure, in turn, determine the Gibbs energy of the adsorbates. This is, naturally, only true when the phases of the system are in equilibrium, thus eq. 2.91 is valid. In this case, the temperature- and pressure-dependent surface energy is obtained via:

$$\gamma = \frac{1}{2A} \left(G^{\text{slab}} - n^{\text{bulk}} \mu^{\text{bulk}} - \sum_i n_i^{\text{ads}} \mu_i^{\text{ads}} \right). \quad (2.100)$$

All terms in eq. 2.100 are Gibbs energies. Nonetheless, when combining quantum chemical calculations to surface thermodynamics it is a reasonable approximation to neglect the vibrational degrees of freedom for the solid terms: Firstly, the vibrational contributions to the total energy are significantly smaller than the electronic energy. Secondly, the vibrational contributions are expected not to differ significantly between slab and bulk, so can be assumed to cancel each other out. That allows for substituting G^{slab} and G^{bulk} with the corresponding electronic energies, which also enter eq. 2.99.

Wulff construction

In the beginning of the section, it was mentioned that a system tends towards the direction that minimizes its Gibbs energy. In the case of a biphasic system with phases of constant volume and constant number of particles, this corresponds to minimizing the energy of the interface:

$$\min_{\gamma(\mathbf{n})} \left(\int \gamma(\mathbf{n}) dA \right). \quad (2.101)$$

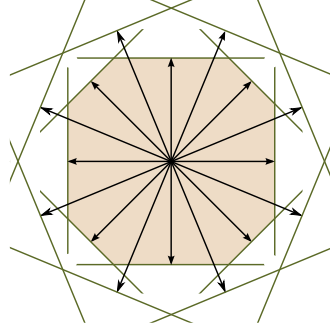


Figure 2.2: Two-dimensional pictorial scheme of the Wulff construction. Polar plot of the surface energies (black vectors). The green lines correspond to the Wulff planes. The inner envelope in beige corresponds to the equilibrium shape of the crystal.

If γ is independent of the orientation \mathbf{n} , eq. 2.101 is minimized by minimizing the area A . This is the case for fluids. By contrast, the surface energy of crystals strongly depends on the orientation of the surface under consideration, which is expressed by the Miller indices (hkl) . This complicates the minimization of the integral.

G. Wulff published in 1901 a detailed account on his experimental investigation on crystal growth [133], in which he determined the orientation-dependent growth rate of $\text{Zn}(\text{NH}_4)\text{SO}_4 \cdot 6 \text{H}_2\text{O}$ in solution. Comparing his findings to previous works, Wulff concluded that the growth rate of a crystal towards a given direction is proportional to the corresponding surface energy. This is the solution for the problem in eq. 2.101: As Wulff writes, “the minimum surface energy of a polyhedron at constant volume is reached when the distance of its surfaces from a given point is proportional to the surface tension of these surfaces” [133]. This becomes clear considering the process of crystal growth: As the crystal grows towards a given direction, the surface normal to this direction advances away from the centre of mass of the crystal, while the neighbouring surfaces expand laterally. As a result, the exposure of the former continuously decreases.

The graphical determination of the equilibrium shape of a crystal based on surface energies is known as *Wulff construction*. A short but very informative explanation of the Wulff construction can be found in ref. [32]. The construction is demonstrated in fig. 2.2: In a polar diagram, the surface energies are plotted as vectors with magnitude $\gamma(hkl)$ and orientation (hkl) . Then, normal planes are drawn to the radius vectors. The inner envelope of the drawn planes represents the shape for which the crystal minimizes its surface energy.

3 Computational methods

3.1 General remarks

The computational methods used in the present work have been described in detail in the corresponding sections of papers **P1** and **P2**. This chapter provides background information on certain aspects and in addition covers topics that are not published elsewhere: Section 3.2 is concerned with the modelling of surfaces within the periodic approach, providing information for readers not familiar with solid state quantum chemistry. The calculation of the chemical potential for surface thermodynamics is discussed in section 3.3, including details complementary to the computational section of paper **P2**. A topic not published elsewhere is introduced in section 3.4, concerning the computational aspects of the parametrization of classical force fields. Regarding the quantum chemical calculations, convergence criteria and other parameters are introduced in the corresponding papers. Unless explicitly mentioned otherwise, periodic calculations are performed using the CRYSTAL09 [55, 56] code for Hartree-Fock and DFT; the CRYSCOR09 [39, 40] code is employed for periodic local MP2 calculations. The latter will be referred to in the following as *MP2* for simplicity. With the exception of certain tests published in **P1**, where it is explicitly stated, the B3LYP functional [26, 27] is used for the DFT calculations. These are mentioned throughout this work plainly as *DFT*.

3.2 Model of the surfaces

The surfaces have been modelled with the CRYSTAL09 quantum chemical package for periodic systems. Slabs in CRYSTAL09 are cut from the three-dimensionally periodic bulk, and are periodic in the two directions along the cutting plane; in the third direction the system is non-periodic (fig. 3.1). Termination and thickness of the slabs have been chosen to always preserve a symmetry plane normal to the *z*-axis. This way, no measures need to be taken to prevent reconstruction during structure optimization. Based on previous calculations [28], low-index slabs of a thickness of 12 MgF_2 units have been chosen. Due to the differences of the sequence and composition of the atomic layers along each direction, the MgF_2 layers correspond to different number of atomic layers in each slab. Atomic layers include atoms that share the same value of *z*-coordinate. (001) is a non-polar surface, so (001) slabs consist of 12 stoichiometric atomic layers. The other low-index surfaces are polar, with the corresponding slabs being built of different sequences of charged atomic layers: slab (100) consists

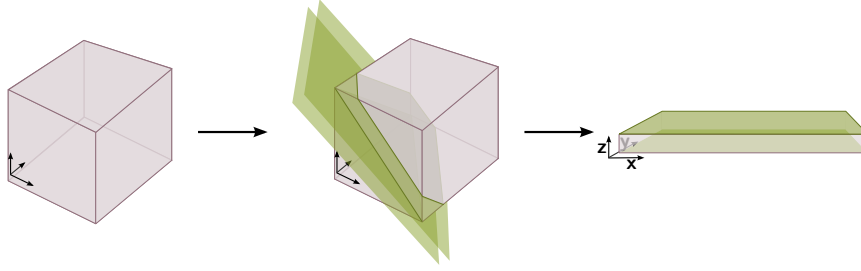


Figure 3.1: Pictorial representation of the construction of the slab from a 3-dimensional periodic bulk. Pink planes imply periodic continuity in the corresponding direction, green planes represent non-periodic directions.

of 36 atomic layers with sequence F-Mg-F, (110) of 18 atomic layers with sequence F-(Mg,Mg,F,F)-F and (101) of 18 atomic layers with sequence (F,F)-(Mg,Mg)-(F,F). The structure along vicinal directions will be discussed in detail in sec. 4.2.

3.3 Surface thermodynamics

3.3.1 Calculation of the chemical potential

In most cases, thermodynamic quantities have standard temperature as a reference point. To combine the chemical potential to quantum chemical quantities, one needs to refer it to 0 K. This is done by expressing it as:

$$\mu_i(p_i, T) = E_{i,\text{electr.}} + \Delta\mu_i^{p^0}(T) + kT \ln \frac{p_i}{p^0}. \quad (3.1)$$

Eq. 3.1 differs from eq. 2.95 of section 2.3 in the units; 3.1 refers to one molecule whereas 2.95 to 1 mol. The first term of eq. (3.1) is the electronic energy of species i , which is regarded as the Gibbs energy at zero Kelvin, neglecting the vibrational and rotational contributions. The third term of eq. 3.1 is the pressure-dependent contribution to the chemical potential, with k the Boltzmann constant. The second term expresses the temperature dependence of μ_i and is not as straight-forward as the other two. It can be calculated directly from eq. 2.95 and the partition function by means of statistical mechanics, but it is usually – also in this work – calculated based on listed values for thermodynamic quantities [134]. $\Delta\mu_i^{p^0}(T)$ refers to the change of the chemical potential of the component i of a system when the temperature is increased from 0 K to T , at constant pressure $p^0 = 1$ atm. It is calculated using tabulated values in a number of steps, demonstrated in the following.

Standard values for thermodynamics are listed in the NIST database [135], in the form of polynomials for the heat capacity, standard enthalpy and standard entropy as a function of temperature. These polynomials (equations 3.2 and 3.3), known as the Shomate equation, are the result of fits to experimental values:

$$H^\circ - H_{298.15}^\circ = At + \frac{Bt^2}{2} + \frac{Ct^3}{3} + \frac{Dt^4}{4} - \frac{E}{t} + F - H, \quad (3.2)$$

$$S^\circ = A \ln \frac{t}{[\text{K}]} + Bt + \frac{Ct^2}{2} + \frac{Dt^3}{3} - \frac{E}{2t^2} + G. \quad (3.3)$$

The factors entering the equations for H_2O and HF are listed in table 3.1, and t is an expression of temperature in Kelvin: $t = \frac{T\text{K}}{1000}$.

Table 3.1: Values used to calculate $\Delta\mu_i^{p_0}(T)$. Factors A to H give $H^\circ - H_{298.15}^\circ$ in kJ/mol and S° in J/molK. The quantity $H^\circ - H_0^\circ$ is in kJ/mol.

	H_2O	HF
$A / \text{Jmol}^{-1}\text{K}^{-1}$	30.09200	30.11693
$B / \text{Jmol}^{-1}\text{K}^{-2}$	6.832514	-3.246612
$C / \text{Jmol}^{-1}\text{K}^{-3}$	6.793435	2.868116
$D / \text{Jmol}^{-1}\text{K}^{-4}$	-2.534480	-1.243874
E / kJKmol^{-1}	0.082139	-0.024861
F / kJmol^{-1}	-250.8810	-281.4912
$G / \text{Jmol}^{-1}\text{K}^{-1}$	223.3967	210.9226
H / kJmol^{-1}	-241.8264	-272.5462
$H^\circ - H_0^\circ$	9.905	8.599

Since these data are referred to the standard temperature, the quantity $H^\circ - H_0^\circ$ is additionally needed. It is calculated by direct summation over vibrational levels of the ground electronic state of HF and H_2O and is tabulated in [136]. Using equations 3.2–3.3 and the values listed in table 3.1, the temperature contribution to the chemical potential is calculated as:

$$\Delta\mu_{0 \rightarrow T} = (H_{298.15}^\circ - H_0^\circ) + (H^\circ - H_{298.15}^\circ) - S^\circ T. \quad (3.4)$$

Using the expression for the chemical potential as a function of temperature and pressure, the surface energy at finite temperature and pressure can be calculated following the considerations of section 2.3. For the system $\text{MgF}_2/\text{HF}/\text{H}_2\text{O}$ the surface energy is calculated via:

$$\begin{aligned} \gamma(T, p_{\text{HF}}, p_{\text{H}_2\text{O}}, p_{\text{tot}}) = & \frac{1}{2A} \left[E_{\text{slab}}^{\text{DFT}}(T, p_{\text{tot}}) - N_{\text{Mg}} E_{\text{MgF}_2\text{-bulk}}^{\text{DFT}}(T, p_{\text{tot}}) \right. \\ & - (N_{\text{HF}} - N_{\text{OH}}) \mu_{\text{HF}}(T, p_{\text{HF}}) \\ & \left. - (N_{\text{H}_2\text{O}} + N_{\text{OH}}) \mu_{\text{H}_2\text{O}}(T, p_{\text{H}_2\text{O}}) \right]. \end{aligned} \quad (3.5)$$

For a detailed derivation of eq. 3.5, the reader is referred to paper **P2**.

3.4 Parametrization of classical force fields

The parametrization of the classical force field to fit the DFT energy is performed in the three-dimensional periodic system and is based on the energy-volume equation

of states (EOS) of the rutile-type MgF_2 bulk. The structures for the EOS are derived from the fully relaxed bulk of rutile-type MgF_2 by uniformly expanding the lattice; 20 structures in the range between 0.80 and 1.20 of the equilibrium volume of the unit cell are calculated. The periodic DFT calculations are performed with the CRYSTAL14 code [137, 138] using the keyword EOS. It takes care of the expansion of the lattice and ensures that the selection criteria for the Coulomb and exchange integrals are frozen to those of the reference geometry throughout the series of calculations, thus minimizing computational noise.

It will be explained in detail in section 4.5 that for the modelling of bulk MgF_2 using classical force fields, it is necessary to split the energy into a sum of electrostatic and a sum of short-range interactions, individually evaluating each of the two and consequently summing them to obtain the total energy.

The short-range pair interactions in MgF_2 are described as Buckingham potentials [139], with the modification that the pair-specific coefficients are written as products of ion-specific parameters:

$$E_{ij}^{\text{Buck}} = b_i b_j \exp\left(\frac{-r_{ij}}{\rho}\right) - \frac{d_i d_j}{r_{ij}^6} \quad (3.6)$$

This way, the parameters entering the pair potentials are reduced from seven to five, thus accelerating the minimization procedure.

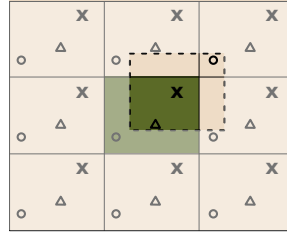


Figure 3.2: The minimum image convention, here shown for atom **x**. Only interactions between the atoms inside the dashed box (simulation box centred at **x**) are taken into account. The original simulation box is shown in green and its periodic images in beige.

The evaluation of the short-range contribution is performed via direct-lattice summation after imposing periodic boundary conditions, using the minimum image convention, illustrated in fig. 3.2. The simulation boxes are chosen to contain $2 \times 2 \times 2$ or $3 \times 3 \times 3$ unit cells, corresponding to a size of $(9.3344 \times 9.3344 \times 6.1658) \text{ \AA}$ and $(14.0016 \times 14.0016 \times 9.2488) \text{ \AA}$, respectively. The Matlab package MolDynSim [140] is employed for the calculation of the short-range contribution.

The electrostatic contribution is evaluated in periodic boxes containing $2 \times 2 \times 2$ unit cells via Ewald summation [125], as implemented in the molecular dynamics package OpenMM6.2 [141]. The values for the ionic charges $z_{\text{Mg}} = 1.66$ and $z_{\text{F}} = -0.83$ are derived from the DFT calculation for the fully optimized bulk via Mulliken population analysis [142]. In addition to the charges and periodic box, OpenMM requires

the definition of the direct space cutoff r_{\max} and a parameter δ , which corresponds to the desired accuracy. These are used to determine the value of parameter α , which controls the width of the Gaussians:

$$\alpha = \frac{\sqrt{-\log(2\delta)}}{r_{\text{cutoff}}}. \quad (3.7)$$

Consequently, based on the calculated value of α and the width of the periodic box l^1 , the error of the reciprocal-space sum is estimated according to:

$$\text{error} = \frac{k_{\max} \sqrt{l} \alpha}{20} \exp\left(-(\pi k_{\max}/l \alpha)^2\right). \quad (3.8)$$

The value of the cutoff in reciprocal space k_{\max} is chosen such, that $\text{error} < \delta$ according to eq. 3.8 [143].

The fitting is performed using the simplex algorithm *fminsearch* [144], implemented in Matlab[®] [145], as a minimization of the sum of squared errors (SSE); error is the difference in bulk energy values calculated with DFT and with MM for each point of the EOS. Since no force field parameters are involved in the electrostatic contribution, it is evaluated once for each of the points $\{V\}$ and then added to the short-range contribution. Having calculated the DFT energies $E_{\text{bulk}}^{\text{DFT}}\{V\}$ and the electrostatic contribution $E_{\text{bulk}}^{\text{Ewald}}\{V\}$, the fitting is performed in the following steps (schematically shown in fig. 3.3):

1. Guess of the parameters. In addition to the parameters entering the pair potentials, dummy parameter C is used to shift the MM value to the energy range of the DFT, and does not appear in the final force field.
2. Calculation of the short-range contribution in the bulk, $E_{\text{bulk}}^{\text{Buck}}$, with Buckingham pair potentials.
3. Addition of the electrostatic contribution to calculate the total bulk energy, $E_{\text{bulk}}^{\text{MM}}$, with molecular mechanics.
4. Shift of the classical energy to match the range of DFT.
5. Calculation of the SSE. Optionally, the errors are weighted with factors $w\{V\}$ prior to calculating the SSE to achieve a better fit around the minimum.

The fitted parameters are used in a Coulomb-Buckingham force field, the pair potentials of which have the form:

$$E_{ij}^{\text{Coul-Buck}} = \frac{e^2 z_i z_j}{r_{ij}} + b_i b_j \exp\left(\frac{-r_{ij}}{\rho}\right) - \frac{d_i d_j}{r_{ij}^6}. \quad (3.9)$$

These are employed for the calculation of the energy of MgF_2 clusters in non-periodic systems. The total energy of the clusters is calculated as a sum of pair interactions:

$$E_{\text{cluster}}^{\text{MM}} = \sum_{\substack{i,j \\ i \neq j}} E_{ij}^{\text{Coul-Buck}}. \quad (3.10)$$

¹In non-cubic boxes, the shortest dimension is taken as l .

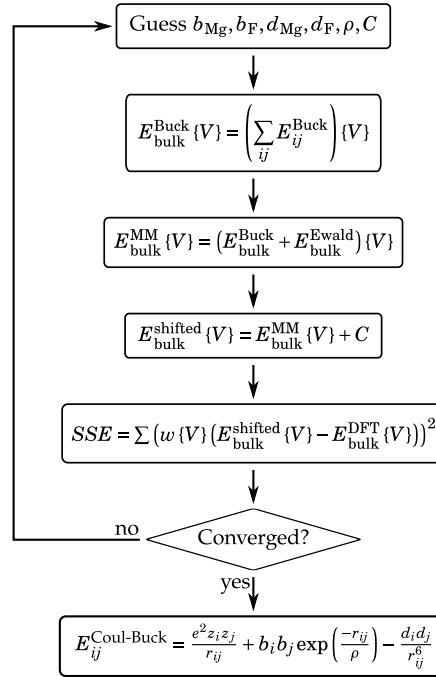


Figure 3.3: The strategy followed for the parametrization of classical pair potentials, for the development of a force field that reproduces the DFT energies for bulk MgF_2 .

4 Results

On the way to a predictive model for the sol-gel synthesized MgF_2 , the present work is concerned with two central topics. One topic is the influence of the synthetic conditions on the morphology of crystals. The most important results on this subject have been published in paper **P2**. The other topic relates to the catalytic properties of MgF_2 surfaces and their investigation with quantum chemical methods. This is the subject of paper **P1**, in which Hartree-Fock, MP2 and DFT with dispersion correction schemes have been employed to describe the adsorption of HF and H_2O on various MgF_2 surfaces. The publications are attached in the next chapter.

In this chapter, complementary questions are addressed, either to – challenge and – support the validity of the already published results, or to extend the investigation to related questions. The chapter begins with basic considerations concerning the calculation of surface energy, in section 4.1, which underlie the investigation presented in papers **P1** and **P2**. The effect of finite basis and the performance of different methods on the calculation of surface energies is tested in the example of pure, low-index MgF_2 surfaces. Then, the focus is moved to hydroxylated terminations and their stability, as predicted from Hartree-Fock, MP2 and DFT calculations. Papers **P1** and **P2** focus on these low-index terminations and the adsorption of H_2O and HF on them. Vicinal surfaces are the subject in section 4.2. Defects are assumed to play an essential role in the properties of nanostructured material. To model defective sites within the periodic model, slabs are cut at a small angle to the lattice vectors. The stability of the resulting terminations, some of which are highly unsaturated, is discussed briefly. Subsequently in section 4.3, one of the vicinal surfaces, (103), is taken as a model for defects. Hydroxylation and its effect on the adsorption of H_2O and HF on surface (103) is studied with DFT. Phase diagrams are then created for the prediction of the stability of the modelled terminations at finite temperature and pressure. These two sections are based on calculations performed by two students during their research internships under the author’s supervision: Mengxi Shi carried out the DFT calculations presented in section 4.2, and Bruno Pescara did the DFT calculations involving hydroxylated terminations of (103).

The work presented in section 4.4 was motivated by the insights won in papers **P1** and **P2**. It is seen in **P1**, that DFT is not always sufficient for the description of the adsorption structures, some of which occur in the Wulff plots of **P2**. So the question arises, whether the crystal morphologies predicted from thermodynamics based on DFT are valid. To answer this, MP2 calculations are combined with surface thermodynamics to create surface diagrams and consequently Wulff plots for MgF_2 . The MP2 calculations were performed by Giuseppe Sansone under supervision of Lukas

Hammerschmidt and Lorenzo Maschio. In the last section, the focus is shifted from quantum chemistry towards multiscale modelling. To open the way for a mesoscale model of MgF_2 that is compatible with the quantum chemical results, a classical force field is parametrized to reproduce the results of DFT calculations.

4.1 The contribution of electron correlation to the stability of low-index surfaces

The truncation of the bulk when modelling surfaces goes along with a basis set superposition error (BSSE) as a result of the use of finite basis sets: Compared to the bulk, the basis is unbalanced in the surrounding of the surface atoms due to the removal of the neighbouring atomic layers and the corresponding basis functions. This disturbance is usually not accounted for in the calculation of surface energies. It occurs in more or less similar extent for all slabs, therefore it is not expected to interfere with the relative stability of the surfaces.

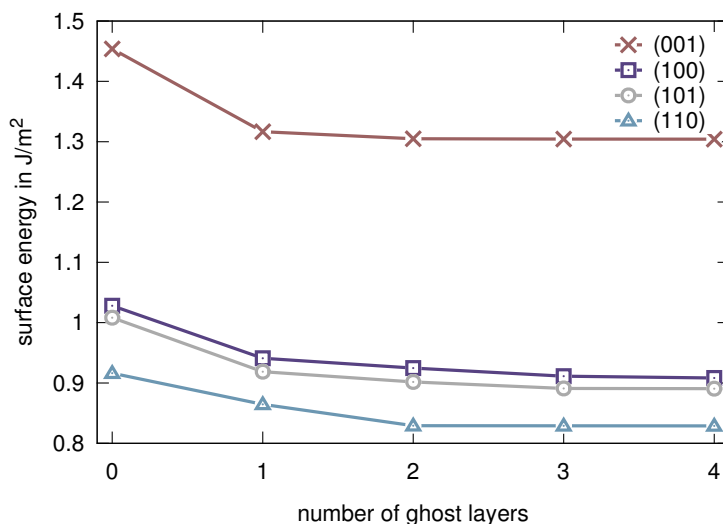


Figure 4.1: The effect of truncation on the surface energy of unrelaxed slabs. The addition of atomic ghost layers results in stabilization of the surfaces without changing their energetic order.

Focusing on the four low-index surfaces of MgF_2 , the effect of truncation on the surface energy of unrelaxed¹ structures has been examined. This was done by placing increasing layers of ghost atoms in the position of the missing neighbours on the slabs. The surface energies obtained for these slabs with B3LYP are shown in fig. 4.1. Being the only low-index surface to expose fourfold coordinated cations, (001) shows, with

¹That refers to the relaxation of the slab structures. The slabs themselves are derived from the fully optimized bulk, like all other structures in this work.

0.15 J/m², the strongest decrease in the surface energy after addition of ghost atoms. Surface (100) is stabilized by 0.12 J/m², (101) by 0.11 J/m² and (110) by 0.09 J/m². Convergence is reached in (001) already after addition of the first layer of ghost atoms, owing to the fact that one atomic layer covers all positions of missing neighbours of the surface atoms. Analogously, convergence is reached after addition of three atomic layers on (100) and (101), while the surface energy of (110) converges when two atomic layers are added.

The energetic order of the surfaces is associated to their stabilization after addition of ghost layers, with the least stable surfaces “gaining” from the ghost layers the most. Yet, the BSSE has no consequence on the energetic order of the surfaces. That being the case, truncation-related BSSE is not taken into account in the further investigation of surfaces.

After optimization of the structures on the other hand, the energetic order of the surfaces changes. The relaxation energy of (101) is significantly lower compared to the other three surfaces, only 8% of the unrelaxed surface energy, whereas it is 18% for (001), 16% for (100) and 19% for (110).

Table 4.1: Surface energy in J/m² for the four low-index terminations of rutile MgF₂ obtained from DFT, MP2 and Hartree-Fock calculations on the structures optimized with DFT, and exposure of the surfaces in the Wulff plot.

	DFT ²		MP2		Hartree-Fock	
	E_{surf}	area	E_{surf}	area	E_{surf}	area
(001)	1.07	–	1.15	–	1.10	–
(100)	0.76	16%	0.87	14%	0.80	16%
(101)	0.82	43%	0.90	45%	0.85	44%
(110)	0.67	41%	0.76	41%	0.71	40%

The surface energies obtained from DFT, Hartree-Fock and MP2 calculations on the structures relaxed with B3LYP are presented in table 4.1. The three methods predict the same energetic order for the surfaces: Among relaxed structures, (110) is the most stable termination, followed by (100), (101) and (001). Also quantitatively the methods are in very good agreement, with differences in the energy of the same surface being less than 6%. The performance of Hartree-Fock is in the case of pure surfaces comparable to DFT and MP2, in line with the findings of the thorough analysis by Hammerschmidt *et al.* [46] on the correlation contributions in MgF₂ (110) slabs. Also in line with this analysis, the surface energies calculated with MP2 are higher than those calculated with B3LYP.

It cannot be said with certainty which method yields the “correct” surface energies, since there are no experimental values available. However, as Hammerschmidt *et al.*

²The surface energies calculated with DFT are identical to those published in [28]. However, the exposure of the surfaces differs, presumably due to an oversight related to the Wulff construction in [28].

note, there is an intrinsic source of error in local MP2 calculations of surface energies according to eq. 2.99: By analogy to the effect of the truncated basis discussed previously, the neighbours removed when cutting a surface from the bulk interfere in local MP2 with the consistent description of the excitation domains between bulk and slabs. The excitation domains in the MgF_2 bulk include one F and its 3 neighbouring Mg (see also **P1**). Since the surface fluorines (fig. 4.2) have only two neighbours, the excitation domains of the surface atoms are smaller than the corresponding in the bulk. In [46], this effect was found to be in a similar range as the BSSE in the unrelaxed (110).

The effects discussed above have a similar influence on all low-index surfaces. When used in Wulff constructions, the three series of surface energies give essentially the same crystal shape. The exposure of the surfaces in the Wulff plots, listed in table 4.1 next to the corresponding surface energies, is nearly identical in the three cases, with deviations not exceeding 2% of the total crystal surface. Surfaces (101) and (110) dominate the surface of the crystal, each with more than 40% participation, while (100) takes up 14-16% depending on the method. Based on the Wulff construction, (001) appears not to be exposed in the athermal limit.

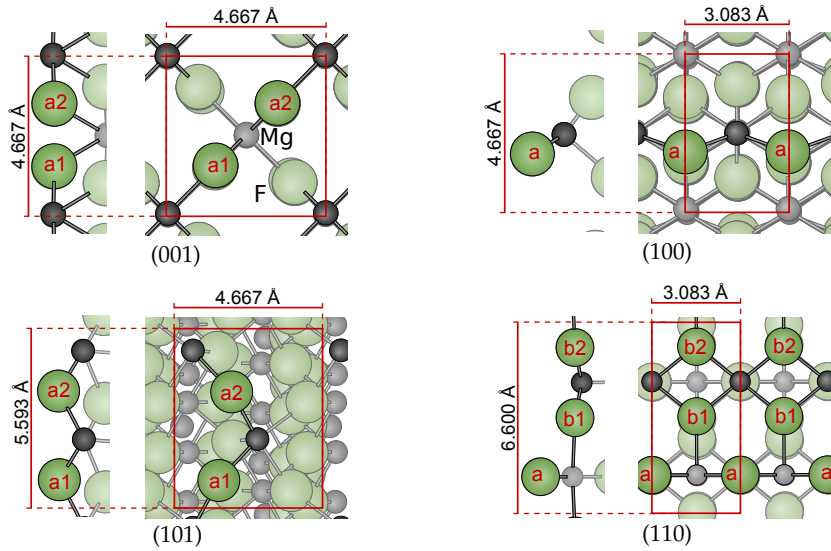


Figure 4.2: Relaxed surfaces of rutile MgF_2 in side and top view. Surface atoms are highlighted and non-equivalent surface fluorines marked with (a) and (b). Red frames mark the periodic unit (1×1 cell).

Turning to partially hydroxylated surfaces, one faces the problem that a surface energy as defined in eq. 2.99 cannot be calculated for slabs with modified surface composition, because there is no analogy to a homogeneous bulk. Instead, their stability can be evaluated by defining an energy of hydroxylation ΔE_{OH} , which is the reaction energy of:

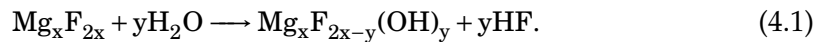


Table 4.2: Energy of hydroxylation, in eV, obtained from total energies according to eq. 4.2. y is equal to 2 for all cases and 4 for (101)-2OH_a.

pattern	cell	ΔE_{OH}		
		DFT	MP2	Hartree-Fock
(001)-1OH _a	1×1	0.508	0.594	0.700
	$\sqrt{2} \times \sqrt{2}$	0.510	–	–
(100)-1OH _a	1×1	0.476	0.570	0.629
	2×1	0.422	–	–
(101)-1OH _a	1×1	0.582	0.676	0.773
(101)-2OH _a	1×1	0.572	–	–
(110)-1OH _a	1×1	0.608	0.703	0.785
	2×1	0.545	–	–
(110)-1OH _b	1×1	0.475	0.534	0.649
	2×1	0.440	–	–

This allows for the comparison of the energies, since the system in each side of 4.1 consists of x magnesium, $2x$ fluorine, $2y$ hydrogen, and y oxygen atoms. The hydroxylation energy per substituted site is then calculated as:

$$\Delta E_{\text{OH}} = \frac{1}{y} \left(E_{\text{Mg}_x\text{F}_{2x-y}(\text{OH})_y} + yE_{\text{HF}} - E_{\text{Mg}_x\text{F}_{2x}} - yE_{\text{H}_2\text{O}} \right). \quad (4.2)$$

The available positions for surface hydroxylation are shown in fig. 4.2. (001) and (101) have two equivalent fourfold coordinated surface fluorines in the unit cell, whereas (100) only one. On (110) there are two equivalent threefold coordinated fluorines, marked with (b), and one of twofold coordination, marked with (a). The hydroxylation energies have been calculated with DFT, and selected hydroxylation patterns additionally with Hartree-Fock and MP2; they are presented in table 4.2. The hydroxylation patterns are named (hkl)-nOH_m, with n the number of hydroxyls in the periodic unit, and the hydroxylation position $m = a, b$ or c . For example, pattern (001)-1OH_a on cell 1×1 is a termination of (001), in which all $a1$ positions are hydroxylated. The same pattern on cell $\sqrt{2} \times \sqrt{2}$ means that every other $a1$ position is hydroxylated, in total one forth of the surface anions. ΔE_{OH} is calculated from total energies of symmetric slabs, so $y = 2n$ for the two sides of the slab.

The hydroxylation of MgF₂ is in all cases predicted to be endothermic: ΔE_{OH} is positive for all patterns studied, regardless of the method employed for the calculation. ΔE_{OH} calculated from the DFT energies takes values between 0.440 and 0.582 eV per substituted site, depending on pattern and degree of hydroxylation. On surfaces (100) and (110), the hydroxylation energy is lower in 2×1 than in 1×1 cells, indicating a destabilizing interaction between hydroxyls in neighbouring cells. The largest difference is observed for (110)-1OH_a, where ΔE_{OH} for substitution of one fluorine per 2×1 cells is 63 meV lower than for the substitution of one fluorine per 1×1 cell. For (100), the difference between degrees of hydroxylation is lower, 54 meV. In both cases

the hydroxyls are coordinated to two cations. Due to the form of the unit cell they are positioned rather close to the equivalent position in the neighbouring cell, 3.08 Å. Obviously, latter is true for termination of (110)-1OH_b as well. Yet, the difference in hydroxylation between the 2 × 1 and 1 × 1 cell is in this case only 35 meV, as hydroxyls in position b are sterically prevented from interacting with those in the neighbouring cells. On surface (001) the difference between hydroxylation energies on 1 × 1 and $\sqrt{2} \times \sqrt{2}$ is, with 2 meV, negligible; the square (001) unit cell leaves already at high degree of hydroxylation a distance of 4.67 Å between hydroxyls in neighbouring cells, which is sufficient to prevent an interaction between them. On surface (101), the situation is different. Here, two degrees of hydroxylation are tested, both in the 1 × 1 cell: hydroxylation pattern (101)-2OH_a, where both positions a1 and a2 are hydroxylated, and (101)-1OH_a, where one of them is occupied by a fluorine. ΔE_{OH} is in this case by 10 meV higher at high than at low degree of hydroxylation. The stabilizing interaction between hydroxyls, which is observed only for this termination, is a result of the “staggered” structure of (101). When hydroxyls occupy both positions a1 and a2, they exhibit an alternating, chain-like arrangement, the consequence of which is a slight stabilization of the structure.

Comparing the hydroxylation energy for different surfaces at low degree of hydroxylation, (101) has the highest ΔE_{OH} , is thus the least favoured hydroxylation position. It is followed by (110)-1OH_a, (001) and (110)-1OH_b. Hydroxylation is most favoured on (100), with $\Delta E_{\text{OH}} = 476 \text{ meV}$. In any case, as indicated by the positive values of the hydroxylation energy, non-hydroxylated terminations are more stable than their hydroxylated counterparts.

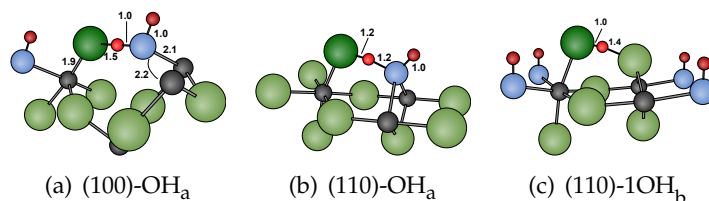


Figure 4.3: Adsorption structures of HF on partially hydroxylated MgF₂ surfaces, obtained from optimization with B3LYP. Selected distances and bond lengths are given in Å.

Structure optimizations on the adsorption of HF on hydroxylated MgF₂ surfaces support this finding. Starting from hydroxylated surfaces and placing a HF molecule on top of the coordinatively unsaturated Mg, the system tends towards re-fluorination, as it can be seen in the optimized structures in fig. 4.3. The F-end of HF coordinates to Mg, while the H-end forms a hydrogen bond to the hydroxy-group on the surface; on (110)-1OH_b the hydroxyl is not available due to its position with threefold coordination, so the H-bond acceptor is a surface fluorine. In all three cases, the F–Mg distance is, with 1.9 Å, in the range of the bonds in the slab (1.9–2.0 Å). The distance from the HF-hydrogen to the oxygen of the hydroxyl (or in the last case to the surface

fluorine) ranges between 1.0-1.4 Å; the distance between H and F of the adsorbate is in the range 1.0-1.5 Å. On the other hand, the bond lengths of the free molecules are 0.97 Å for H₂O and 0.93 Å for HF, and they do not change significantly during all other cases of adsorption on MgF₂ surfaces studied. Based on the bond lengths, the hydrogen can thus not be unambiguously attributed to HF or H₂O. The adsorption energy for these structures, -0.79 eV for 100% HF on hydroxylated (100), -1.23 eV for 100% HF on (110)-1OH_a and -0.97 eV on (110)-1OH_b, is notably higher than the adsorption energy on the corresponding non-hydroxylated surfaces, -0.67 eV and -0.89 eV respectively (see paper P1).

Returning to the energy of hydroxylation, the three methods show qualitative agreement regarding the endothermic nature of the reaction. For a quantitative comparison, one should keep in mind that ΔE_{OH} is some orders of magnitude smaller than the total energies, or even the MP2 corrections. If ΔE_{OH} is split in contributions from the adsorbates, $\Delta E_{\text{ads}} = 2 (E_{\text{HF}} - E_{\text{H}_2\text{O}})$, and from the slabs, $\Delta E_{\text{slab}} = E_{\text{Mg}_x\text{F}_{2x-y}(\text{OH})_y} - E_{\text{Mg}_x\text{F}_{2x}}$, the two parts have comparable contributions to ΔE_{OH} , -48.02 and approx. 48.07 Ha, respectively. That is not the case in the MP2 corrections. The correction to ΔE_{ads} is -0.012 Ha, coming from the difference in correlation between the adsorbates, is the principal contribution to the correction of the hydroxylation energy. It is partly compensated by the positive correction to ΔE_{slab} , which ranges between 0.004 - 0.008 Ha. The correction to ΔE_{slab} decreases with increasing stabilization the hydroxylated slab. As a consequence, the overall correction to ΔE_{OH} increases. The highest and lowest correction in ΔE_{slab} are observed for structures (100)-1OH_a and (110)-1OH_b respectively. As the hydroxylation energies from Hartree-Fock are very close for the two structures, MP2 causes a reversing in the energetic order, "correcting" the discrepancy between Hartree-Fock and DFT.

4.2 Truncation and stability of vicinal surfaces

The interest in surface properties is usually limited to the most stable surfaces, which are in most cases the low-index ones. Part of the focus of this work being the shape of nanocrystals, high-index terminations are also taken into account and tested for their potential exposure in the crystallites.

Cutting at a small angle to the lattice vectors, the slabs created are of Type B according to Tasker's nomenclature [146]: They consist of sequences F-Mg-F-F-Mg-F of charged atomic layers, allowing for symmetric stoichiometric slabs with no net dipole moment normal to the surface. The periodicity patterns relevant for the high-index slabs are shown schematically in fig. 4.4. Each block layer corresponds to the least number of atomic layers that need to be added on a symmetric and stoichiometric slab to produce another symmetric and stoichiometric slab. In the case shown in fig. 4.4(a), addition of a block layer results in a shift of the surfaces with respect to another by a fraction of the lattice constant (1/4 in the example shown). The exposed surfaces on the two sides are equivalent irrespectively of the thickness, provided it is a multiple of block layers. However, the relative position of the surface sites, consequently

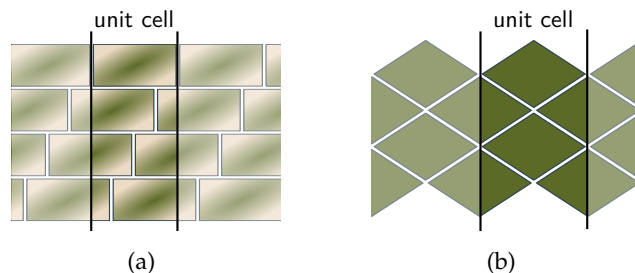


Figure 4.4: Pictorial representation of periodicity and symmetry patterns in vicinal slabs. A layer of blocks represents the number of layers required to preserve stoichiometry in the slab.

the orientation of the partial dipole moments, change with every added block layer affecting the surface energy. As it takes a few layers for the relative position of the surfaces to be repeated, an increase in the thickness of slabs with periodicity (a) is unlikely to produce a recognizable pattern as the surface energy converges. The pattern shown in fig. 4.4(b) is more familiar. A slab of odd number of block layers has a mirror plane symmetry resulting in a peak-peak profile. A slab of even number of block layers has a glide plane symmetry giving a peak-well profile. Assuming, for example, that coordinatively unsaturated cations sit in the wells of the surface in fig. 4.4(b), they will be positioned directly opposite to each other in a slab with odd number of block layers; in a slab of even number of block layers the cations of the opposite surfaces will be alternating. Increasing the thickness of such a slab will result in a kind of odd-even effect.

A block layer in slabs (102), (112), (103) and (301) has a thickness of 3 atomic layers, whereas in (120), (201) and (401) a thickness of 6 atomic layers. Some of the modelled high-index slabs combine both types of layering in the two directions parallel to the surface, resulting in the convergence patterns shown in fig. 4.5. For example, in slab (102) two series of odd-even oscillations in the two lattice directions parallel to the surface, resulting from the combination of two patterns of type (b) can be clearly recognized. On the other hand, type (a) dominates in slab (401), leading to a particularly favourable interaction for a thickness of 39 atomic layers and an unfavourable one for 51 atomic layers, but loses in significance as the slab thickness increases, leading to convergence.

The energy of the high-index surfaces is calculated from the relaxed structures at converged thickness. The surface energies for all studied terminations are listed in table 4.3. They are significantly higher than the energies of the low-index surfaces (table 4.1), with the exception of (001), so they do not appear in the Wulff construction.

Nevertheless, surface (103) has been included in the study: On one hand, its surface energy as calculated with B3LYP is so close to the energy of (001), that an exposure of (103) is possible under conditions of finite pressure and temperature. On the other hand, it is a suitable model for stepped surfaces.

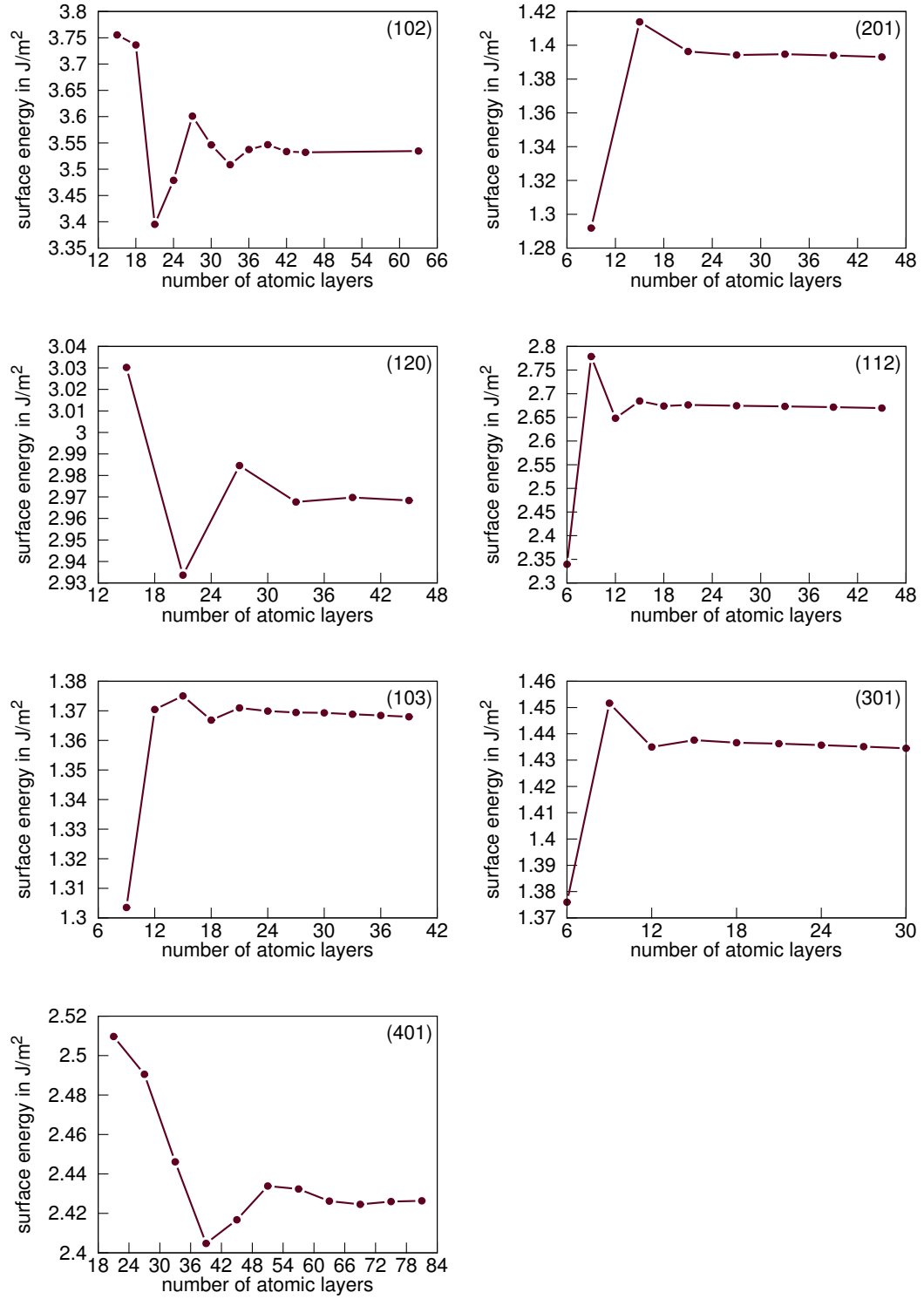


Figure 4.5: Convergence of the surface energy with slab thickness for vicinal cuts. The results are obtained from DFT calculations on unrelaxed structures.

Table 4.3: Energy, in J/m^2 , of vicinal surfaces, obtained from optimization with DFT. The thickness of the slabs in atomic layers is also listed.

(hkl)	atomic layers	E_{surf}
(102)	45	1.57
(201)	33	0.93
(120)	39	1.54
(112)	21	2.01
(103)	36	1.02
(301)	24	0.92
(401)	69	0.91

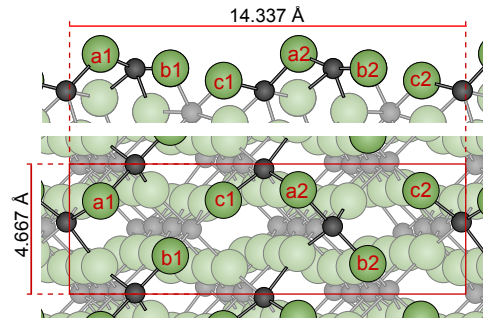


Figure 4.6: Relaxed structure of surface (103). Surface atoms are highlighted and non-equivalent surface fluorines marked with (a), (b) and (c). Red frames mark the periodic unit (or 1×1 cell).

4.3 Surface (103)

4.3.1 Terminations and adsorption

Surface (103), shown in fig. 4.6, exposes three non-equivalent surface anions and two coordinatively unsaturated cations. The anions, all doubly coordinated, are marked in fig. 4.2 with (a), (b) and (c). Due to the vicinal cut of the surface, their positions differ slightly in height, with (a) lying higher than (b), which lies in turn higher than (c). Fourfold coordinated Mg cations are coordinated to anions (a) and (b), whereas fivefold coordinated Mg cations are located between anions (a) and (c).

Table 4.4: Energy of hydroxylation for surface (103), in eV, obtained from DFT calculations.

termination	cell	ΔE_{OH}
(103)- 1OH_a	1×1	0.480
(103)- 1OH_b	1×1	0.497
(103)- 1OH_c	1×1	0.555

Hydroxylation is probed on the surface sites of (103) by exchanging one of the fluorines for a hydroxyl and optimizing the structure. As in the case of low-index surfaces discussed previously, the obtained values for ΔE_{OH} (see table 4.4) are positive, which means that the hydroxylation of eq. 4.1 is endothermic. Position (a) has the lowest hydroxylation energy, followed by (b) and (c), showing a correlation to the position of the anion in the z-axis: the more exposed the surface anion, the less unfavoured its hydroxylation.

The adsorption of HF and H₂O on (103) is calculated on clean and partially hydroxylated surfaces. Structures at half coverage are studied, such that one kind of adsorption sites – four- or fivefold coordinated Mg – is occupied by adsorbates. Regarding hydroxylated surfaces, only structures have been investigated on which the adsorbate coordinates to a site next to a hydroxyl: There are two possible structures for (103)-OH_a, where the hydroxyl is located between the two surface cations, and one for (103)-OH_b and (103)-OH_c, each. On (103)-OH_c, however, no minimum is found for the adsorption of HF.

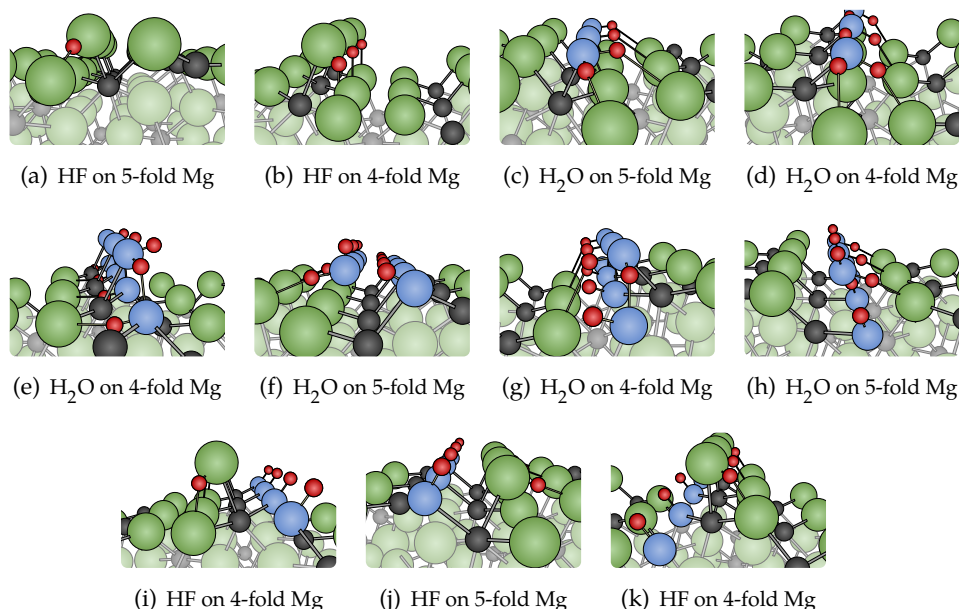


Figure 4.7: Adsorption structures of HF and H₂O on terminations of (103). (a)–(d) clean surfaces, (e)–(f) and (i)–(j) (103)-OH_a, (g) and (k) (103)-OH_b, and (h) (103)-OH_c. Green spheres represent fluorine, black magnesium, red oxygen and blue hydrogen atoms.

The optimized adsorption structures are presented in fig 4.7. After geometry optimization, the molecules are arranged on the surface so that the electronegative end (oxygen or fluorine) coordinates to the surface Mg, while the hydrogen coordinates to a surface fluorine. The distance between electronegative end and Mg varies between 2.0 and 2.2 Å in the different structures.

The adsorption energies, listed in table 4.5, are in the same range as for the low-index

surfaces, with H_2O showing generally stronger adsorption than HF. Furthermore, H_2O is adsorbed stronger on the fourfold coordinated site, where it forms two H-bonds to the neighbouring fluorines. In contrast, HF binds stronger to the fivefold coordinated site. There, it takes the position of the missing neighbour and forms a significantly shorter H-bond of 1.6 Å – compared to a distance of 2.1 Å in the case of the fourfold site.

The presence of hydroxyl on (103) destabilizes, in the majority of cases, the adsorption of molecules on the neighbouring cations. Hydroxylation in position (a) has no effect on the adsorption of HF on the fourfold coordinated Mg and only a minor one of 3% decrease in the adsorption energy on the fivefold coordinated Mg. Hydroxylation of position (b) leads to a 13% decrease in the adsorption energy of HF compared to the clean surface. When a hydroxyl is introduced in position (c) adsorption of HF on the fivefold coordinated site fails completely. In contrast to the low-index surfaces, no tendency for re-fluorination of the hydroxylated site is observed on (103). The reason is presumably the protected position of the hydroxy groups in the slab, that prevents them from acting as H-bond acceptors.

Table 4.5: Adsorption energies, in eV, for H_2O and HF on surface (103). All values refer to 50% coverage. Adsorption of HF does not occur on the fivefold coordinated cationic site of (103)- OH_c .

termination	site	E_{ads}	
		H_2O	HF
(103)	4-fold	-1.09	-0.63
(103)	5-fold	-0.80	-0.79
(103)- OH_a	4-fold	-0.71	-0.61
(103)- OH_a	5-fold	-0.67	-0.80
(103)- OH_b	4-fold	-0.90	-0.55
(103)- OH_c	5-fold	-0.56	–

The interaction of H_2O with surface (103) is also hindered by surface hydroxyls. Hydroxylation of position (a) significantly affects the adsorption on the fourfold site, which is 35% weaker than on the clean surface; to a lesser extent it affects the adsorption on the fivefold site, which is 17% weaker than on the clean surface. Adsorption on the fivefold site is affected more by hydroxyls in position (c), which lead to a 30% decrease of the adsorption energy compared to the clean surface. When position (b) is occupied by a hydroxyl, H_2O adsorbs 17% weaker on the fourfold cation than on the clean surface.

The adsorption energies for H_2O presented above, in particular those concerning hydroxylated terminations, should be interpreted with caution. As discussed in paper **P1**, DFT does not adequately describe interactions in which dispersion is of importance. In this regard, the structures shown in figures 4.7(f) and 4.7(h) are particularly problematic. The O–Mg distance is in both cases, with 2.2 Å, rather long, and com-

parable – or longer – to the distance of the oxygen to the hydrogen on the surface: 2.2 Å on (103)-OH_a and 2.0 Å on (103)-OH_c. According to the findings in **P1**, DFT is not expected to describe the adsorption interactions in these structures satisfactorily, but it cannot be predicted with certainty if the adsorption energy is under- or overestimated.

4.3.2 Surface thermodynamics

Having optimized structures for the clean and hydroxylated terminations of (103), as well as the adsorption on them, the total energies of the structures are used in phase diagrams for three temperatures (fig. 4.8), following the choice of conditions in paper **P2**. They include, besides the clean surface, hydroxylation patterns in which one or two equivalent anion positions are hydroxylated, and adsorption structures of H₂O and HF at half coverage, on clean and doubly hydroxylated surfaces. Full coverage, in which four- and fivefold cations are covered with adsorbates, is not possible on surface (103) due to the high density of adsorption sites.

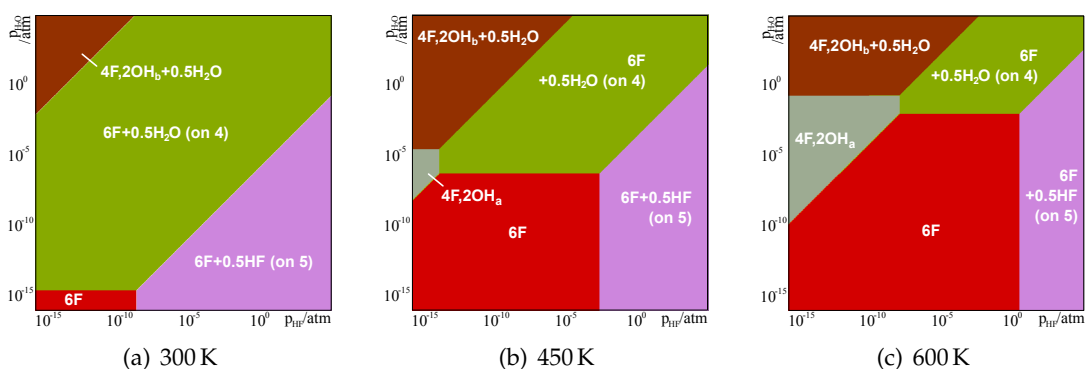


Figure 4.8: Phase diagrams for surface (103) at three temperature values and varying partial pressure of H₂O and HF, based on DFT energies. The terminations are named after the anions on the surface, the adsorbates and the coordination of the adsorption site: e.g. 6F for clean MgF₂ surface, 4F,2OH_b+0.5H₂O for a termination hydroxylated in position (b) and half-covered with H₂O.

At low partial pressures, clean (103) is the most stable termination. The water-covered surface becomes more stable as the partial pressure of water rises. At 300 K, that happens already at $p_{\text{H}_2\text{O}} = 10^{-15}$ atm, whereas at 450 and 600 K the transition occurs later, at pressures of 10^{-7} and 10^{-3} atm respectively. By analogy, increasing partial pressure of HF favours the HF-covered termination at 300 K already when 10^{-9} atm are reached. At 450 K the clean termination is more stable up to $p_{\text{HF}} = 10^{-3}$ atm and at 600 K a partial pressure of 1 atm is required for HF adsorption to take place. Turning towards the high pressure region, where the transition from H₂O- to HF-covered termination occurs, it should be pointed out that H₂O preferably adsorbs on fourfold,

whereas HF on fivefold sites. That being the case, the two adsorbates do not compete for the same adsorption sites, but still sterically hinder each other. At increased temperature, high partial pressure of H_2O and low partial pressure of HF the most stable doubly hydroxylated surface is exposed, (103)- OH_a . A further increase of $p_{\text{H}_2\text{O}}$ leads to the adsorption of H_2O on the hydroxylated surfaces. The interaction with H_2O molecules particularly stabilizes termination (103)- OH_b . As a consequence, H_2O -covered (103)- OH_b is exposed at high $p_{\text{H}_2\text{O}}$. This is an illustrative example on how the experimental conditions can be used for fine tuning of the surface and manipulation of the catalytic activity.

4.4 Surface thermodynamics based on MP2 energies

4.4.1 Phase diagrams and crystal morphology

The relative stability of a variety of terminations and the morphology of MgF_2 crystals at conditions of finite temperature and pressure was investigated in paper **P2** by combining surface thermodynamics with DFT calculations. On the other hand, the comparison of methods for the description of adsorption interactions in paper **P1** showed that the adsorption of H_2O , in particular on hydroxylated surfaces, is not described sufficiently with DFT. In this section, the phase diagrams are reviewed to examine how significant is the effect of explicit correlation in the quantum chemical calculations for the prediction of the crystal morphology: MP2 calculations are combined with surface thermodynamics for the creation of phase diagrams and consequently Wulff constructions for the prediction of crystal shapes.

At 300 K adsorption structures dominate the phase diagrams, shown in fig. 4.9. Clean terminations, shown in red, are exposed only at very low pressures. As long as the partial pressure of H_2O is kept low, surfaces covered with HF become more stable as p_{HF} increases. This happens for $p_{\text{HF}} = 10^{-13} - 10^{-12}$ atm on (100), (101) and (110), but not before 10^{-9} atm have been exceeded on (001). Surfaces covered with H_2O are favoured compared to clean terminations already at $p_{\text{H}_2\text{O}} = 10^{-14} - 10^{-13}$ atm for (001), (101) and (110) at low partial pressure of HF and around $p_{\text{H}_2\text{O}} = 10^{-11}$ atm for (100). The two adsorbates compete when both partial pressures are increased, but as long as the pressures are held equal the adsorption of H_2O is strongly favoured on (001), and slightly on (110). On (001), (100) and (110), H_2O -covered hydroxylated surfaces are the most stable terminations when the partial pressure of H_2O is high and at the same time the partial pressure of HF very low.

With an increase of temperature to 450 K, clean surfaces gain in importance (fig. 4.10). Clean terminations of (100), (101) and (110) are the most stable up to partial pressures of 10^{-5} atm, with a minor deviation for (001), on which the clean termination is favoured up to $p_{\text{HF}} = 10^{-3}$ atm and $p_{\text{H}_2\text{O}} = 10^{-6}$ atm. On all surfaces, HF-covered terminations dominate at high p_{HF} . The transition from HF- to H_2O -covered terminations in the high pressure region occurs at $p_{\text{HF}} = p_{\text{H}_2\text{O}}$. In the region of low p_{HF} and towards high $p_{\text{H}_2\text{O}}$, hydroxylated terminations occur, giving their place to H_2O -

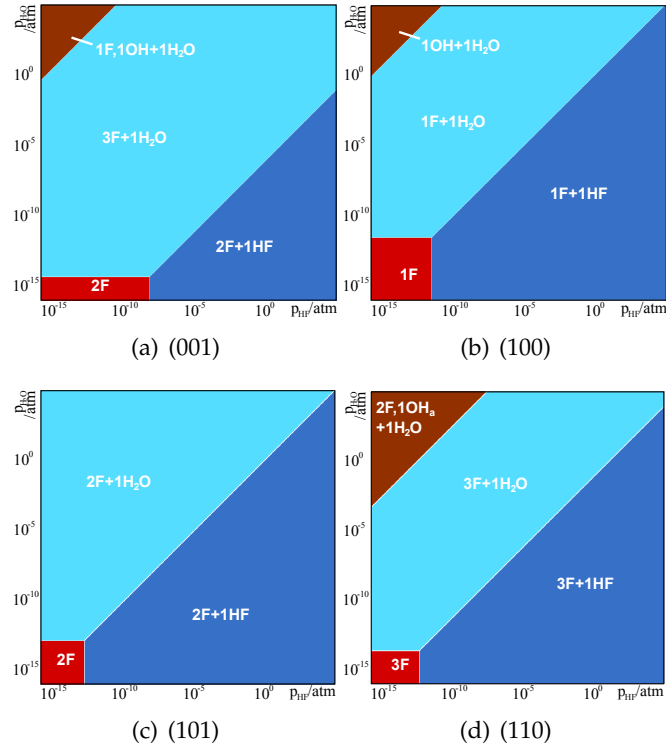


Figure 4.9: Phase diagrams for the four low-index surfaces of rutile MgF_2 at 300 K, based on MP2 energies.

covered hydroxylated terminations with increasing partial pressure of H_2O .

The trends described above evolve further when the temperature is increased to 600 K. A large part of the phase diagrams is occupied by clean terminations. These are exposed up to partial pressures of $10^{-3} - 10^{-2}$ atm for HF and H_2O – for (001) even up to $p_{\text{HF}} = 1$ atm. Hydroxylated terminations occupy a larger part of the low p_{HF} region compared to lower temperatures. As the partial pressure of H_2O increases, they give place to terminations which are additionally covered with H_2O .

The results obtained with surface thermodynamics are used to predict the shape of MgF_2 crystals at conditions of finite temperature and pressure of HF and H_2O . Wulff constructions for nine sets of conditions³ are presented in fig. 4.12. From left to right, the effect of increasing temperature can be observed at constant pressure conditions; from top to bottom, the transition from the low pressures region to the high $p_{\text{H}_2\text{O}}$ – low p_{HF} and then to the high pressures region. The values for the surface energy at the chosen conditions are listed in table 4.6, next to the corresponding terminations. In addition, the exposure of each termination in the Wulff construction is given as percentage of the total crystal area. As discussed in section 2.3, the thermodynamic considerations behind the Wulff construction imply that the surface with the lowest

³The conditions chosen are the same as those in paper P2, to facilitate a direct comparison of the results.

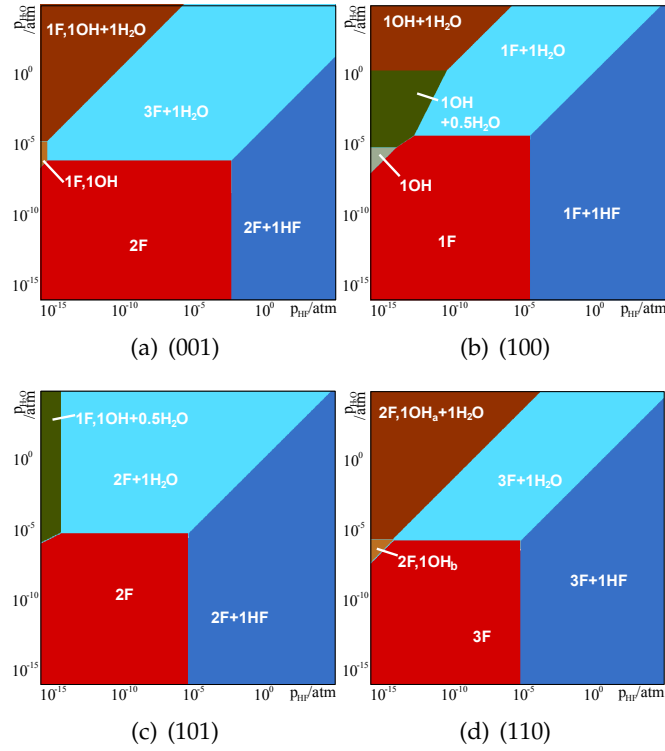


Figure 4.10: Phase diagrams for the four low-index surfaces of rutile MgF_2 at 450 K, based on MP2 energies.

energy occupies the largest part of the crystal surface, since it has the slowest growth rate. Although that is true, the values in table 4.6 show no exact – inverse – analogy between γ and the area. The reason is the symmetry of the MgF_2 , owing to which certain facets are equivalent; (101) occurs thus eight times, (110) and (100) four times, as explained in detail in paper P2.

The occurrence of terminations in the Wulff plots of fig. 4.12 reflects the observations made previously based on the phase diagrams: With increasing temperature and decreasing pressure, surfaces covered with adsorbates give place to clean surfaces; the composition of the exposed adsorbate-free terminations also depend on the temperature and pressure conditions. In particular, in the conditions chosen here, at low pressures (first row in the figure and table), clean surfaces are exposed at 600 and 450 K. Under the same pressure conditions at 300 K, H_2O covers all surfaces. The adsorption stabilizes (101) and (110) compared to (100), so the latter now only occupies 4% of the crystal surface. Keeping the temperature at 300 K, an increase in $p_{\text{H}_2\text{O}}$ to 10^{-3} atm particularly favours surface (101). As a consequence, platelet crystals are formed, the surface of which is dominated, with 84%, by (101). At the same conditions of pressure at 450 K, (110) is exposed in its hydroxylated and H_2O -covered termination. Combined to the observed increase in the surface energy of (101), this leads to the formation of cube-like crystals. A further increase of the temperature to

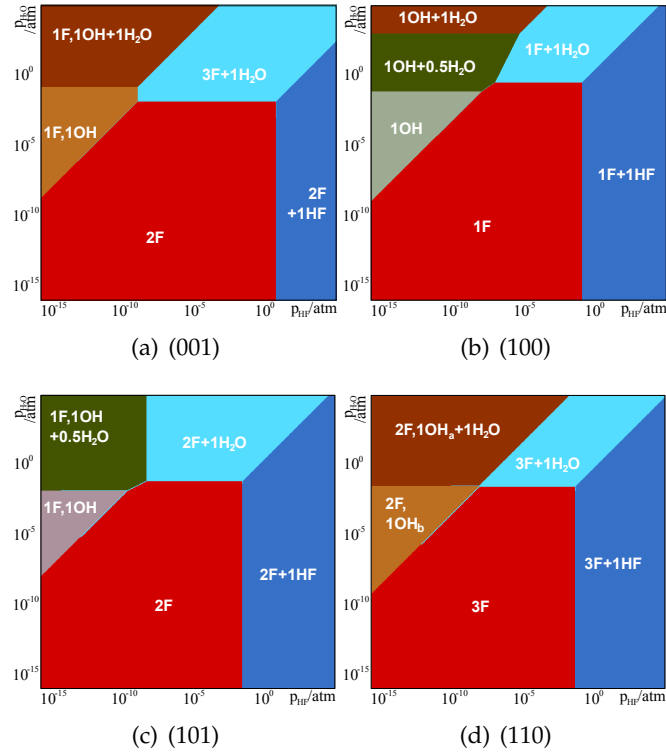


Figure 4.11: Phase diagrams for the four low-index surfaces of rutile MgF_2 at 600 K, based on MP2 energies.

600 K results in oblong crystals with hydroxylated surface; they consist only to 35% of the otherwise dominating (101), 46% (110) and 19% (100). An increase of p_{HF} favours, as expected, crystals the surface of which is covered with HF. At 600 K the crystals are quasi-spherical, but with a lowering of the temperature to 450 K they become flat, since the energy of (101) – having two adsorption sites per unit cell instead of one – decreases faster than the energy of the other surfaces.

An attempt to obtain surface energy values at 300 K, $p_{\text{H}_2\text{O}} = 10^{-3}$ atm and $p_{\text{HF}} = 1$ atm reveals the limitations of the model: A negative surface energy is obtained for (101) in the HF-covered termination. Strictly interpreted, a negative value for the surface energy suggests a decomposition of the slab in favour of the surfaces. Negative surface energies in surface thermodynamics can be interpreted as a limit for dissolution [147]. However, in the framework of this model, it should be regarded as an artefact caused by the high values for pressure. For a structure that consists of an MgF_2 slab and HF adsorbates, eq. 3.5 for the surface energy is reduced to:

$$\gamma(T, p_{\text{HF}}) = \frac{1}{2A} \left[E_{\text{slab}}^{\text{MP2}} - N_{\text{Mg}} E_{\text{MgF}_2\text{-bulk}}^{\text{MP2}} - N_{\text{HF}} \mu_{\text{HF}}(T, p_{\text{HF}}) \right], \quad (4.3)$$

so a negative value for γ is reached when $E_{\text{slab}}^{\text{MP2}} - N_{\text{Mg}} E_{\text{MgF}_2\text{-bulk}}^{\text{MP2}} < N_{\text{HF}} \mu_{\text{HF}}(T, p_{\text{HF}})$. Nonetheless, the qualitative observation is still valid: At conditions of high p_{HF} and high temperature, (101) is significantly more stable than the other surfaces.

4 Results

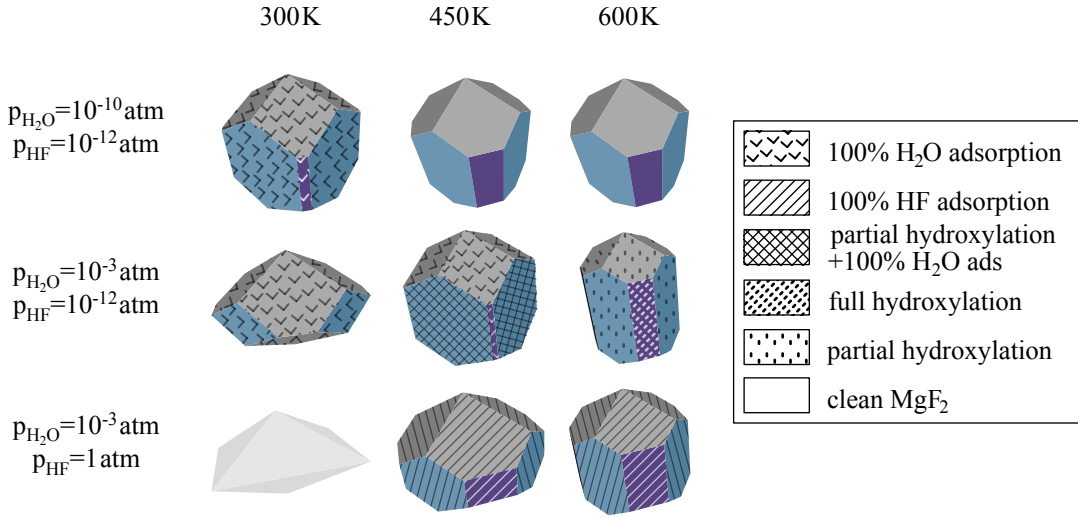


Figure 4.12: The effect of temperature change on the morphology of the crystals at three pressure conditions - surface (100) in purple, (101) in gray and (110) in light blue. The corresponding surface energies as well as the relative exposure of the surfaces on the crystal are presented in table 4.6. The Wulff construction for 300 K, $p_{\text{H}_2\text{O}} = 10^{-3}$ atm and $p_{\text{HF}} = 1$ atm is not possible. A more detailed explanation is given in the text.

Table 4.6: Exposed surfaces of MgF_2 crystals shown in fig. 4.12 – termination, surface energy in J/m^2 and abundance as percentage of the total crystal surface.

	300 K			450 K			600 K		
(hkl)	termin.	γ	area	termin.	γ	area	termin.	γ	area
	$p_{\text{H}_2\text{O}} = 10^{-10}$ atm/ $p_{\text{HF}} = 10^{-12}$ atm								
001	2F+1H ₂ O	0.96	–	2F	1.15	–	2F	1.15	–
100	1F+1H ₂ O	0.77	4	1F	0.87	14	1F	0.87	14
101	2F+1H ₂ O	0.69	45	2F	0.90	45	2F	0.90	45
110	3F+1H ₂ O	0.58	51	3F	0.76	41	3F	0.76	41
	$p_{\text{H}_2\text{O}} = 10^{-3}$ atm/ $p_{\text{HF}} = 10^{-12}$ atm								
001	2F+1H ₂ O	0.66	–	2F+1H ₂ O	0.95	–	1F,1OH	1.00	–
100	1F+1H ₂ O	0.31	–	1F+1H ₂ O	0.75	2	1OH	0.61	19
101	2F+1H ₂ O	0.17	84	2F+1H ₂ O	0.66	45	1F,1OH	0.82	35
110	3F+1H ₂ O	0.26	16	2F,1OH _a +1H ₂ O	0.55	53	2F,1OH _b	0.54	46
	$p_{\text{H}_2\text{O}} = 10^{-3}$ atm/ $p_{\text{HF}} = 1$ atm								
001	2F+1H ₂ O	0.66		2F+1H ₂ O	0.95	–	2F	1.15	–
100	1F+1HF	0.10		1F+1HF	0.41	11	1F+1HF	0.74	10
101	2F+1HF	–0.04	n.d.	2F+1HF	0.30	68	2F+1HF	0.66	50
110	3F+1HF	0.17		3F+1HF	0.39	22	3F+1HF	0.62	40

4.4.2 MP2 versus DFT for surface thermodynamics

In paper **P1**, the performance of the two methods on the adsorption was studied on a variety of structures. The conclusion was that DFT adequately describes simple cases, as the adsorption of HF on clean surfaces, but it does not perform as well – or completely fails – on the adsorption of water on clean and hydroxylated surfaces.

However, comparing the phase diagrams based on DFT energies in paper **P2** to those presented in this section the differences are not as prominent. One should keep in mind, that the surface diagrams are not exactly comparable with respect to the occurring terminations due to certain discrepancies in the structures included. For instance, low coverage – 25% for H_2O , and 25% and 50% for HF – is not included in the MP2 study due to the high computational cost of the calculations. This is also the case for a number of hydroxylation patterns: degrees of hydroxylation so low that would require the calculation of supercells, or complete hydroxylation for surface (101) have not been included in the MP2 diagrams.

Bearing that in mind, the two methods capture predominantly the same trends. It was observed in paper **P1**, that the adsorption energies calculated with DFT are in general lower than those calculated with MP2. In line with this result, adsorption structures appear earlier – at lower pressure – in the phase diagrams with MP2. The effect is pronounced in water-covered hydroxylated terminations, which – as seen in **P1** – DFT describes poorly, causing in the phase diagram of (110) at 600 K the only case of qualitative discrepancy: At low p_{HF} with increasing $p_{\text{H}_2\text{O}}$ the clean termination (6F) gives its place to $(2\text{F}, 1\text{OH}_b)$, which is followed by $(2\text{F}, 1\text{OH}_b + \text{H}_2\text{O})$, according to DFT. According to MP2 however, H_2O adsorption stabilizes the other hydroxylated termination, causing a transition from termination $(2\text{F}, 1\text{OH}_b)$ to $(2\text{F}, 1\text{OH}_a + \text{H}_2\text{O})$.

The same applies to the Wulff plots. It was seen in section 4.1 that the two methods predict the same crystal shape for MgF_2 based on the quantum chemical surface energies. This is also the case at conditions of finite temperature and pressure, where the relative exposure of the surfaces and consequently the shape of the crystals are comparable. Minor discrepancies in the predicted crystal shape are observed at conditions where adsorption plays a major role and goes hand in hand with differences regarding the predicted termination: For instance at 450 K, $p_{\text{H}_2\text{O}} = 10^{-3}$ atm and $p_{\text{HF}} = 10^{-12}$ atm, the combination of hydroxylation and adsorption of H_2O leads to a stabilization of (110) at the expense of (100). On the other hand at $p_{\text{H}_2\text{O}} = 10^{-3}$ atm and $p_{\text{HF}} = 1$ atm at the same temperature, (110) is covered with HF according to MP2 results, but with H_2O according to DFT, without this significantly affecting the relative exposure of the surfaces.

4.5 A force field for MgF_2

4.5.1 Embedded clusters as a model for MgF_2 bulk

To extend the modelling of crystallites in the mesoscale, a classical force field is parametrized to reproduce the DFT energies for the MgF_2 bulk. To this end, the previously

published force field by Catti *et al.* [78] for rutile-type MgF_2 bulk is used as a starting point. It consists of Coulomb-Buckingham pair potentials:

$$E_{ij} = \frac{e^2 z_i z_j}{r_{ij}} + b_{ij} \exp\left(\frac{-r_{ij}}{\rho}\right) - \frac{d_{ij}}{r_{ij}^6}, \quad (4.4)$$

with dispersion coefficients d_{ij} derived from theoretical and experimental data; the repulsion coefficients have been expressed as $b_{ij} = \exp\left(\frac{r_i + r_j}{\rho}\right)$. The ionic radii r_{F} and r_{Mg} , the parameter ρ and the ionic charges z_{F} , z_{Mg} (with $2z_{\text{F}} + z_{\text{Mg}} = 0$) have been fitted to reproduce Hartree-Fock results for the elastic tensors of MgF_2 . The b_{ij} and d_{ij} coefficients of Catti's force field are listed in table 4.7, the value for ρ is 0.205 \AA , and for z_{F} and z_{Mg} -0.83 and 1.66 respectively.

Table 4.7: Parameters of the pair potentials in Catti's force field [78], employed for the testing of the embedded cluster scheme. b_{ij} in eV, d_{ij} in eV \AA^6 .

	F-F	F-Mg	Mg-Mg
b_{ij}	17039.097	4166.247	905.517
d_{ij}	15.168	2.901	0.5557

Catti's force field is used to examine the suitability of embedded clusters as an approximation for MgF_2 bulk. To this end, a translational asymmetric unit of MgF_2 is embedded in rutile-type clusters cut following two strategies:

- The six atoms of a translational asymmetric unit are embedded in quasi-spherical clusters of varying radii.⁴
- The original translational asymmetric unit is the centre of a cuboid embedding cluster, the edges of which have a length of $2n+1$ units.

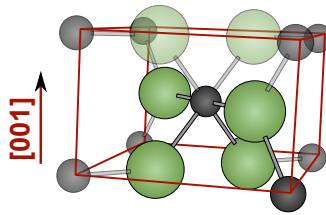


Figure 4.13: The unit cell of rutile-type MgF_2 . Black spheres represent magnesium and green spheres fluorine. In opaque, the atoms of the translational asymmetric unit.

In both cases, the energy of the central translational asymmetric unit is calculated in gradually growing clusters; it corresponds to a bulk energy per unit cell. In case (a),

⁴Starting from bulk MgF_2 , the clusters contain all atoms located within a set radius from at least one of the six atoms of the translational asymmetric unit.

the resulting clusters are symmetric, but as shown at the bottom of fig. 4.14(a) they are charged, and their charge diverges with growing size. The clusters of series (b) are stoichiometric and neutral. However, as a consequence of the shape of the translational asymmetric unit (fig. 4.13), they have in two directions a macroscopic dipole moment.

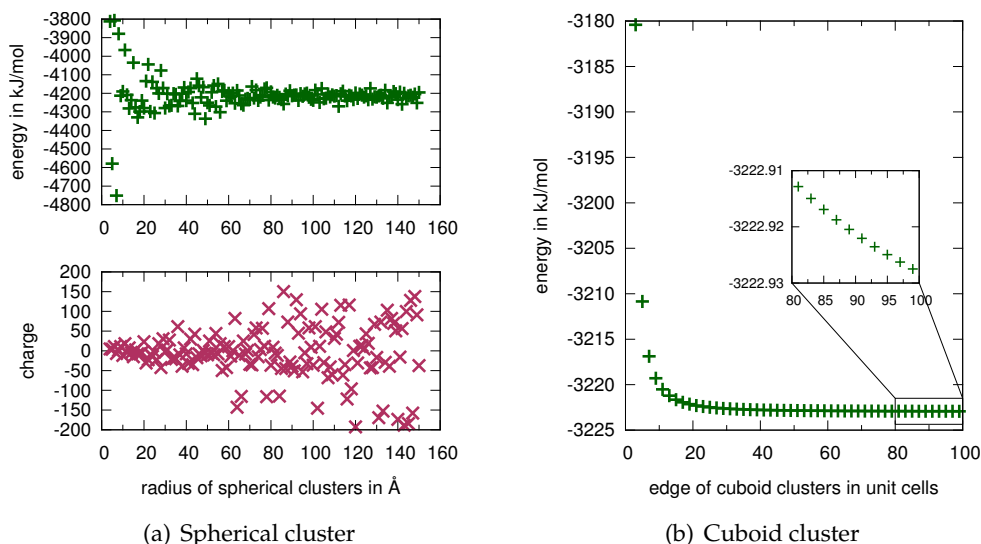


Figure 4.14: Energy of a unit cell of MgF_2 embedded in spherical and cuboid clusters. For spherical clusters, the charge of the embedding clusters is also plotted. The cuboid clusters are neutral but have a macroscopic dipole moment.

At first glance, both energy series in fig. 4.14 seem to converge. Unfortunately, they do so in different limits: The quasi-spherical series converges to a bulk energy of approximately -4217 kJ/mol, while the cuboid series to a value of -3223 kJ/mol. Besides, one should be cautious when claiming convergence: a closer look at the tail of the cuboids' series reveals that even when approaching the $100 \times 100 \times 100$ cluster, the bulk energy keeps decreasing, although very slowly, monotonically. The spherical clusters' series shows better signs of convergence, however in the range of radii between 100 and 160 Å, the bulk energy values show a deviation of approximately 80 kJ/mol. When evaluating these results, one should keep in mind that the series plotted in fig. 4.14 expand to a ridiculously large size of clusters: for example, a spherical cluster of radius 100 Å already consists of 393440 atoms and a cuboid cluster with edges of 81 unit cells consists of 3188646 atoms.

A modelling of the MgF_2 bulk with embedded clusters and the calculation of the bulk energy via direct summation has thus proven to be unsuitable. For an infinite periodic system as the one to be modelled in this work, the exponential and the dispersion term of Coulomb-Buckingham pair potentials do not constitute a problem, owing to their rapid convergence: It is sufficient to calculate the interaction of pairs up

to a cutoff of a few Ångström for r_{ij} . The Coulomb term, on the other hand, shows a significantly slower converge and is sensitive to macroscopic dipole moments. Therefore, a different strategy should be pursued for the calculation of the electrostatic interactions of bulk MgF_2 . In the following, the electrostatic interaction is calculated via Ewald summation.

4.5.2 Fitted force fields

A number of fits were performed according to the procedure described in section 3.4, with varying fitting parameters. The quality of the fitting, the performance regarding the EOS and the shape of the individual pair potentials will be discussed for a selection of them.

Table 4.8: Parameters of selected fitted force fields. d is given in $\sqrt{\text{eV}}\text{\AA}^3$, b in $\sqrt{\text{eV}}$ and ρ in \AA . The simulation box is measured in number of unit cells. A weighting of 3p·10+4p·5 means that the error of the minimum and of one neighbouring point on each side are weighted by a factor of 10 and two further points on each side by a factor of 5.

	d_{Mg}	b_{Mg}	d_{F}	b_{F}	ρ	sim. box	$w\{V\}$
fit 1	0.381	37.311	4.806	178.557	0.205	$2 \times 2 \times 2$	none
fit 2	-1.425	292.223	9.582	20.385	0.225	$3 \times 3 \times 3$	none
fit 3	-0.240	57.582	4.482	144.315	0.202	$2 \times 2 \times 2$	7p·5
fit 4	0.083	78.669	7.733	97.739	0.209	$3 \times 3 \times 3$	7p·5
fit 5	0.495	38.561	9.646	98.697	0.231	$3 \times 3 \times 3$	3p·10+4p·5
fit 6	6.217	9.614	6.519	73.068	0.284	$3 \times 3 \times 3$	11p·10

The size of the simulation box, the weighting scheme – where applicable – and the fitted parameters are presented in table 4.8. Fits 1 and 3 were performed in $2 \times 2 \times 2$ simulation boxes, and all others in $3 \times 3 \times 3$ boxes, which correspond to cutoffs of 6.16 Å and 9.24 Å, respectively; obviously, the latter is expected to give a description of higher quality, since more interactions are taken into account. The last column in table 4.8 refers to the weighting scheme of the errors during fitting. In the first two fits, no weighting is applied. In fits 3 and 4, the DFT minimum and its three neighbouring points in each direction, seven points in total, are weighted by a factor of 5. By analogy, eleven points are weighted by 10 in fit 6. In fit 5, a graded scheme has been applied, in which three points (the DFT minimum and its two neighbours) are weighted by 10 and the following four points – two in each direction – are weighted by 5. Yet before discussing the fitted parameters, the reader is invited to take a look at the graphical representation of the EOS in fig. 4.15.

The EOS ($E_{\text{bulk}}^{\text{shifted}}$ vs volume) have been created using the parameters of the fitted force fields. For comparison, an EOS has been created with Catti’s parameters for the short-range interaction, shifted to match the DFT range. All series show a pro-

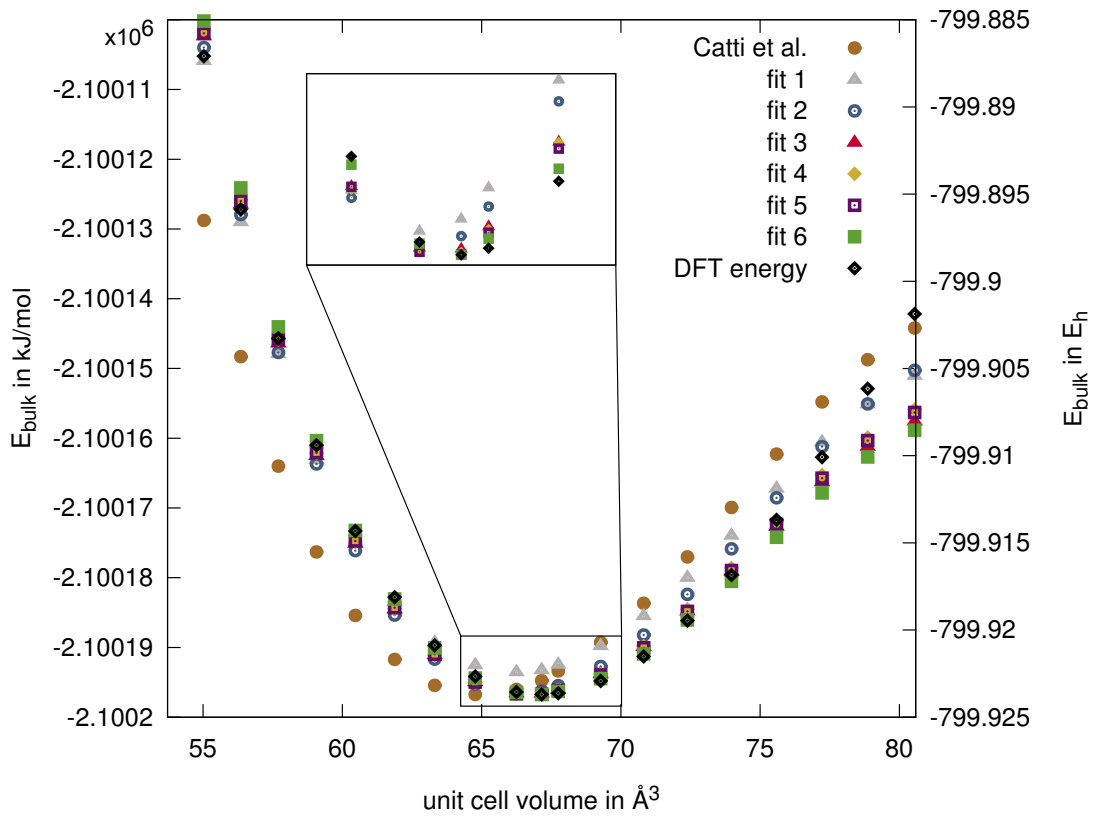


Figure 4.15: EOS for MgF_2 bulk calculated with periodic DFT, literature and fitted force fields. The force field energies are shifted to match the DFT range. The ‘Catti *et al.*’ series has been removed from the close-up to improve readability.

nounced anharmonicity at very large expansion factors, which is not observed in the DFT series. As expected, Catti’s pair potential does not reproduce the EOS from DFT. In accordance to their Hartree-Fock calculation, which gives a unit cell volume of 66.4 \AA^3 , the force field underestimates the volume of the unit cell as well. The fitted force fields reproduce the DFT energies for small cell volumes and around the minimum satisfactorily. An exception are fits 1 and 2, the minimum of which is shifted towards smaller volume with respect to DFT.

The quality of the fitted force fields is quantified in table 4.9, by means of errors, mean absolute error and standard deviation. The error values for E_{bulk} support the visual observations made above. The failure of the fits at the large volume range is reflected by the amplitude of the errors, which – for the last two points in each series – is a multiple of the mean absolute error $|\overline{\Delta E_{\text{bulk}}}|$; the mean absolute error itself takes very similar values for all fits. Additional information, however, can be extracted from the standard deviation σ . When calculated over the entire series, the σ value close to 3 suggests that fits 1 and 2 are better choices compared to fits 4 and 5 with a standard deviation larger than 4, or fit 6 with $\sigma \approx 5$. Since the DFT energies are more

Table 4.9: Error, sum of absolute errors and standard deviation of the fitted bulk energy E_{bulk} . The standard deviation is calculated for the entire series (σ) and for five points around the minimum (σ_5). Volume of the unit cell in \AA^3 , errors' values in kJ/mol.

expansion	volume	ΔE_{bulk}					
		Fit 1	Fit 2	Fit 3	Fit 4	Fit 5	Fit 6
0.800	53.72	4.52	4.06	5.96	6.90	6.10	7.58
0.819	55.03	1.17	1.25	2.90	3.73	3.28	5.03
0.839	56.36	-1.13	-0.75	0.73	1.40	1.21	3.08
0.859	57.70	-2.52	-2.03	-0.70	-0.18	-0.21	1.64
0.880	59.07	-3.16	-2.69	-1.50	-1.15	-1.06	0.66
0.900	60.47	-3.16	-2.81	-1.77	-1.57	-1.43	0.08
0.921	61.88	-2.74	-2.57	-1.72	-1.64	-1.50	-0.26
0.943	63.31	-1.97	-1.99	-1.38	-1.40	-1.29	-0.36
0.964	64.77	-0.87	-1.08	-0.77	-0.85	-0.79	-0.22
0.987	66.25	0.30	-0.08	-0.14	-0.25	-0.26	-0.04
1.000	67.15	0.95	0.49	0.16	0.06	0.01	0.00
1.009	67.75	1.59	1.09	0.58	0.48	0.41	0.25
1.032	69.27	2.66	2.09	1.04	1.01	0.85	0.32
1.055	70.82	3.65	3.08	1.41	1.48	1.26	0.37
1.078	72.39	4.28	3.78	1.40	1.63	1.33	0.11
1.102	73.97	4.08	3.75	0.57	0.99	0.64	-0.91
1.126	75.59	3.25	3.17	-0.91	-0.24	-0.64	-2.48
1.150	77.22	1.26	1.51	-3.55	-2.59	-3.02	-5.12
1.174	78.86	-2.86	-2.19	-8.30	-7.02	-7.45	-9.79
1.199	80.55	-9.28	-8.08	-15.35	-13.70	-14.12	-16.66
$ \overline{\Delta E_{\text{bulk}}} $		2.77	2.43	2.54	2.41	2.34	2.75
σ		3.37	2.96	4.36	4.02	4.04	5.01
σ_5		1.13	0.98	0.73	0.73	0.68	0.41

reliable close to the equilibrium structure than further away, the standard deviation is calculated again, this time limited to five points around the minimum. The new standard deviation, σ_5 , presents a different picture: With a $\sigma_5 \approx 0.4$, fit 6 appears to be notably better than the others, followed by fits 3–5 with $\sigma_5 \approx 0.7$, and fits 1 and 2 with $\sigma_5 \approx 1.0$. Nevertheless, the data in table 4.9 should be interpreted with caution. The bulk energy in the EOS is calculated as a sum of pair interactions, some of which are attractive, and some repulsive. That leaves open the possibility of individual pair interactions cancelling out, thus producing coincidentally good results for the total energy.

Indeed, turning to the individual pair potentials plotted in fig. 4.16, this scepticism proves to be justified. The first observation to be made is, that the – according to the

plotted EOS – well-behaved fit 6 must be rejected, due to the shape of pair potentials Mg-Mg and Mg-F caused by the low value for b_{Mg} . As a consequence of b_{Mg} and d_{Mg} having the same order of magnitude, the intrinsic weakness of the Coulomb-Buckingham potential, the “turning over” for small values of r_{ij} [148], is pronounced for the pair Mg-Mg. Considering that the distance between Mg atoms in the bulk is 3.08 Å, the rather shallow barrier between 2–3 Å is unlikely to be sufficient to prevent “nuclear fusion” during simulation. The low b_{Mg} value affects the Mg-F potential as well, making it monotonically attractive, thus also useless for simulations. Fits 2 and 3 have to be rejected as unphysical. Their negative values for d_{Mg} cancel out in the Mg-Mg potential, but – though not visible in the graph – result in a repulsive dispersion for the pair Mg-F. Moreover, the potential for pair F-F in fit 2 falls monotonically towards negative infinity with decreasing r_{ij} due to the low values of b_{F} .

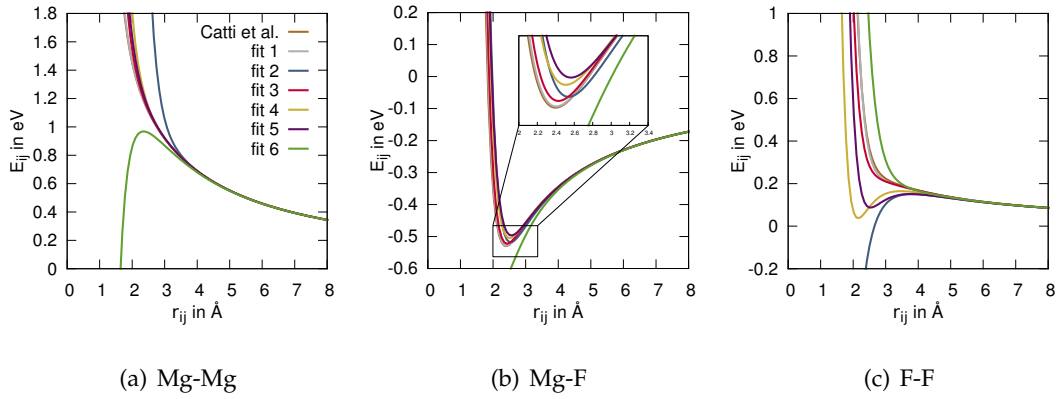


Figure 4.16: Analytical plot of Coulomb-Buckingham pair potentials with fitted and literature parameters for MgF_2 .

The detailed examination of the fitted force fields showed that the parametrization of force fields for solids based solely on the EOS is not sufficient. Thus, not only the performance of the force fields in reproducing the bulk energies obtained with DFT but also the behaviour of the individual pair potentials need to be taken into consideration for the evaluation of the presented fits. Based on these criteria, fits 4 and 5 are acceptable and are employed in the following.

4.5.3 Validation of the force fields

In the previous section, the force fields were evaluated with respect to their performance in the periodic system. Objective is, however, their application to the modelling of nanocrystals, so their behaviour in non-periodic systems is of importance as well. For further evaluation of the suitability of the force fields, they are tested on cluster structures.

Four neutral MgF_2 clusters have been cut from the optimized bulk structure, presented in fig. 4.17; each cluster consists of 24 Mg and 48 F atoms. Cluster (a) has

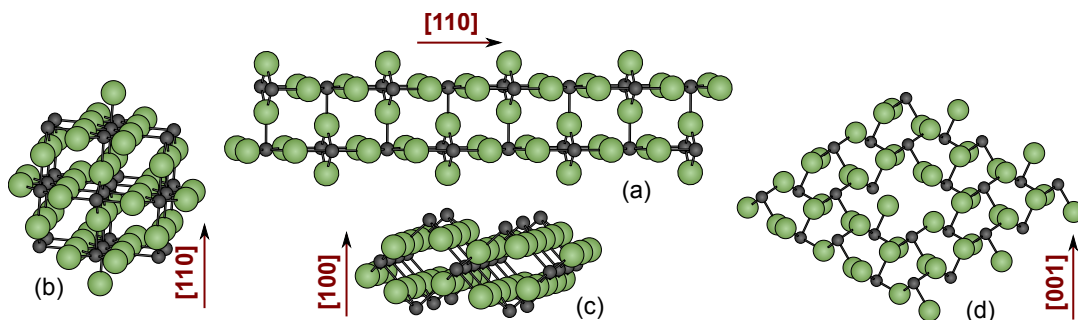


Figure 4.17: Clusters for validation of the force field, cut from the relaxed bulk structure of rutile-type MgF_2 . All clusters are neutral and consist of 72 atoms: 24 Mg and 48 F.

the shape of a rod, the long side of which consists of 24 atomic layers parallel to the (110) surface while the short sides consist of 3 and 5 atomic layers, resulting in dimensions of $25.7 \times 3.1 \times 5.9 \text{ \AA}$. Cluster (b) is a quasi-spherical cluster with maximal dimensions of $9.2 \times 9.2 \times 8.9 \text{ \AA}$. Structure (c) is a flat cluster, the large side of which is cut along the (100) surface, with a thickness of 7 atomic layers. Its dimensions are $15.41 \times 11.2 \times 4.7 \text{ \AA}$. The last cluster, (d), is a thin film of (001) consisting of 2 atomic layers, with dimensions $20.5 \times 20.5 \times 1.54 \text{ \AA}$; one missing Mg and two F atoms form a vacancy in the centre of the cluster. These structures are not necessarily what a MgF_2 nanocrystal is expected to look like. They are chosen such that they represent different distributions of pair distances.

Table 4.10: Energy of the clusters, in kJ/mol, obtained from DFT, and from MM calculations with the two best fitted force fields. The energies are given with respect to the total energy of the most stable cluster, (a), the energy of which is set to zero.

cluster	DFT	Fit 4	Fit 5
a	0.00	0.00	0.00
b	743.18	640.31	508.82
c	1898.55	1830.35	1717.64
d	2296.95	1818.56	1838.73

The total energy of these structures is calculated with single-point DFT, and with the two force fields. According to the DFT calculations, cluster (a) is the most stable of the four. It is followed by structures (b), (c) and (d), in that order. Naturally, the quantum chemical energies lie on a different range than the energies calculated with force fields. Of interest, however, is whether the force fields predict the same trends in the energy as DFT. The most stable cluster, (a), is regarded as a reference for the comparison of the relative stability of the structures.

In table 4.10, the energy of the clusters is given as their difference to the energy of

the reference. Both force fields underestimate the energy of the less stable clusters compared to DFT. For clusters (b) and (c), fit 4 predicts ΔE_{tot} lower than DFT by 103 kJ/mol and 68 kJ/mol respectively, while fit 5 by 234 kJ/mol and 181 kJ/mol. On the other hand for cluster (d), which is the least stable of the four, the discrepancy between DFT and force fields is significantly larger. Fit 4 predicts a ΔE_{tot} lower by 478 kJ/mol, whereas fit 5 by 458 kJ/mol than DFT.

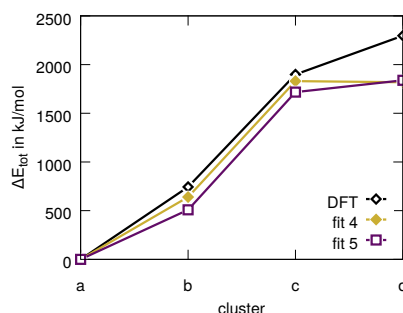


Figure 4.18: Total energy of the clusters from DFT and fitted force fields with respect to the most stable structure, in kJ/mol. Lines between points are drawn for clarity and do not imply continuity between the structures.

The decision, which force field is better suited for the modelling of MgF_2 clusters, can only be met under consideration of the mechanics of the simulation in which it will be employed. Based merely on the values of ΔE_{tot} , fit 4 performs overall better than fit 5. However, it reverses the energetic order of the two least stable clusters. Consequence of the reversing would be, for instance, in the case of a simple geometry optimization with MM, a step from structure (c) to structure (d) to be accepted with force field 4 but not with force field 5. In this respect, fit 5 is in better accord to DFT, and is therefore proposed as more suitable for the modelling of MgF_2 in a multiscale approach.

An additional consideration is to be given to the observables used for fitting. Until now, the force field is fitted and tested only with respect to total energies, but not with respect to forces. Therefore in the present state, it should be employed with caution in MD simulations, which base on the equation of motion to propagate the system. A safer choice is its use in Metropolis Monte Carlo simulations [149], in which the propagation of the system is based on the energy.

5 Publications

5.1 Paper P1

Elisavet Kanaki, Giuseppe Sansone, Lorenzo Maschio and Beate Paulus,
Phys. Chem. Chem. Phys., **2015**, 17, 18722–18728

DOI: 10.1039/C5CP02017D

<http://dx.doi.org/10.1039/C5CP02017D>

5.2 Paper P2

Elisavet Kanaki, Sebastian Gohr, Carsten Müller and Beate Paulus,
Surf. Sci. **2015**, 632, 158–163

DOI: 10.1016/j.susc.2014.10.007

<http://dx.doi.org/10.1016/j.susc.2014.10.007>

6 Conclusions

The aim set at the beginning of this work was the better understanding of the properties behind the catalytic activity of MgF_2 -based nanomaterial. Having determined the suitable method to investigate the properties of MgF_2 surfaces and having completed the extensive study of different terminations and the adsorption of H_2O and HF on them, it is sensible to go back to the starting point of this work: the experimental findings. It is in general assumed, that coordinatively unsaturated cations are the key to catalytic activity – and that the more neighbours the cation misses, the higher is its activity. That is partly true, but it is only one aspect. After having investigated a number of adsorption patterns, one can conclude that the surface anions and the particular surface structure play a role just as important for the interaction with the adsorbates, at least for polar molecules.

Wuttke *et al.* [16] have postulated different types of surface hydroxyls: terminal and bridging, based on their coordination; free, hydrogen-bonded and interacting with neighbouring unsaturated cations, based on their interactions with adjacent sites. The theoretical findings of the present work confirm the existence of bridging hydroxyls on the surface, usually coordinated to two cations. Terminal hydroxyls do not occur among the structures studied, as the terminations of pure and stoichiometric MgF_2 slabs do not contain singly coordinated surface fluorines. A relaxation of the structure occurs upon hydroxylation, however the change in the structure of the surface is not so pronounced as to result in the formation of terminal hydroxyls. Hydrogen bonding between surface hydroxyls and fluorines is not supported by findings in this work either. On low-index surfaces, hydroxyls are sterically prevented from interacting with adjacent fluorines, but also on the stepped surface (103) an interaction is not observed.

Experimental studies indicate that the properties of surface hydroxyls of MgF_2 depend on their concentration. The Brønsted-basic nature of surface hydroxyls was experimentally observed at very high concentration on the surface of nanostructured material [12], in agreement with observations on polycrystalline MgF_2 [21]. In the present theoretical study a similar behaviour is observed in the context of HF adsorption on hydroxylated terminations. The F-end of the molecule coordinates to the cation and the H-end forms a symmetric hydrogen bond to the hydroxyl, indication of a tendency for re-fluorination of the surface along with formation of H_2O . According to experimental findings [31], surface hydroxyls at low concentration exhibit Brønsted-acidic activity. The modelled adsorption systems are not suitable for the investigation of hydrogen-donating properties. However, surface hydroxyls show acidic behaviour in some occasions, acting as adsorption sites for H_2O .

The basicity of surface fluorines is evident in all calculated structures, as adsorbates always lie approximately parallel to the surfaces. Based on data from IR spectroscopy, Wuttke *et al.* [31] proposed two adsorption schemes for H_2O on MgF_2 surfaces, involving two or one hydrogen bonds to surface fluorines. The present study confirms both schemes, depending on the availability of surface anions for the formation of hydrogen bonds. The same is true for HF: the F-end interacts with surface cations while the H-end with surface anions. As a consequence H_2O adsorbs preferably on fourfold, whereas HF on fivefold coordinated cations.

In discussions concerning the catalytic activity of nanoscopic metal fluorides, the focus is usually on the Lewis-acidity of coordinatively unsaturated cations. The theoretical results show that the basicity of the ligands can play a role of similar importance. The calculated adsorption energies of H_2O and HF show a dependence on hydrogen bonding to the basic sites. The observed adsorption structures in principle support the scheme proposed by Astruc *et al.* [17] for MgF_2/HF as fluorinating agent, although the formation of chains of adsorbed HF molecules on surface fluorines was not explicitly modelled. Also the mechanism proposed by Teinz *et al.* [18] for dehydrohalogenation on metal fluorides is supported by the theoretical findings.

The second aim of this work was to develop a model for the prediction of the morphology of magnesium fluoride crystals at conditions of finite temperature and pressure. To this end, quantum chemical calculations were combined with surface thermodynamics. The resulting phase diagrams illustrate the relative stability of different terminations, depending on temperature and pressure. Using the data from the phase diagrams, Wulff plots were created as a model for MgF_2 crystals at different conditions. It was shown that pure MgF_2 terminations are the most stable at vacuum conditions, regardless of the temperature. The presence of H_2O or HF in the gas phase favours the adsorption of the corresponding molecules, affecting the relative stability of the surfaces, and as a consequence the shape of the crystallites. Hydroxylated surfaces occur with increasing temperature in presence of H_2O . Unfortunately, the predictions of the model can not be validated for the case of sol-gel synthesized material, due to the lack of suitable experimental data.

The comparison of quantum chemical methods shows that their performance depends on the nature of the addressed question. Pure MgF_2 structures are described adequately with Hartree-Fock, but hydroxylated surfaces and adsorption interactions require treatment on a higher level of theory. The relative stability of these surfaces and the prediction of the crystal morphology is satisfactory with DFT/B3LYP. However, MP2 is required for the detailed description of adsorption interactions. The expertise gained in this work is not specific to MgF_2 . It provides information on the limits of each method, that can be valuable for the theoretical investigation of other similar systems.

An insight was gained in the individual interactions behind the catalytic activity of magnesium fluoride, supporting some of the experimental observations. From the results it is evident that numerous factors influence the interaction of the surfaces even with small molecules. Since the nanoscopic material has a high density of de-

fects, modelling the crystallites beyond the periodic model is an intriguing task. To this end, a force field for MgF_2 was developed for the use in classical simulations. As it has been parametrized to reproduce the DFT energies, the force field is particularly suited for multiscale models: Structures based on Wulff plots can be used as starting point to simulate nanocrystals with classical force fields, extending the model in the mesoscale. An equally intriguing question concerns the predictive strength of the model for the surface properties of MgF_2 . Towards this direction, the next step would be the development of a suitable experimental setup for the validation of the theoretical model. It is now the experiment's turn to challenge the theoretical results, so that the scientific journey can go on.

Bibliography

- [1] P. J. Crutzen, *Nature*, 2002, **415**, 23.
- [2] P. T. Anastas, and M. M. Kirchhoff, *Acc. Chem. Res.*, 2002, **35**, 686–694.
- [3] P. T. Anastas, M. M. Kirchhoff and T. C. Williamson, *Appl. Catal. A*, 2001, **221**, 3–13.
- [4] D. Astruc, F. Lu and J. R. Aranzaes, *Angew. Chem. Int. Ed.*, 2005, **44**, 7852–7872.
- [5] M. Wojciechowska and R. Fiedorow, *J. Fluorine Chem.*, 1980, **15**, 443–452.
- [6] E. Kemnitz, U. Groß, S. Rüdiger and C. S. Shekar, *Angew. Chem. Int. Edit.*, 2003, **42**, 4251–4254.
- [7] E. Kemnitz, *Catal. Sci. Technol.*, 2015, **5**, 786–806.
- [8] I. Agirrezabal-Telleria, F. Hemmann, C. Jäger, P. Arias and E. Kemnitz, *J. Catal.*, 2013, **305**, 81–91.
- [9] H. A. Prescott, Z.-J. Li, E. Kemnitz, J. Deutsch and H. Lieske, *J. Mater. Chem.*, 2005, **15**, 4616–4628.
- [10] A. Negoï, S. Wuttke, E. Kemnitz, D. Macovei, V. I. Parvulescu, C. M. Teodorescu and S. M. Coman, *Angew. Chem. Int. Ed.*, 2010, **49**, 8134–8138.
- [11] Y. Guo, S. Wuttke, A. Vimont, M. Daturi, J.-C. Lavalley, K. Teinz and E. Kemnitz, *J. Mater. Chem.*, 2012, **22**, 14587–14593.
- [12] S. Wuttke, S. M. Coman, G. Scholz, H. Kirmse, A. Vimont, M. Daturi, S. L. M. Schroeder and E. Kemnitz, *Chem.–Eur. J.*, 2008, **14**, 11488–11499.
- [13] S. M. Coman, V. I. Parvulescu, S. Wuttke and E. Kemnitz, *ChemCatChem*, 2010, **2**, 92–97.
- [14] S. M. Coman, V. I. Parvulescu, S. Wuttke and E. Kemnitz, *ChemCatChem*, 2010, **2**, 92–97.
- [15] S. Célérier and F. Richard, *Catalysis Communications*, 2015, **67**, 26 – 30.
- [16] S. Wuttke, S. Coman, J. Kröhnert, F. Jentoft and E. Kemnitz, *Catalysis Today*, 2010, **152**, 2 – 10.

- [17] A. Astruc, C. Cochon, S. Dessources, S. Célérrier and S. Brunet, *Appl. Catal. A*, 2013, **453**, 20–27.
- [18] K. Teinz, S. Wuttke, F. Börno, J. Eicher and E. Kemnitz, *J. Catal.*, 2011, **282**, 175–182.
- [19] E. Kemnitz, S. Wuttke and S. M. Coman, *Eur. J. Inorg. Chem.*, 2011, **2011**, 4773–4794.
- [20] N. Candu, S. Wuttke, E. Kemnitz, S. Coman and V. Parvulescu, *Appl. Catal. A*, 2011, **391**, 169–174.
- [21] M. Wojciechowska, M. Zieliński and M. Pietrowski, *J. Fluorine Chem.*, 2003, **120**, 1–11.
- [22] G. Scholz, C. Stosiek, J. Noack and E. Kemnitz, *J. Fluorine Chem.*, 2011, **132**, 1079–1085.
- [23] M. Karg, G. Scholz, R. König and E. Kemnitz, *Dalton Trans.*, 2012, **41**, 2360–2366.
- [24] J. Noack, *Ph.D. thesis*, Humboldt-Universität zu Berlin, 2001.
- [25] J. Haines, J. M. Léger, F. Gorelli, D. D. Klug, J. S. Tse and Z. Q. Li, *Phys. Rev. B*, 2001, **64**, 134110.
- [26] A. D. Becke, *Phys. Rev. A*, 1988, **38**, 3098–3100.
- [27] C. Lee, W. Yang and R. G. Parr, *Phys. Rev. B*, 1988, **37**, 785–789.
- [28] Z. Huesges, C. Müller, B. Paulus, C. Hough, N. Harrison and E. Kemnitz, *Surf. Sci.*, 2013, **609**, 73–77.
- [29] J. M. Thomas and W. J. Thomas, *Principles and practice of heterogeneous catalysis*, VCH, 1997.
- [30] K. I. Hadjiivanov and G. N. Vayssilov, *Advances in Catalysis*, 2002, **47**, 307–511.
- [31] S. Wuttke, A. Vimont, J.-C. Lavalley, M. Daturi and E. Kemnitz, *J. Phys. Chem. C*, 2010, **114**, 5113–5120.
- [32] H. Lüth, *Surfaces and Interfaces of Solid Materials*, Springer, 1995.
- [33] C. Müller, *Ph.D. thesis*, Uppsala Universitet, 2009.
- [34] H. Stoll, *Chem. Phys. Lett.*, 1992, **191**, 548–552.
- [35] H. Stoll, *J. Chem. Phys.*, 1992, **97**, 8449–8454.
- [36] H. Stoll, *Phys. Rev. B*, 1992, **46**, 6700–6704.
- [37] C. Muller and B. Paulus, *Phys. Chem. Chem. Phys.*, 2012, **14**, 7605–7614.

- [38] C. Møller and M. S. Plesset, *Phys. Rev.*, 1934, **46**, 618–622.
- [39] C. Pisani, L. Maschio, S. Casassa, M. Halo, M. Schütz and D. Usvyat, *J. Comput. Chem.*, 2008, **29**, 2113–2124.
- [40] C. Pisani, M. Schütz, S. Casassa, D. Usvyat, L. Maschio, M. Lorenz and A. Erba, *Phys. Chem. Chem. Phys.*, 2012, **14**, 7615–7628.
- [41] G. Kresse and J. Hafner, *Phys. Rev. B*, 1993, **47**, 558–561.
- [42] G. Kresse and J. Hafner, *Phys. Rev. B*, 1994, **49**, 14251–14269.
- [43] G. Kresse and J. Furthmüller, *Comput. Mat. Sci.*, 1996, **6**, 15–50.
- [44] G. Kresse and J. Furthmüller, *Phys. Rev. B*, 1996, **54**, 11169–11186.
- [45] J. Sauer, P. Ugliengo, E. Garrone and V. R. Saunders, *Chemical Reviews*, 1994, **94**, 2095–2160.
- [46] L. Hammerschmidt, L. Maschio, C. Müller and B. Paulus, *J. Chem. Theory Comput.*, 2015, **11**, 252–259.
- [47] Y. Andersson, D. C. Langreth and B. I. Lundqvist, *Phys. Rev. Lett.*, 1996, **76**, 102–105.
- [48] D. C. Langreth, M. Dion, H. Rydberg, E. Schröder, P. Hyldgaard and B. I. Lundqvist, *Int. J. Quantum Chem.*, 2005, **101**, 599–610.
- [49] T. Sato, T. Tsuneda and K. Hirao, *Mol. Phys.*, 2005, **103**, 1151–1164.
- [50] O. A. von Lilienfeld, I. Tavernelli, U. Rothlisberger and D. Sebastiani, *Phys. Rev. Lett.*, 2004, **93**, 153004.
- [51] Y. Y. Sun, Y.-H. Kim, K. Lee and S. B. Zhang, *J. Chem. Phys.*, 2008, **129**, 154102.
- [52] Y. Zhao and D. G. Truhlar, *Acc. Chem. Res.*, 2008, **41**, 157–167.
- [53] S. Grimme, *J. Comput. Chem.*, 2006, **27**, 1787–1799.
- [54] S. Grimme, J. Antony, S. Ehrlich and H. Krieg, *J. Chem. Phys.*, 2010, **132**, 154104.
- [55] R. Dovesi, R. Orlando, B. Civalleri, C. Roetti, V. R. Saunders and C. M. Zicovich-Wilson, *Z. Kristallogr.*, 2005, **220**, 571–573.
- [56] R. Dovesi, V. Saunders, C. Roetti, R. Orlando, C. M. Zicovich-Wilson, F. Pascale, B. Civalleri, K. Doll, N. Harrison, I. Bush, P. D’Arco and L. M., *CRYSTAL09 User’s Manual*, University of Torino, Torino, 2010.
- [57] B. Civalleri, C. M. Zicovich-Wilson, L. Valenzano and P. Ugliengo, *CrystEngComm*, 2008, **10**, 405–410.

- [58] S. Ehrlich, J. Moellmann, W. Reckien, T. Bredow and S. Grimme, *ChemPhysChem*, 2011, **12**, 3414–3420.
- [59] C. Stampfl, M. V. Ganduglia-Pirovano, K. Reuter and M. Scheffler, *Surf. Sci.*, 2002, **500**, 368–394.
- [60] G. Ertl, *J. Mol. Catal. A: Chem.*, 2002, **182-183**, 5–16.
- [61] C. Stampfl, H. J. Kreuzer, S. H. Payne, H. Pfnür and M. Scheffler, *Phys. Rev. Lett.*, 1999, **83**, 2993–2996.
- [62] K. Reuter and M. Scheffler, *Phys. Rev. B*, 2001, **65**, 035406.
- [63] W.-X. Li, C. Stampfl and M. Scheffler, *Phys. Rev. B*, 2003, **68**, 165412.
- [64] F. Zasada, W. Piskorz and Z. Sojka, *J. Phys. Chem. C*, 2015, **119**, 19180–19191.
- [65] N. İnoğlu and J. R. Kitchin, *J. Catal.*, 2009, **261**, 188–194.
- [66] M.-T. Nguyen, M. Farnesi Camellone and R. Gebauer, *J. Chem. Phys.*, 2015, **143**, 034704.
- [67] T. S. Bjørheim and E. Kotomin, *J. Phys. Chem. Lett.*, 2014, **5**, 4238–4242.
- [68] A. I. Duff, L. Lymperakis and J. Neugebauer, *Phys. Status Solidi B*, 2015, **252**, 855–865.
- [69] P. Ágoston and K. Albe, *Surf. Sci.*, 2011, **605**, 714–722.
- [70] A. Marmier and S. C. Parker, *Phys. Rev. B*, 2004, **69**, 115409.
- [71] A. K. Rappe, C. J. Casewit, K. S. Colwell, W. A. G. III and W. M. Skiff, *J. Am. Chem. Soc.*, 1992, **114**, 10024–10035.
- [72] W. D. Cornell, P. Cieplak, C. I. Bayly, I. R. Gould, K. M. Merz, D. M. Ferguson, D. C. Spellmeyer, T. Fox, J. W. Caldwell and P. A. Kollman, *J. Am. Chem. Soc.*, 1995, **117**, 5179–5197.
- [73] M. Kubo, Y. Oumi, H. Takaba, A. Chatterjee, A. Miyamoto, M. Kawasaki, M. Yoshimoto and H. Koinuma, *Phys. Rev. B*, 2000, **61**, 16187–16192.
- [74] A. V. Banduraă and J. D. Kubicki, *J. Phys. Chem. B*, 2003, **107**, 11072–11081.
- [75] Z. Fan, R. S. Koster, S. Wang, C. Fang, A. O. Yalcin, F. D. Tichelaar, H. W. Zandbergen, M. A. van Huis and T. J. H. Vlugt, *J. Chem. Phys.*, 2014, **141**, 244503.
- [76] N. Y. Mostafa and P. W. Brown, *J. Phys. Chem. Solids*, 2007, **68**, 431–437.
- [77] F. Schiffmann, J. Hutter and J. VandeVondele, *J. Phys.: Condens. Matter*, 2008, **20**, 064206.

-
- [78] M. Catti, A. Pavese, R. Dovesi, C. Roetti and M. Causà, *Phys. Rev. B*, 1991, **44**, 3509–3517.
- [79] E. Francisco, A. M. Pendas and M. A. Blanco, *J. Chem. Phys.*, 2005, **123**, 234305.
- [80] S. Neelamraju, J. C. Schon, K. Doll and M. Jansen, *Phys. Chem. Chem. Phys.*, 2012, **14**, 1223–1234.
- [81] M. Planck, *Annalen der Physik*, 1901, **309**, 553–563.
- [82] E. Schrödinger, *Annalen der Physik*, 1926, **384**, 361–376.
- [83] M. Born, W. Heisenberg and P. Jordan, *Zeitschrift für Physik*, 1926, **35**, 557–615.
- [84] M. S. Longair, *Quantum concepts in physics: an alternative approach to the understanding of quantum mechanics*, Cambridge University Press, 2013.
- [85] M. Born and R. Oppenheimer, *Annalen der Physik*, 1927, **389**, 457–484.
- [86] D. R. Hartree, *Math. Proc. Camb. Phil. Soc.*, 1928, **24**, 89–110.
- [87] J. C. Slater, *Phys. Rev.*, 1929, **34**, 1293–1322.
- [88] V. Fock, *Z. Phys.*, 1930, **61**, 126–148.
- [89] D. R. Hartree and W. Hartree, *P. Roy. Soc. Lond. Ser.-A*, 1935, **150**, 9–33.
- [90] I. N. Levine, *Quantum chemistry*, Prentice Hall, 5th edn., 2000.
- [91] C. C. J. Roothaan, *Rev. Mod. Phys.*, 1951, **23**, 69–89.
- [92] G. G. Hall, *Proc. R. Soc. Lond. A*, 1951, **205**, 541–552.
- [93] E. Schrödinger, *Annalen der Physik*, 1926, **385**, 437–490.
- [94] A. Szabo and N. S. Ostlund, *Modern quantum chemistry*, Dover Publications, 1996.
- [95] L. H. Thomas, *Math. Proc. Camb. Phil. Soc.*, 1927, **23**, 542–548.
- [96] E. Fermi, *Z. Phys.*, 1928, **48**, 73–79.
- [97] P. Hohenberg and W. Kohn, *Phys. Rev.*, 1964, **136**, B864–B871.
- [98] R. G. Parr and W. Yang, *Density-functional theory of atoms and molecules*, Oxford University Press, 1989.
- [99] W. Kohn and L. J. Sham, *Phys. Rev.*, 1965, **140**, A1133–A1138.
- [100] P. A. M. Dirac, *Math. Proc. Camb. Phil. Soc.*, 1930, **26**, 376–385.
- [101] J. C. Slater, *Phys. Rev.*, 1951, **81**, 385–390.

- [102] S. H. Vosko, L. Wilk and M. Nusair, *Can. J. Phys.*, 1980, **58**, 1200–1211.
- [103] D. M. Ceperley and B. J. Alder, *Phys. Rev. Lett.*, 1980, **45**, 566–569.
- [104] J. P. Perdew, K. Burke and M. Ernzerhof, *Phys. Rev. Lett.*, 1996, **77**, 3865–3868.
- [105] P. J. Stephens, F. J. Devlin, C. F. Chabalowski and M. J. Frisch, *J. Phys. Chem.*, 1994, **98**, 11623–11627.
- [106] J. P. Perdew and Y. Wang, *Phys. Rev. B*, 1992, **45**, 13244–13249.
- [107] A. D. Becke, *J. Chem. Phys.*, 1993, **98**, 5648–5652.
- [108] C. Kittel, *Einführung in die Festkörperphysik*, Oldenbourg, 9th edn., 1991.
- [109] F. Bloch, *Z. Phys.*, 1929, **52**, 555–600.
- [110] R. Dovesi, B. Civalleri, C. Roetti, V. R. Saunders and R. Orlando, in *Ab Initio Quantum Simulation in Solid State Chemistry*, ed. L. K.B., L. R. and C. T.R., John Wiley & Sons, Inc., 2005, vol. 21, ch. 1, pp. 1–125.
- [111] S. Saebo and P. Pulay, *Annu. Rev. Phys. Chem.*, 1993, **44**, 213–236.
- [112] P. Pulay and S. Saebo, *Theoretica chimica acta*, 1986, **69**, 357–368.
- [113] M. Schütz, G. Hetzer and H.-J. Werner, *J. Chem. Phys.*, 1999, **111**, 5691–5705.
- [114] G. H. Wannier, *Phys. Rev.*, 1937, **52**, 191–197.
- [115] C. M. Zicovich-Wilson, R. Dovesi and V. R. Saunders, *J. Chem. Phys.*, 2001, **115**, 9708–9719.
- [116] S. Casassa, C. Zicovich-Wilson and C. Pisani, *Theor. Chem. Acc.*, 2006, **116**, 726–733.
- [117] P. Pulay, *Chem. Phys. Lett.*, 1983, **100**, 151–154.
- [118] A. Erba, M. Halo and S. Salustro, *CRYSCOR09 User's Manual*, Università degli Studi di Torino, Torino - Italy, 2009.
- [119] A. J. Stone, *The theory of intermolecular forces*, Clarendon Press, Oxford, 1997.
- [120] F. London, *Trans. Faraday Soc.*, 1937, **33**, 8–26.
- [121] H. B. G. Casimir and D. Polder, *Phys. Rev.*, 1948, **73**, 360–372.
- [122] P. Pyykkö and M. Atsumi, *Chem. Eur. J.*, 2009, **15**, 186–197.
- [123] K. Fukui and T. Yamabe, *Int. J. Quantum Chem.*, 1968, **2**, 359–369.
- [124] G. Starkschall and R. G. Gordon, *J. Chem. Phys.*, 1972, **56**, 2801–2806.

-
- [125] P. P. Ewald, *Annalen der Physik*, 1921, **369**, 253–287.
- [126] D. Frenkel and B. Smit, *Understanding molecular simulation*, Academic Press, 2002.
- [127] A. Y. Toukmaji and J. A. J. Board, *Computer Physics Communications*, 1996, **95**, 73–92.
- [128] D. C. Rapaport, *The art of molecular dynamics simulation*, Cambridge University Press, 1997.
- [129] D. A. McQuarrie and J. D. Simon, *Physical chemistry, a molecular approach*, University Science Books, 1997.
- [130] I. N. Bronstein, K. A. Semendjajew, G. Musiol and H. Mühlig, *Taschenbuch der Mathematik*, Harri Deutsch, 4th edn., 1999.
- [131] J. W. Gibbs, *Collected Works*, Longmans, 1928.
- [132] E. A. Guggenheim, *Trans. Faraday Soc.*, 1940, **35**, 397–412.
- [133] G. Wulff, *Zeitschrift für Kristallographie und Mineralogie*, 1901, **34**, 449–530.
- [134] C. L. Bailey, *Ph.D. thesis*, Imperial College London; STFC Daresbury Laboratory, 2009.
- [135] <http://webbook.nist.gov/chemistry> – accessed 26.09.2014, 11:38.
- [136] J. D. Cox, D. D. Wagman and V. A. Medvedev, *CODATA key values for thermodynamics*, Hemisphere Publ., 1989.
- [137] R. Dovesi, R. Orlando, A. Erba, C. M. Zicovich-Wilson, B. Civalleri, S. Casassa, L. Maschio, M. Ferrabone, M. De La Pierre, P. D’Arco, Y. Noël, M. Causà, M. Rérat and B. Kirtman, *Int. J. Quantum Chem.*, 2014, **114**, 1287–1317.
- [138] R. Dovesi, V. Saunders, C. Roetti, R. Orlando, C. M. Zicovich-Wilson, F. Pascale, B. Civalleri, K. Doll, N. Harrison, I. Bush, P. D’Arco, M. Llunell, M. Causà and Y. Noël, *CRYSTAL14 User’s Manual*, University of Torino, Torino, 2014.
- [139] R. A. Buckingham, *Proc. R. Soc. Lond. A*, 1938, 264–283.
- [140] B. Schmidt, *MolDynSim 1.0: A Matlab program package for molecular simulations*. Available via <http://sourceforge.net/p/trajlab/moldynsim>, 2013.
- [141] P. Eastman, M. S. Friedrichs, J. D. Chodera, R. J. Radmer, C. M. Bruns, J. P. Ku, K. A. Beauchamp, T. J. Lane, L.-P. Wang, D. Shukla, T. Tye, M. Houston, T. Stich, C. Klein, M. R. Shirts and V. S. Pande, *J. Chem. Theory Comput.*, 2013, **9**, 461–469.
- [142] R. S. Mulliken, *J. Chem. Phys.*, 1955, **23**, 1833–1840.
- [143] P. Eastman, *OpenMM Users Guide*, Release 6.3, 2015.

- [144] J. C. Lagarias, J. A. Reeds, M. H. Wright and P. E. Wright, *SIAM Journal on Optimization*, 1998, **9**, 112–147.
- [145] MATLAB, *version 7.12.0 .635 (R2011a)*, The MathWorks Inc., Natick, Massachusetts, 2011.
- [146] P. W. Tasker, *J. Phys. C: Solid State Phys.*, 1979, **12**, 4977–4984.
- [147] C. L. Bailey, S. Mukhopadhyay, A. Wander, B. G. Searle and N. M. Harrison, *J. Phys. Chem. C*, 2009, **113**, 4976–4983.
- [148] F. Jensen, *Introduction to computational chemistry*, Wiley, 1999.
- [149] N. Metropolis and S. Ulam, *J. Am. Stat. Assoc.*, 1949, **44**, 335–341.

Acknowledgement

Writing a doctoral thesis is a solitary task, but many of the people I encountered during this time, or who have accompanied me for much longer, have contributed in the most versatile ways to the successful outcome. I am grateful to all of them.

First and foremost, I am grateful to my supervisor Professor Beate Paulus. She has supported me these last years and has enabled my participation in conferences and workshops. Working with her, I learned a lot – not only about science.

Professor Erhard Kemnitz, who provided us with an intriguing problem to solve, I would like to thank for his vivid interest in my research and for taking the time to be the second referee of my thesis.

I am grateful to Dr. Carsten Müller for his help with practical problems in beginning of my project and the discussions later on. Also, I enjoyed the exchange with Dr. Larisa Schmidt and Dr. Matthias Karg from the Humboldt University.

I would like to thank Dr. Lorenzo Maschio and Giuseppe Sansone from the University of Torino for their help. I enjoyed working with them. I thank all members of the group for Theoretical Chemistry in the University of Torino, for their hospitality during my short stay there.

Among the people who work behind the scenes to ensure the smooth operation of a university, I am grateful to Julija Djordjevic for her help with administrative procedures and her discretion, and to the ZEDAT-team for the technical support. Also, the funding by the Graduate School 1582 and the computational time in the HLRN have been essential for this work.

My colleagues in the joined theoretical chemistry groups at the Freie Universität have offered a great work and break environment. Zeinab Kaawar has stood out with her calm, supportive manner.

Dr. Lukas Hammerschmidt has been an inspiring friend and colleague, has patiently listened to my problems and has brightened me up in difficult moments; together, we have passed through fog and snow. Zita Hüsches, Dr. Axel Schild and Claudia Brieger have offered me valuable distraction and support, in and outside university. My office neighbour Hendrik Ronneburg generously provided me with sources of carbohydrates in the most peculiar times.

For taking my mind off work and making sure I enjoy every now and then the pleasures of life, I would like to thank my dearest friend Irene Exarchou, and Kathrin Grenzdörffler and Ekkerhard Windrich. Most of all, I am grateful to Stefan Hartmann, for all the reasons he best knows.

Finally, the most important: I am grateful to my family, most of all to my parents,

Acknowledgement

who have supported me in all my steps. Since my early childhood, they inculcated in me the enthusiasm for science and knowledge in general.